THEORY OF RESONANCE AND NOVEL NONPERTURBATIVE PHYSICS IN TWISTED BILAYER GRAPHENE

A Dissertation
Presented to
The Academic Faculty

By

Steven C. Carter

In Partial Fulfillment
of the Requirements for the Degree
Doctor of Philosophy in the
School of Physics

Georgia Institute of Technology

May 2017

THEORY OF RESONANCE AND NOVEL NONPERTURBATIVE PHYSICS IN TWISTED BILAYER GRAPHENE

Approved by:

Dr. Markus Kindermann, Advisor
School of Physics
Georgia Institute of Technology

Dr. Phillip N. First
School of Physics
Georgia Institute of Technology

Dr. T. A. Brian Kennedy
School of Physics
Georgia Institute of Technology

Dr. Carlos Sa de Melo
School of Physics
Georgia Institute of Technology

Dr. Martin B. Short
School of Mathematics
Georgia Institute of Technology

Date Approved: April 3, 2017

Opinionum commenta delet dies, naturae judicia confirmat.

Time obliterates the fictions of opinion and confirms the decisions of nature.

Marcus Tullius Cicero

This dissertation is dedicated to my fiancée Stephanie and to my parents, without whose endless love and support I could not have persisted in this endeavor.

ACKNOWLEDGEMENTS

I would like to first thank every member of my Thesis Exam Committee for their critical contribution to this endeavor. I would also like to express my gratitute to Georgia Tech School of Physics Professor Andrew Zangwill for his presence on my Thesis Proposal Committee and his general support and advice as Graduate Coordinator. Additionally, I would like to thank School of Mathematics Professor Kirsten Wickelgren for important guidance regarding a particular topic of this research. I am also grateful to Dr. Michael Trott for providing computational and mathematical insights at Wolfram Research which contributed to another aspect of this project. Former Georgia Tech Postdoctoral Fellow Hridis K. Pal also made contributions to the early success of this project.

Most importantly, I would like to thank my advisor, Professor Markus Kindermann, for his unwavering support and dedication to my success as a student and beyond. Without his expertise and guidance, this project could not have succeeded.

Finally, I would like to thank the School of Physics and the Georgia Institute of Technology for providing financial support, faculty, education, and an intellectual infrastructure in which this research could occur. I also thank the National Science Foundation for funding this research via grant DMR-1055799.

TABLE OF CONTENTS

LIST OF TABLES

LIST OF FIGURES

SUMMARY

Graphene is a fascinating material which has revealed immense commercial and theoretical opportunities. Experiment often produces graphene bilayers with various relative twist angles. While bilayers are well understood in certain configurations, twisted bilayers of graphene have shown strikingly rich phenomenology while also posing significant theoretical challenges. As a consequence, many numerically discovered phenomena have defied analytical understanding to date. A famous such example is the set of so-called magic twist angles, where the velocity of charge carriers vanishes. They have been observed numerically in a nonperturbative regime which has not been accessed analytically. Here we identify an analytically solvable, nonperturbative limit of twisted graphene bilayers in the presence of a perpendicular electric field. We find phenomena very similar to the ones previously studied numerically, but our theory now provides analytical insights and it affords exact predictions.

For example, we demonstrate the emergence of myriad Lifshitz transitions–abrupt discontinuities in physical observables–and find a regime in which a universal set of these transitions appear. This reveals a deep connection between seemingly disparate systems–resonant graphene bilayers with vastly different twist angles.

Most prominently, we demonstrate that graphene bilayers in our resonant limit also have "magic twist angles" where charge carriers have zero velocity and infinite mass at zero Dirac wavevector. We prove that there are infinitely many such angles and we provide exact, analytical expressions for them.

CHAPTER 1
INTRODUCTION

Graphene is a special material which has been studied extensively over the past several decades, unveiling a plethora of exciting behaviors as well as unexplained phenomena. In condensed matter systems such as this, isolated atomic orbitals give way to a composite energy landscape known as energy bands. These bands comprise the dispersion relation, the dependence of allowed energy states on the momentum or wavevector. We focus primarily on physics of low energy electron states in twisted graphene bilayers and on the physics of the Fermi surface, a mathematical construct defined as the boundary between the filled and empty energy states in this dispersion at absolute zero temperature. This surface is of great theoretical interest because many physical observables are dominated by the behavior of electrons on the Fermi surface.

1.1 Graphene

Graphene is atomically-thin single-layer allotrope of carbon which is of great theoretical and practical interest. The honeycomb lattice of carbon atoms is a genuine 2-dimensional crystalline system, with electrons possessing only 2 momentum degrees of freedom. Graphene is a remarkably strong material [1], nearly transparent (only[1] $\pi\alpha \approx 2.3\%$ of white light is absorbed [2]), flexible, has high electronic mobility [3], and has electrical conductivity which can be tuned over a wide range through chemical doping or external electric fields. Moreover, single-layer graphene (SLG) has a particularly intriguing dispersion which supports two strict symmetry-protected linearities in the dispersion called Dirac points, where electrons are governed by a Dirac equation which normally characterizes ultrarelativistic

[1] fine structure constant α

particles. Thus, despite speeds[2] of roughly $c/300$, these electrons provide a probe for these relativistic theories at much lower energy.[4]

However, while being comprised only of many layers of graphene, bulk graphite does not exhibit these astounding properties. This has motivated the invention of the many present-day methods for producing graphene from graphite, such as micromechanical exfoliation, liquid-phase exfoliation, graphite oxidation, chemical vapor deposition, electric arc production, thermal decomposition, and epitaxial growth.[5]

The structure of graphite was determined experimentally via powder diffraction in 1916 [6] and by single crystal diffraction in 1924.[7] The theory of single layer graphene was first explored as a reductionist approach to understanding graphite in 1947 [8] and the massless behavior of electrons obeying a Dirac equation was discovered in 1984.[9] Few-layer graphene (FLG) was first observed by transmission electron microscope (TEM) in 1948 [10] and single layer graphene was directly observed in 2007.[11] Epitaxial graphene was grown on substrates as early as 1979 [12] and in breakthrough experiments which achieved electrical control in 2004.[13] Efforts to mechanically exfoliate graphene began as early as 1990, but it wasn't until 2004 that single layer graphene was cleaved from bulk graphite [14], earning Andre Geim and Kostya Novoselov the 2010 Nobel Prize in physics. The Quantum Hall Effect was observed in 2005, confirming theoretical predictions of the Berry's phase in massless Dirac fermions.[15]

1.2 Theory of Few-Layer Graphene

The theory of single layer graphene is well understood (as of 1947 [8]) in many ways, but current laboratory methods can often produce several layers of graphene, typically in pseudo-random angular orientations. Micromechanical cleavage has been used to produce SLG, FLG, and bilayer graphene (BLG), and FLG has been grown epitaxially on SiC in 2004.[13] This has driven theorists to study few-layer graphene systems, particularly be-

[2] vacuum speed of light c

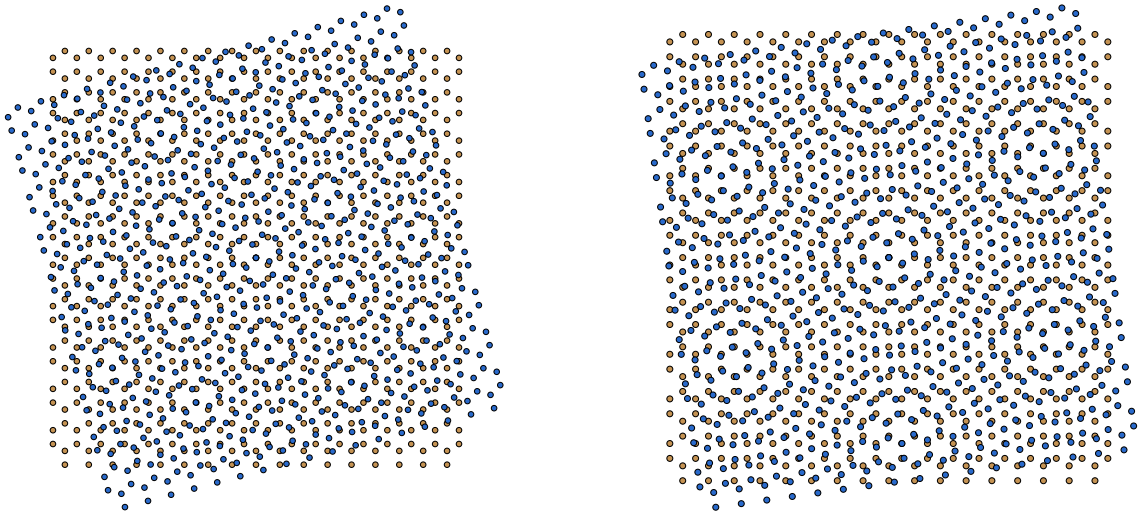

Figure 1.1: Twisted bilayer graphene lattices with interlayer angles $15°$ (left) and $8°$ (right), measured relative to AA. Both figures depict 718 carbon atoms in the lower layer (gold) and 718 carbon atoms in the upper layer (blue) which lie within a square of each graphene lattice with a side length of 30 times the nearest neighbor distance.

ginning with bilayer ones.

However, only the two simplest orientations of BLG are fully understood: rhombohedral (AA configuration, no relative twist) and Bernal-stacked (AB configuration, $60°$ relative twist) bilayers. This is ultimately because such configurations preserve the periodicity of SLG and afford comprehensive quantum mechanics calculations. In these configurations, as well as SLG, the system is a gapless semi-metal, but the linear dispersion of SLG and rhombohedral BLG becomes parabolic in Bernal BLG.[16]

At an arbitrary twist angle in BLG, the periodicity mismatch between the layers produces a Moiré pattern which can be seen in Figure 1.1, which displays bilayers with two different angles on $(0, 60°)$. Observe that each system gains a new, larger-scale periodicity compared to the small scale periodicity of an individual layer. The combined periodic system is a superlattice and has a large repeating unit cell called the supercell. An exact analysis of bilayer graphene with such an arbitrary twist angle is a great task.

1.3 Lifshitz Transitions and Resonance

The Fermi surface is a collection of dimension $(F-1)$ spaces for electrons with F momentum degrees of freedom, and is dependent on physical parameters which can change under certain environmental disruptions, such as chemical doping, interlayer bias voltage, and mechanical stress. One of the features of interest to our research is the Lifshitz transition, an observation that abstract topological transitions in the Fermi surface correspond exactly to abrupt changes in measurable behavior of condensed matter systems.[17] It is difficult to study Lifshitz transitions in metals, but Bernal bilayer graphene supports a single Lifshitz transition which has been measured.[18] Note that SLG and rhombohedral BLG produce no Lifshitz transition.

Typically, arbitrarily twisted BLG is highly decoupled because there is a mismatch in energy between Dirac bands in each layer, resulting in a familiar low-energy spectrum similar to that of SLG.[19] However, at very small angles of rotation, the system becomes nonperturbative and presents unexplained phenomena.[20] The presence of an external electric field through the graphene layers produces a bias voltage and an electric potential energy difference. We show that tuning this bias energy into resonance with the kinetic energy difference between the layers due to the twist angle generates a rich energy landscape near zero wavevector and new nonperturbative phenomena. We will show here that this system, twisted bilayer graphene with resonant bias energy, supports diverse and novel nonperturbative physics and a plethora of Lifshitz transitions.

1.4 Magic Angles

Bistritzer and MacDonald make a mysterious prediction in their 2011 paper using a theory upon which we build much of the work in this dissertation. By numerically modeling the dispersion of non biased twisted bilayer graphene, they find that the electron state velocity goes to zero at a set of "magic angles."[20] These authors provide some conceptual jus-

tification, but no analytic prescription of the value of these angles, likely leading to their choice of name. We show here that a similar zero velocity electron state emerges from graphene bilayers at all twist angles in the presence of particular resonant bias energies. Moreover, this zero velocity state also has a divergent mass, making it profoundly more robust to perturbations. Finally, we provide an exhaustive, analytic prescription of these bias values, but we nonetheless denote them magic energies to align with the prior result.

CHAPTER 2
THE TWISTED BILAYER GRAPHENE HAMILTONIAN

Electrons move within bilayer graphene via intralayer scattering processes and interlayer tunneling. However, the mismatched periodicities of the two layers, which form Moiré patterns as we saw in Figure 1.1, makes the problem of arbitrarily twisted bilayer graphene difficult.

Here we solve a truncated problem using finite-dimensional matrices similar to those in Ref. [20], which describe the electron behavior in small-angle twisted bilayer graphene. We extend this perturbation expansion theory for bilayer graphene to describe arbitrary twist angles as well as an interlayer bias energy due to an external electric field. The true description of such a system is a Hilbert space Hamiltonian operator or infinite dimensional matrix which captures all possible sequences of interlayer tunneling events and intralayer scattering events within the reciprocal superlattice (cf. Section 2.1.4). However, this matrix can be truncated to obtain finite dimensional matrices which describe the low energy physics.

2.1 Geometry

In order to generate Hamiltonian matrices for twisted bilayer graphene, we must first consider the geometry of the system and discover the origin of layer-mismatch momentum transfer vectors which come with interlayer tunneling.

2.1.1 Single Layer Graphene

We begin with a single layer of graphene in real space which consists of carbon atoms lying in a 2-point basis trigonal Bravais lattice. We must choose a coordinate system for the lattice along with a selection of two independent lattice vectors. Our choice of Cartesian

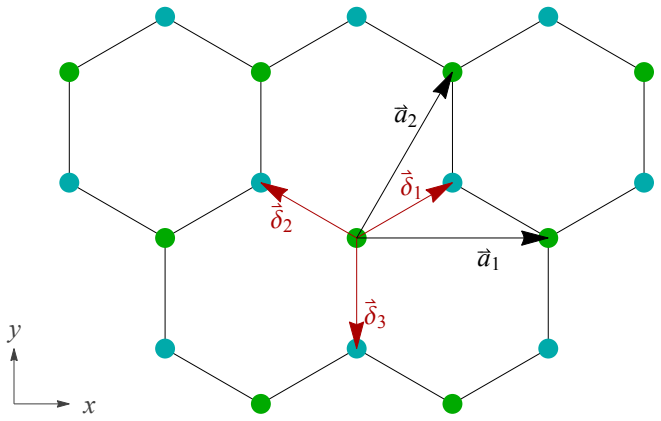

Figure 2.1: Direct lattice for single layer graphene with chosen lattice basis and nearest-neighbor vectors. A and B sublattice carbon atoms are distinguished by disk color.

lattice vectors will be

$$\vec{a}_1 = \sqrt{3}a\,(1,0) \qquad \vec{a}_2 = \sqrt{3}a\left(\tfrac{1}{2}, \tfrac{\sqrt{3}}{2}\right) \tag{2.1}$$

along with sublattice displacement vectors

$$\vec{\delta}_1 = a\left(\tfrac{\sqrt{3}}{2}, \tfrac{1}{2}\right) \qquad \vec{\delta}_2 = a\left(-\tfrac{\sqrt{3}}{2}, \tfrac{1}{2}\right) \qquad \vec{\delta}_3 = a\,(0,-1) \tag{2.2}$$

for a single, non-rotated graphene layer. In the above, $a = a_{CC} \equiv 1.42$Å which is taken as the nearest neighbor distance between adjacent carbon atoms. The value arises as the mean value of the experimental C-C bond lengths in sp^2 hybridized benzene.[4] The direct lattice and lattice vectors appear in Figure 2.1.

The span over integer coefficients of these lattice vectors gives the direct lattice. Thus, an arbitrary vector in the direct lattice is written $\vec{R} = n_1 a_1 + n_2 a_2$ with integral n_j. The reciprocal lattice is defined by all vectors $\vec{G}$ which satisfy the relation $1 = e^{i\vec{G}\cdot\vec{R}}$. We choose

$$\vec{b}_1 = \tfrac{4\pi}{3a}\left(\tfrac{\sqrt{3}}{2}, -\tfrac{1}{2}\right) \qquad \vec{b}_2 = \tfrac{4\pi}{3a}\,(0,1) \tag{2.3}$$

for the reciprocal lattice basis vectors. The reciprocal lattice is given by the span over

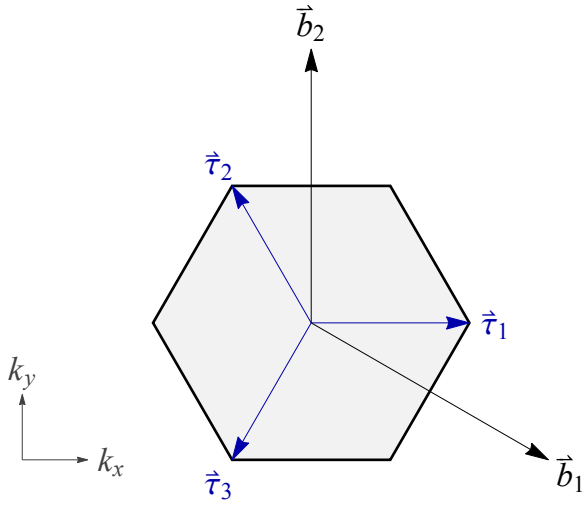

Figure 2.2: Reciprocal lattice and first Brillouin zone for single layer graphene with chosen lattice vectors.

integer coefficients in these basis vectors, $\vec{G} = m_1\vec{b}_1 + m_2\vec{b}_2$ for[1] $m_j \in \mathbb{Z}$.

In reciprocal space, these basis vectors determine equivalence classes between all points which differ by an integral linear combination of the basis vectors. The Wigner-Seitz cell is a set of all inequivalent points which define the first Brillouin zone of the single layer momentum space and is illustrated in Figure 2.2. Three corners of this Brillouin zone at wavevectors

$$\vec{\tau}_1 = \tfrac{4\pi}{3\sqrt{3}a}\,(1,0) \qquad \vec{\tau}_2 = \tfrac{4\pi}{3\sqrt{3}a}\left(-\tfrac{1}{2},\tfrac{\sqrt{3}}{2}\right) \qquad \vec{\tau}_3 = \tfrac{4\pi}{3\sqrt{3}a}\left(-\tfrac{1}{2},-\tfrac{\sqrt{3}}{2}\right) \tag{2.4}$$

are the equivalent crystallographic K point. Another Dirac point is at crystallographic K' with wavevectors $-\vec{\tau}_j$. The equivalence classes due to this lattice periodicity correspond to intralayer scattering processes that connect such equivalent wavevectors.

2.1.2 Bilayer Graphene

Consider now a system of two parallel graphene lattices. The perpendicular interlayer distance is experimentally known and enters the theory indirectly later. However, the relative

[1] integers $\mathbb{Z}$

interlayer rotation angle is left as an experimental variable. For a pair of layers with relative twist $\delta\theta$, we rotate the vectors given in Equations 2.1 and 2.2 by an angle $-\delta\theta/2$ to describe the first layer and rotate the same vectors by $\delta\theta/2$ to define the second layer. The rotated layers and their respective lattice vectors are shown in Figure 2.3.

Using these rotated real space vectors, reciprocal lattice basis vectors and K-point Brillouin corner vectors are computed similarly to Equations 2.3 and 2.4. The rotated first Brillouin zones are shown in Figure 2.4a and simply the basis vectors in Figure 2.4b. Notice that the real space lattice rotations manifest in the same rotations in the reciprocal lattice basis vectors as well.

2.1.3 Dispersion Relation

The dispersion of single layer graphene contains robust symmetry-protected linearities at crystallographic points K and K', corners of its hexagonal Brillouin zone which can be seen in Figure 2.5, taken from [21]. Expansion of the spectrum about these so-called Dirac points reduces the Hamiltonian to a Dirac equation. Most previous efforts to understand twisted bilayer graphene focus on small twist angles so that the Dirac points in each layer are not greatly separated in momentum space. This allows the system with relative twist angle $\delta\theta$ and interlayer bias energy V to be described by a Hamiltonian

$$\begin{pmatrix} H_1 & H_\perp \\ H_\perp^\dagger & H_2 \end{pmatrix} \tag{2.5}$$

where $H_1 = \hbar v \boldsymbol{\sigma} \cdot \vec{k}$ and $H_2 = \hbar v \boldsymbol{\sigma} \cdot \vec{k} + V\sigma_0$ are Dirac matrices for each individual layer. Pauli matrices σ_x and σ_y comprise $\boldsymbol{\sigma} \equiv \begin{pmatrix} \sigma_x & \sigma_y \end{pmatrix}^T$ and σ_0 is the 2-dimensional identity matrix. These are coupled by the interlayer Hamiltonian

$$H_\perp(\vec{r}) = \frac{\gamma}{3} \sum_{j=0}^{2} e^{i\vec{q}_j \cdot \vec{r}} \begin{pmatrix} 1 & e^{-i\frac{2j\pi}{3}} \\ e^{i\frac{2j\pi}{3}} & 1 \end{pmatrix} e^{-i\sigma_z \delta\theta/2} \tag{2.6}$$

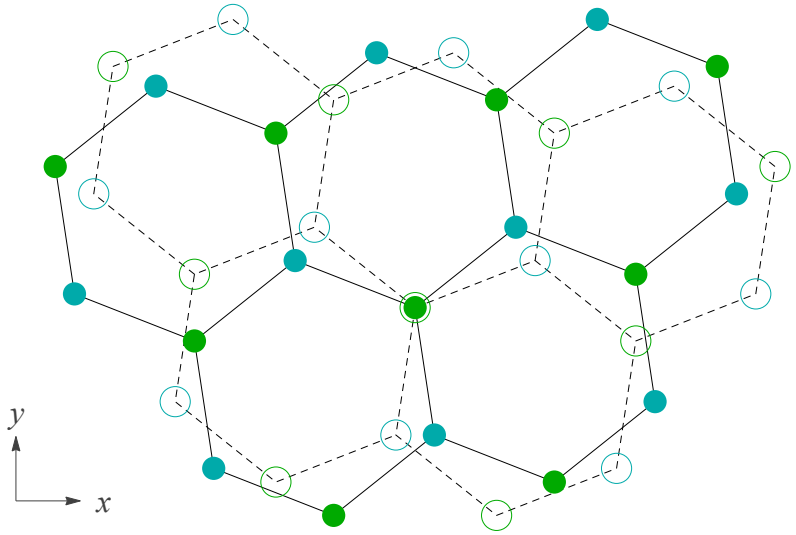

(a) Direct lattices.

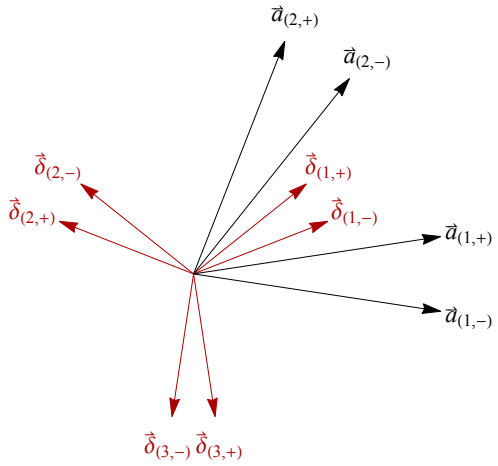

(b) Basis vectors and nearest-neighbor vectors.

Figure 2.3: Description of bilayer graphene twisted with respect to the AA stacking configuration. Lattices and vectors displayed as projections onto a parallel plane of the layers, the top layer (solid,+) is rotated by $\delta\theta/2$ and bottom layer (dashed,-) is rotated by $-\delta\theta/2$ ($\delta\theta = 0.3$ shown).

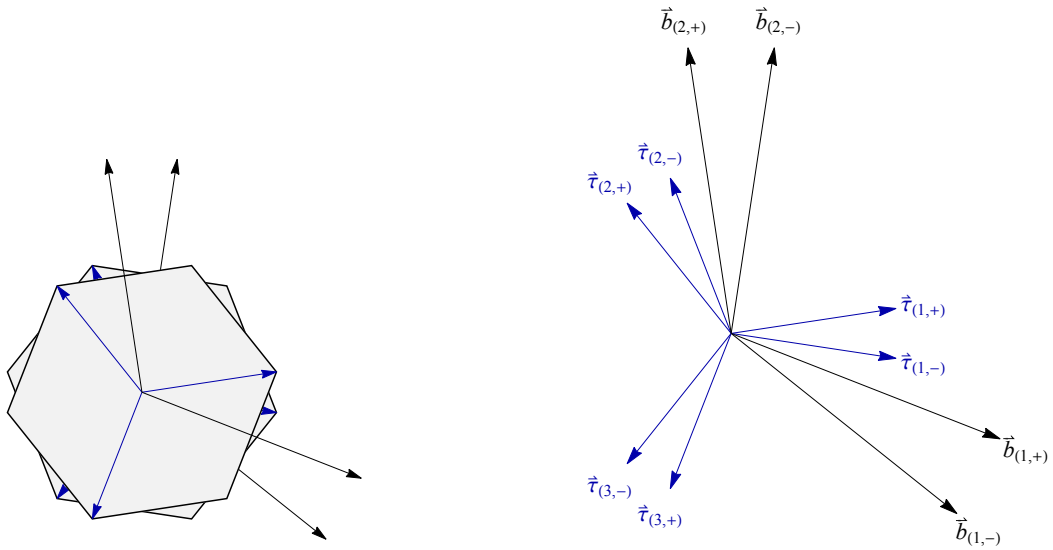

(a) First Brillouin zone and reciprocal vectors.

(b) Reciprocal lattice basis vectors and Brillouin zone corner vectors.

Figure 2.4: Momentum-space description of bilayer graphene twisted with respect to the AA stacking configuration. The Brillouin zone and reciprocal lattice vectors for each layer are projected onto a parallel plane of the layers, the top layer (solid,+) is rotated by $\delta\theta/2$ and bottom layer (dashed,-) is rotated by $-\delta\theta/2$ ($\delta\theta = 0.3$ shown).

in real space, where the $\vec{q}_j = \vec{\tau}_{(j,+)} - \vec{\tau}_{(j,-)}$ are momentum mismatch vectors between the corners of each single layer Brillouin zone defined in the previous section, a result first derived in Ref. [19]. Note that the matrix exponential in Equation 2.6

$$e^{-i\sigma_z\delta\theta/2} = \begin{pmatrix} e^{-i\delta\theta/2} & 0 \\ 0 & e^{i\delta\theta/2} \end{pmatrix} \tag{2.7}$$

can be written explicitly. The Fourier transform of the interlayer coupling is off-diagonal in momentum space and changes $\vec{k}$ by $-\vec{q}_j$. Moreover, the coupling energy γ is a Fourier amplitude of the interlayer potential and can be fitted to experimental data.[22, 23]

This momentum transfer can be explained as follows. Consider an electron near Dirac point $\vec{\tau}_{(j,-)}$ in the first layer with crystal momentum $\vec{p}$. We write this crystal momentum as $\vec{p} = \hbar(\vec{\tau}_{(j,-)} + \vec{k})$ where[2] the small $\vec{k}$ and $\hbar\vec{k}$ are defined as the Dirac wavevector and

[2]reduced Planck constant $\hbar$

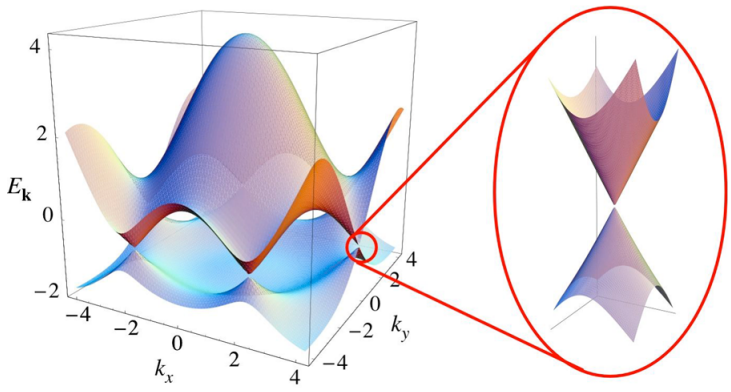

Figure 2.5: Image taken unaltered from Ref. [21], showing the dispersion relation for single layer graphene. The energy is linear with respect to wavevector about the crystallographic K and K' points at the corners of the hexagonal Brillouin zone.[21]

Dirac momentum, respectively. Similarly, we write the crystal momentum for an electron near Dirac point $\vec{\tau}_{(j,+)}$ in the second layer as $\vec{p} = \hbar(\vec{\tau}_{(j,+)} + \vec{k}_{\delta\theta})$. Since interlayer tunneling events conserve crystal momentum, we have $\hbar(\vec{\tau}_{(j,-)} + \vec{k}) = \hbar(\vec{\tau}_{(j,+)} + \vec{k}_{\delta\theta})$, which implies that $\vec{k}_{\delta\theta} = \vec{k} - \vec{q}_j$. Therefore, the Dirac momentum is not conserved in interlayer tunneling events, and this interlayer hopping carries a transfer of $-\hbar\vec{q}_j$ Dirac momentum. We will see in Section 2.2.3, for so-called commensurate twist angles, bilayer graphene is periodic under translation by some finite superlattice basis vectors, like the ones which describe the periodicity of the Moiré pattern seen in Figure 1.1. This larger superlattice periodicity for the composite system generates a new, smaller scale reciprocal superlattice with a smaller Brillouin zone which encompasses all of the unique equivalence classes of wavevectors for the bilayer. The corners of this Brillouin zone are at $\pm\vec{q}_j$. All additional wavevectors in the (k_x, k_y) plane are connected to ones within this small superlattice Brillouin zone by scattering processes along reciprocal superlattice basis vectors $\vec{g}_i$ defined in Equation 2.8 in the next section.

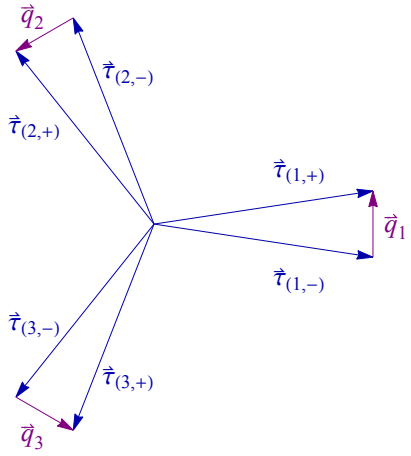

Figure 2.6: Interlayer tunneling vectors $\vec{q}_j$ which arise as momentum difference vectors between the Brillouin zone corner vectors, $\vec{\tau}_{(j,\pm)}$, for each of the rotated layers.

2.1.4 Tunneling Lattice

Recall that the K points in the reciprocal space of each layer differ by small wavevectors $\vec{q}_j = \vec{\tau}_{(j,+)} - \vec{\tau}_{(j,-)}$ which are illustrated in Figure 2.6. Electron interlayer tunneling events carry momentum transfers along these $\vec{q}_j$, as described in the previous section. Consequently, successive interlayer hopping leads to a chain of momenta transfers which can be described by movement within a lattice of points spanned by alternating sequences of these momenta transfers. This lattice is presented in Figure 2.7a.

Notice also that this tunneling lattice is again a trigonal Bravais lattice with 2-point basis. We choose to span this lattice by vectors $\vec{g}_1 = \vec{q}_2 - \vec{q}_1$ and $\vec{g}_2 = \vec{q}_3 - \vec{q}_1$ as indicated in Figure 2.7b. These vectors are given in Equation 2.8 where $\bar{k} \equiv |\vec{\tau}_1| = 4\pi/(3\sqrt{3}a)$. This tunneling lattice will form the foundation of a large amount of the work that follows and we define this set of points, a subset of the two-dimensional wavevector space (k_x, k_y), along with these specific choices of basis vectors, as the set $\mathbb{B}$. An arbitrary vector in $\mathbb{B}$

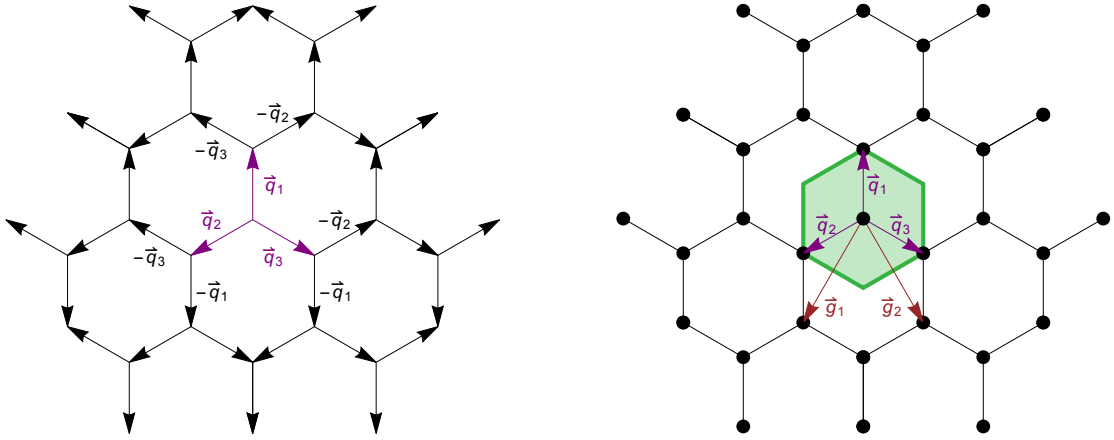

(a) Enumeration of possible tunneling sequences.

(b) Hopping lattice $\mathbb{B}$ with chosen basis vectors along with the superlattice first Brillouin zone.

Figure 2.7: Generation of the hopping lattice $\mathbb{B}$ as alternating sequences of the interlayer tunneling vectors $\vec{q}_j$. The first Brillouin zone of the superlattice is the domain of inequivalent Dirac wavevectors $\vec{k}$ shown in green on the right.

may be written as $\vec{Q} = n\vec{g}_1 + m\vec{g}_2 + t\vec{q}_1$ for $n, m \in \mathbb{Z}$ and $t \in \{0, 1\}$.

$$\vec{q}_1 = 2\bar{k}\sin(\tfrac{\delta\theta}{2})\,(0,1) \qquad \vec{q}_2 = 2\bar{k}\sin(\tfrac{\delta\theta}{2})\left(-\tfrac{\sqrt{3}}{2}, -\tfrac{1}{2}\right) \qquad \vec{q}_3 = 2\bar{k}\sin(\tfrac{\delta\theta}{2})\left(\tfrac{\sqrt{3}}{2}, -\tfrac{1}{2}\right)$$

$$\vec{g}_1 = 2\bar{k}\sin(\tfrac{\delta\theta}{2})\sqrt{3}\left(-\tfrac{1}{2}, -\tfrac{\sqrt{3}}{2}\right) \qquad \vec{g}_2 = 2\bar{k}\sin(\tfrac{\delta\theta}{2})\sqrt{3}\left(\tfrac{1}{2}, -\tfrac{\sqrt{3}}{2}\right) \tag{2.8}$$

Observe also that the K points at $\vec{\tau}_{(j,-)}$ or at $\vec{\tau}_{(j,+)}$, within a layer, are connected via intralayer scattering processes since they differ by a superlattice basis vector $\vec{g}_i$. Consequently, an electron at every site in this lattice can hop to precisely three other sites by tunneling to one of the three K points in the other layer.

2.1.5 Tunneling Length

For reasons that will soon become clear, we wish to assign to each lattice site in our tunneling space two quantities akin to size. The first quantity is the Euclidean metric (or standard distance) in the plane between the given site $\vec{Q}$ and the origin (simply $\sqrt{\vec{Q}\cdot\vec{Q}}$). Henceforth

we will refer to this quantity as the magnitude of $\vec{Q}$ despite the magnitude being formally ill-defined on $\mathbb{B}$. Strictly speaking, this metric is defined here because $\mathbb{B}$ is a subset of the vector space[3] $\langle \mathbb{R} \times \mathbb{R}, (+, \times) \rangle$ in which the l^2 (Euclidean) norm is well-defined.

The second quantity which we assign is essentially the minimum number of tunneling events required to traverse from the origin to a given site $\vec{Q}$. The quantity is equal to the minimum number of edges connecting the site to the origin in Figure 2.7b. We refer to this quantity as the *hopping number* for the site. Formally, we give Definition A.2.1 for a new notion of distance in Appendix A.2 and also there prove that the function is a translation invariant metric in $\mathbb{B}$. Precisely, let the hopping number of site $\vec{Q}$ be given by $\langle \vec{0}, \vec{Q} \rangle_L$ where $\langle \cdot, \cdot \rangle_L$ is the lattice metric defined in Appendix A.2.

Lastly, note that the function defined there gives the desired result for this hopping number only if the basis vectors $\vec{g}_1$, $\vec{g}_2$, and $\vec{q}_1$ are chosen as in Section 2.1.4, which is why the choice was built into the definition of $\mathbb{B}$. The function values are therefore dependent on the basis choice, but the translation invariant metric property is not. Finally, note that the magnitude of $\vec{Q}$ is a non-negative real number and the hopping number is a natural number for all sites in $\mathbb{B}$.

2.1.6 Identification of Tunneling Sites

We can use the preceding ideas to partition the lattice sites in the tunneling lattice into useful sets. We denote sites in $\mathbb{B}$ with hopping number r as members of the r^{th} ring and divide the r^{th} ring into subsets called stars consisting of sites which share a common wavevector magnitude. If $\{l_1, l_2, l_3, \ldots\}$ is the set of magnitudes for all sites in the r^{th} ring such that $l_j < l_{j+1} \quad \forall j$, then we denote the $[r, s]$ star by all sites in the r^{th} ring with Euclidean metric from $\vec{0}$ equal to l_s. Note that the language of "stars" is fairly common in the field, particularly as it emerges in the so-called *first star approximation*, perhaps first defined in Ref. [16] and used in others, including [22]. Our definition of stars is consistent and generalizes it along

[3] real numbers $\mathbb{R}$

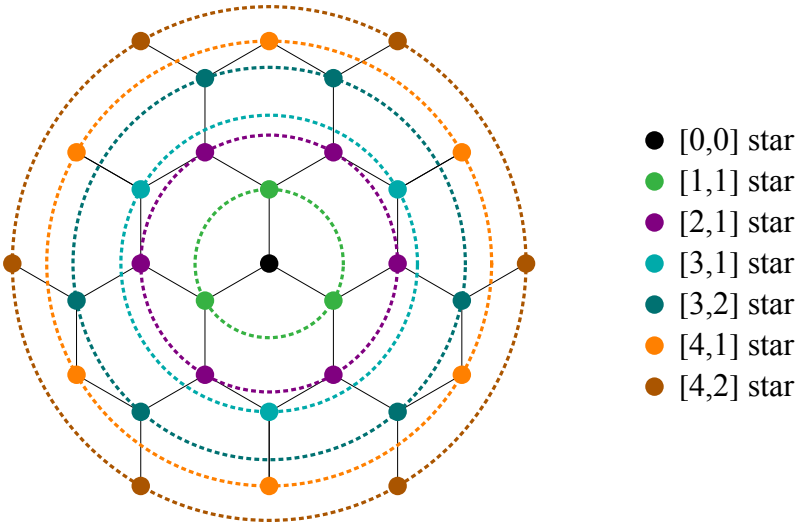

Figure 2.8: A sample of stars in the hopping lattice $\mathbb{B}$, useful subsets indexed first by hopping number and second by ranked magnitude.

with the newly defined "rings" in a systematic way. Figure 2.8 illustrates the first several rings and stars in this convention. Let $m_{r,s}$ be the number of sites in the $[r, s]$ star and $Q_{r,s}$ be the wavevector magnitude of those sites.

2.2 Hamiltonian

We are now prepared to begin constructing the general Hamiltonian matrix. Recall that the true spectrum is given by a Hilbert space operator which could be written, in principle, as an infinite dimensional matrix capturing all possible electron interlayer tunneling sequences.

2.2.1 Hamiltonian Expansion

We follow [20] in order to build finite-dimensional matrices which numerically approximate a portion of the electron energy dispersion. One will note that the explicit matrix elements in the following differ from those in Ref. [20] for several reasons. For one, we chose different coordinates and basis vectors and will expand our Hamiltonian with linear order Dirac matrices near the crystallographic K point rather than the opposing K′ point.

Additionally, we fold the angular dependence into the coupling matrix elements as opposed to the kinetic terms–which amounts to unitary transformation using a convention similar to [24]–allowing us to later generalize our system to much larger twist angles.

We begin building this finite-dimensional Hamiltonian with on-diagonal blocks given by augmented Dirac matrices, similar to the diagonal blocks in Equation 2.5, which have the form

$$h_{\vec{k}}(V) = \begin{pmatrix} V & \hbar v_F \left|\vec{k}\right| e^{-i\varphi(\vec{k})} \\ \hbar v_F \left|\vec{k}\right| e^{i\varphi(\vec{k})} & V \end{pmatrix} \tag{2.9}$$

where $\varphi\left(\vec{k}\right)$ is the angle on $(-\pi, \pi]$ that $\vec{k}$ makes with the k_x axis, v_F is the electron Fermi velocity in graphene, and V is the bias energy, the electric potential energy for an electron induced at this site by a normally oriented, external electric field. We choose the gauge in which the potential is zero in layer 1 and V in the second layer so the zeroth order Hamiltonian is simply $h_{\vec{k}}(0)$. Given a relative twist angle $\delta\theta$ between the layers, tunneling matrices

$$T_p = \gamma \begin{pmatrix} e^{-i\frac{\delta\theta}{2}} & e^{-i\left(\frac{2p\pi}{3} - \frac{\delta\theta}{2}\right)} \\ e^{i\left(\frac{2p\pi}{3} - \frac{\delta\theta}{2}\right)} & e^{i\frac{\delta\theta}{2}} \end{pmatrix} \tag{2.10}$$

arise from the Fourier transform of Equation 2.6 and couple the Dirac blocks along nearest-neighbor edges in $\mathbb{B}$, so that sites whose momenta differ by $\vec{q}_j$ are coupled by T_j.

The first order Hamiltonian

$$H_1 = \begin{pmatrix} h_{\vec{k}}(0) & T_1 & T_2 & T_3 \\ T_1^\dagger & h_{\vec{k}-\vec{q}_1}(V) & 0 & 0 \\ T_2^\dagger & 0 & h_{\vec{k}-\vec{q}_2}(V) & 0 \\ T_3^\dagger & 0 & 0 & h_{\vec{k}-\vec{q}_3}(V) \end{pmatrix} \tag{2.11}$$

takes account of hopping to the $[1, 1]$ star and produces approximations for the 8 smallest energy bands.

A Hamiltonian of order n is constructed by including all sites in $\mathbb{B}$ with hopping number

not in excess of n. In a block form of (2×2) matrices similar to Equation 2.11, diagonal blocks are Dirac matrices for momenta originated at the included sites of $\mathbb{B}$, augmented with the appropriate bias energy. It is readily observed that all sites with hopping number congruent modulo 2 correspond to the same real-space graphene layer and therefore must share a bias energy.

Higher order tunneling events are included in this expansion via successive first order coupling between neighboring sites. Diagonal blocks (i, i) and (j, j) are decoupled if they correspond to non-adjacent sites in $\mathbb{B}$ and consequently blocks (i, j) and (j, i) are the zero matrix. If the momentum origin of block (j, j) is $\vec{q}_p$ greater than that of block (i, i), then block (i, j) is T_p and block (j, i) is $T_p^\dagger$. Conversely, if the momentum origin of block (j, j) is $\vec{q}_p$ less than that of block (i, i), then block (i, j) is $T_p^\dagger$ and block (j, i) is T_p.

The n^{th} order Hamiltonian is denoted H_n and has dimension $3n(n + 1) + 2$. In practice, we generate H_n of arbitrary order in Wolfram *Mathematica* and numerically evaluate the eigenvalues of H_n over a discrete mesh of $\{k_x, k_y\}$ in the Brillouin zone to yield successively larger approximate subsets of the spectrum, $\dim(H_n)$-many bands $\varepsilon_j\left(\vec{k}\right)$. By construction, the $3n(n+1)+2$ bands with the smallest absolute value of energy at $\left|\vec{k}\right| = 0$ appear in H_n and the fidelity of these low energy eigenvalues increases with the order, n.

2.2.2 Numerical Eigenvalue Evaluation

The aforementioned expansion Hamiltonians are functions of several experimentally determined parameters and of the wavevector $\vec{k}$ within the small superlattice Brillouin zone for the two layers. This Brillouin zone consists of a hexagonal region with corners at $\pm\vec{q}_j$ for such tunneling vectors shown in Figure 2.7b. Keep in mind that such wavevectors $\vec{k}$ are but one contribution to crystal momentum $\hbar(\vec{k} + \vec{K})$.

As alluded to previously, the accuracy of these eigenvalues increases with n and also is to be expected to hold more true for smaller wavevectors $\left|\vec{k}\right| \ll |\vec{q}_j|$. However, the Abel-Ruffini theorem proved that there is no algebraic solution for the roots of arbitrary

polynomials of degree 5 or greater.[25, 26] The first order Hamiltonian H_1 has dimension 8 and therefore eigenvalues given by the roots of its degree 8 characteristic polynomial. Furthermore, these matrices lack any of the symmetries that might allow for algebraic solutions, and therefore the eigenvalues of H_n must be computed numerically for all useful $n > 0$.

However, these matrices are also quite sparse which facilitates numerical evaluation considerably. The number of non-zero elements in H_n is bounded from above by $2 + 3n(n+1) + 6\left(\lceil \frac{n}{2} \rceil^2 + 4\left[n\left(n-1\right) + 1 - \delta_0^n\right]\right)$ which grows much less rapidly than the total number of matrix elements, $\left[2 + 3n(n+1)\right]^2$.

2.2.3 General Commensurate Angles

As mentioned previously, a twisted graphene bilayer presents a Moiré pattern with a superlattice consisting of a larger unit cell. Strictly speaking this is not the case for arbitrary deflection angles, but the reality turns out to be only a subtle difference. Let us first consider the possible unique deflection angles for bilayer graphene. Observe that precisely 0° corresponds to AA stacking (Rhombohedral) and precisely 60° corresponds to AB (Bernal) stacking, both of which are described by a simpler theory. Additionally, note the $\mathcal{C}_3$ symmetry of both individual layers (rotations by $2\pi/3$ leave a single layer invariant). Beginning with an AA stacked bilayer, one layer could be rotated by 120° to become again AA stacked. However, any such rotation, Θ, in excess of 60°, could be equivalently recast as a rotation by $120^\circ - \Theta$ with the layers interchanged. Consequently, the complete domain for possible twist angles in our theory is the open interval $(0, 60^\circ)$.

On this angular domain there exist special values called commensurate angles for which the superlattice unit cell has finite size. The commensurate angles are countably infinite and enumerated by the following expression, adapted from [27] since we define angles with respect to AA

$$60^\circ - \left(\frac{180^\circ}{\pi}\right) \arccos\left(\frac{3j^2 - p^2}{3j^2 + p^2}\right) \tag{2.12}$$

with[4] $j \in \mathbb{Z}^+$, $p \in \mathbb{N}$, and $p \leq j$.

This set of commensurate angles is a dense subset of the real interval $[0, \frac{\pi}{3}]$, which means that any actual deflection angle realized by a physical bilayer system falls arbitrarily close to some commensurate one. However, the superlattice unit cell associated with many of these is extremely large. The commensurate angle 0 ($j = 1, p = 0$) corresponds to a superlattice unit cell which is simply the single layer unit cell and thus has Brillouin zone radius $\frac{4\pi}{3\sqrt{3}a}$ as in Equation 2.4. The next smallest superlattice unit cell corresponds to an angle

$$\theta_1 \equiv 38.21\pi/180 \tag{2.13}$$

which emerges from Equation 2.12 at $j = 3, p = 1$ and has Brillouin zone radius $\frac{4\pi\sqrt{7}}{3\sqrt{3}a}$.

Specifically, let us write now the total interlayer rotation angle as $\Theta = \theta + \delta\theta$ where θ will be constrained to exactly commensurate angles and $\delta\theta$ is a small deflection angle. The theory we have developed so far holds only for small angles near 0, i.e. with $\theta = 0$, total interlayer rotation angle $\Theta = \delta\theta$, and $0 < \delta\theta \ll 10^\circ$.

However, it turns out that we may write a similar theory for all rotation angles on $(0, 60^\circ)$ in terms of the deviation from some nearby commensurate angle (namely, that with the largest coupling strength or the smallest supercell). In generally twisted bilayer we rotate the first layer by $-\delta\theta/2$ and the second layer by $\theta + \delta\theta/2$ for a total interlayer angle $\Theta = \theta + \delta\theta$. Similar to Figures 2.4 and 2.6 we obtain new interlayer momentum transfer vectors from the wavevector difference at crystallographic K points. In particular, at $\theta = \theta_1$, these transfer vectors are

$$\begin{aligned}
\vec{q}_1^{(\theta_1)} &= 2\bar{k}\sqrt{7}\sin(\tfrac{\delta\theta}{2})R_{\theta_1}\left(\tfrac{\sqrt{3}}{2}, -\tfrac{1}{2}\right) = \sqrt{7}R_{\theta_1}\vec{q}_3 \\
\vec{q}_2^{(\theta_1)} &= 2\bar{k}\sqrt{7}\sin(\tfrac{\delta\theta}{2})R_{\theta_1}(0, 1) = \sqrt{7}R_{\theta_1}\vec{q}_1 \\
\vec{q}_3^{(\theta_1)} &= 2\bar{k}\sqrt{7}\sin(\tfrac{\delta\theta}{2})R_{\theta_1}\left(-\tfrac{\sqrt{3}}{2}, -\tfrac{1}{2}\right) = \sqrt{7}R_{\theta_1}\vec{q}_2
\end{aligned} \tag{2.14}$$

[4] positive integers $\mathbb{Z}^+$

[5] natural numbers $\mathbb{N} \equiv \mathbb{Z}^+ \cup \{0\}$

where $R_x = \left(\begin{smallmatrix} \cos x & -\sin x \\ \sin x & \cos x \end{smallmatrix}\right)$ and we retain $\bar{k} \equiv 4\pi/\left(3\sqrt{3}a\right)$. Note that the hopping lattice near θ_1 is enumerated by these rotated and scaled hopping vectors similarly to how the original $\vec{q}_j$ enumerated $\mathbb{B}$. Furthermore, the seemingly unusual cyclic relabeling of the new tunneling vectors will later prove to afford a cleaner description.

The general solution for the interlayer coupling matrices in real space has a form similar to that of Equation 2.6 but is given by

$$H_\perp(\vec{r}) = \frac{\gamma^{(\theta)}}{3} \sum_{j=0}^{2} e^{i\vec{q}_j^{(\theta)}\cdot\vec{r}} \begin{pmatrix} 1 & e^{-i\frac{2\pi}{3}(j-p)} \\ e^{i\frac{2\pi}{3}(j-l)} & e^{-i\frac{2\pi}{3}(l-p)} \end{pmatrix} e^{-i\sigma_z\Theta/2} \tag{2.15}$$

where $\Theta = \theta + \delta\theta$ is the total interlayer rotation angle and the l, p indices depend on θ as given in Ref. [24]. In this dissertation, we focus only on the new commensuration with the largest γ, so the new coupling matrices needed to build the perturbative Hamiltonian for a bilayer system with rotation angle $\Theta = \theta_1 + \delta\theta$ are

$$T_p^{(\theta_1)} = \gamma^{(\theta_1)} \begin{pmatrix} e^{-i\frac{\theta_1+\delta\theta}{2}} & e^{-i\left(\frac{2(p-1)\pi}{3} - \frac{\theta_1+\delta\theta}{2}\right)} \\ e^{i\left(\frac{2(p-2)\pi}{3} - \frac{\theta_1+\delta\theta}{2}\right)} & e^{i\left(\frac{\theta_1+\delta\theta}{2} - \frac{2\pi}{3}\right)} \end{pmatrix} \tag{2.16}$$

where $\theta_1 = 38.21\pi/180$ and, notably, the interlayer coupling strength $\gamma^{(\theta_1)} < \gamma$ is diminished. Everything regarding the perturbative scheme follows as described previously, using now the $\vec{q}_j^{(\theta_1)}$ and $T_p^{(\theta_1)}$ to generate general Hamiltonians $H_n^{(\theta_1)}$. Henceforth, symbols will be assumed by default to correspond to the $\theta = 0$ case if a raised index is not explicitly given and all symbols with a raised index (0) are assumed to take on the definition for that symbol without a raised index, e.g. $\vec{q}_j^{(0)} \equiv \vec{q}_j$.

CHAPTER 3
THEORY AND RESONANCE

With a suitable infrastructure to begin studying arbitrarily twisted bilayer graphene, we begin this chapter by introducing our notion of resonance, one of the most important ideas in this work. We also explore in detail the legitimacy of our theory of resonance and other theoretical matters, including the physical parameters and establishing simplification limits. Finally, we will discuss several topological details of the dispersion in twisted bilayer graphene.

3.1 Resonance

The introduction of a normally oriented external electric field through the layers of twisted bilayer graphene provides independent control of a bias energy which differs in each graphene layer. The mismatch in the Dirac spectrum near crystallographic K causes a transfer of momentum shown in Section 2.1.3 which has an associated energy cost. We will see that resonance refers to the case where this energy is equal to the bias energy induced by the electric field and that tunneling is enhanced and new physics emerge.

3.1.1 Bias Resonance

In the coupling free limit, we observe that the Hamiltonian $H_n^{(\theta)}|_{\gamma=0}$ becomes block diagonal. By inspection of Equation 2.9, we see that the coupling-free spectrum consists of eigenvalues $\pm\hbar v_F \left|\vec{k}-\vec{Q}\right|$ and $\pm\hbar v_F \left|\vec{k}-\vec{Q}\right| + V$ for all $\vec{Q}$ in the lattice with even or odd hopping number, respectively. Let us define energies

$$V_{r,s} \equiv (1+\delta V)\,\hbar v_F Q_{r,s} \qquad r \text{ odd} \tag{3.1}$$

where $\delta V \in (-1, 1)$ and $Q_{r,s}$ is the wavevector magnitude of a site in the $[r, s]$ star. We define resonant Hamiltonian $H^{(\theta)}_{n,r,s} \equiv H^{(\theta)}_{n,r,s}|_{V=V_{r,s}}$ and say that the system is in *perfect resonance* with the $[r, s]$ star when $\delta V = 0$ and *imperfect resonance* when $0 < |\delta V| \ll 1$.

Observe that in resonance, the coupling-free spectrum consists of energy bands

$$\varepsilon = \pm\hbar v_F \left|\vec{k} - \vec{Q}\right| \qquad \text{if } \langle \vec{Q}, \vec{0}\rangle_L \text{ even} \tag{3.2}$$

$$\varepsilon = \pm\hbar v_F \left|\vec{k} - \vec{Q}\right| + (1 + \delta V)\,\hbar v_F Q_{r,s} \qquad \text{if } \langle \vec{Q}, \vec{0}\rangle_L \text{ odd} \tag{3.3}$$

where the $\vec{Q}$ are the wavevectors of included sites in $H^{(\theta)}_{n,r,s}|_{\gamma=0}$. Since Dirac wavevector $\vec{k}$ is confined to the Brillouin zone with radius $\left|\vec{q}_1^{(\theta)}\right|$, immediately we observe that Equation 3.2 gives exactly 2 values of zero at $\vec{k} = \vec{0}$ from the site $\vec{Q} = \vec{0}$ at the origin. Additionally, in perfect resonance at $\delta V = \left|\vec{k}\right| = 0$ we see that Equation 3.3 gives exactly one zero-energy for every solution to $\left|\vec{Q}\right| = Q_{r,s}$. It is readily seen that this equation possesses at least $m_{r,s}$ solutions, one for each site in the $[r, s]$ star. For large $Q_{r,s}$ there may be additional solutions, a problem we will explore fully in Chapter 6. Presently, we will define

$$w_{r,s} \geq \begin{cases} 2 & \text{if } r \text{ is even} \\ 2 + m_{r,s} & \text{if } r \text{ is odd} \end{cases} \tag{3.4}$$

precisely as the degeneracy of the zero-energy eigenvalue of $H^{(\theta)}_{n,r,s}|_{\gamma=0}$ at $\vec{k} = \vec{0}$. We will prove in Chapter 6 that the inequality in Equation 3.4 is an equality for all stars with magnitude smaller than $Q_{11,6}$. Specifically, we have

$$w_{r,s} = \begin{cases} 2 & \text{if } r \text{ is even} \\ 2 + m_{r,s} & \text{if } r \in \{1, 3, 5, 7, 9\} \end{cases} \tag{3.5}$$

for the small rings. Furthermore observe that we may resonate only with stars with odd hopping number since only such sites correspond to the second layer in real space and

possess the bias term.

As a particular example, we note that the two-fold degeneracy of $\varepsilon = 0$ at $\left|\vec{k}\right| = 0$ in $H_n^{(\theta)}|_{\gamma=0}$ is increased to a 5-fold degeneracy in $H_{n,1,1}^{(\theta)}|_{\gamma=0}$ ($n \geq 1$) or an 8-fold degeneracy in $H_{n,3,2}^{(\theta)}|_{\gamma=0}$ ($n \geq 3$). Moreover, even imperfect resonance results in a richer energy landscape at small $\left|\vec{k}\right|$ in the true Hamiltonians with coupling reintroduced ($\gamma > 0$). We predict that this resonance will cause novel, nonperturbative physics to emerge in the long wavelength spectrum of $H_{n,r,s}^{(\theta)}$ (r odd) even when $\gamma \neq 0 \neq \delta V$. Such physics will be demonstrated throughout this dissertation, particularly in Chapters 5 and 6.

3.1.2 Expansion Order and Convergence

We saw in the previous section that the concept of stars (defined via the Euclidean metric) is useful since the bias voltage energy may be set into resonance with a star of lattice sites in $\mathbb{B}$. Additionally, it has been mentioned that rings (level sets of the lattice metric to $\vec{0}$) enumerate the sets of sites which contribute to a certain Hamiltonian expansion order. Let us now consider more closely what determines this expansion order.

In the numerical scheme we have described, perturbative energies can be approximated by a Rayleigh-Schrödinger perturbation theory. Consider the perturbations to the central energy bands, which include products of terms of the form

$$\begin{aligned} &\frac{\gamma}{\left(\pm\hbar v_F \left|\vec{k} - \vec{Q}_\eta\right| + I_\eta \left(1 + \delta V\right) \hbar v_F Q_{r,s}\right) - \left(\pm\hbar v_F \left|\vec{k}\right|\right)} \\ &\quad = \zeta \left(\pm \frac{\left|\vec{k} - \vec{Q}_\eta\right|}{\left|\vec{q}_1^{(\theta)}\right|} + I_\eta \left(1 + \delta V\right) \frac{Q_{r,s}}{\left|\vec{q}_1^{(\theta)}\right|} \mp \frac{\left|\vec{k}\right|}{\left|\vec{q}_1^{(\theta)}\right|} \right)^{-1} \end{aligned} \tag{3.6}$$

where the $\vec{Q}_\eta$ are all nonzero wavevector sites included in our description, ζ is defined by

$$\zeta \equiv \frac{\gamma}{\hbar v_F \left|\vec{q}_1^{(\theta)}\right|} \tag{3.7}$$

and I_η is 1 for η from stars with odd first index and 0 otherwise. This dimensionless factor ζ will be known as the *effective coupling strength*.

We draw three conclusions from the form in Equation 3.6. First, the corrections from sites with $\left|\vec{Q}_\eta\right| = Q_{r,s}$, where r and $\langle \vec{Q}_\eta, \vec{0} \rangle_L$ are odd, diverge as $|\delta V| + \left|\vec{k}\right| \cdot \left|\vec{q}_1^{\,(\theta)}\right|^{-1} \to 0$ and therefore the effect of resonance becomes nonperturbative. Second, we observe that ζ provides the scale for all finite corrections. Finally, it can be seen that the following regime ensures both that the resonant star corrections are nonperturbative and that the non-resonant star corrections are perturbatively suppressed.

$$\delta V \frac{Q_{r,s}}{\left|\vec{q}_1^{\,(\theta)}\right|} \ll \zeta \ll 1 \tag{3.8}$$

Generally, we find that for any pair of sites in $\mathbb{B}$, those sites contribute perturbations to the energy of the other which are polynomial in ζ with powers equal to the number of edges along all pathways which connect them in $\mathbb{B}$. Consequently, the contributions of bands from higher stars are monotonically suppressed by small $\zeta < 1$, and finite theory $H^{(\theta)}_{n,r,s}$ produces the low energy spectrum with precision which grows arbitrarily with n.

Equation 3.8 is a sufficient condition for both nonperturbative resonant effects and perturbatively suppressed non-resonant effects, which we will describe as the *resonant regime* for ζ. However, it is not necessary for the convergence of our matrix expansion theory. Indeed, for large $\zeta > 1$, convergence may still be achieved by including sufficiently many sites until

$$\zeta \ll \frac{Q_{t,p}}{\left|\vec{q}_1^{\,(\theta)}\right|} \tag{3.9}$$

is satisfactorily small for some large $Q_{t,p} > Q_{r,s}$. We may then safely ignore contributions from larger stars and obtain a convergent finite Hamiltonian.

In practice, given some ζ, the spectrum of $H^{(\theta)}_{n,r,s}$ is computed numerically for several $n \geq r$ until the eigenvalues *converge* satisfactorily. This truncation of the matrix expansion series produces a valid, finite dimensional theory of the bilayer system in resonance.

3.2 Physical Scales

We will now consider more closely the values and interplay of the physical parameters which define our twisted bilayer graphene system.

3.2.1 Energy Regimes

Our system contains three energy scales, the interlayer coupling γ, the interlayer bias energy V, and $\hbar v_F \left|\vec{q}_1^{(\theta)}\right|$. In the previous section we illustrated the great potential effect of resonating V with particular real multiples of $\hbar v_F \left|\vec{q}_1^{(\theta)}\right|$. We also established how the relationship between γ and $\hbar v_F \left|\vec{q}_1^{(\theta)}\right|$ (expressed via the ratio $\zeta = \gamma / \left(\hbar v_F \left|\vec{q}_1^{(\theta)}\right|\right)$) mediates convergence and acts as a dimensionless, effective coupling strength.

In resonance, we will see that the dominant energy scale depends on the window of inspection. Consider, for example, two (2×2) blocks of $H_{n,1,1}$ $(n > 0)$

$$\begin{pmatrix} (H_{n,1,1})_{3,3} & (H_{n,1,1})_{3,4} \\ (H_{n,1,1})_{4,3} & (H_{n,1,1})_{4,4} \end{pmatrix} = \hbar v_F |\vec{q}_1| \begin{pmatrix} 1+\delta V & \frac{|\vec{k}-\vec{q}_1|}{|\vec{q}_1|} e^{-i\varphi\left(\vec{k}-\vec{q}_1\right)} \\ \frac{|\vec{k}-\vec{q}_1|}{|\vec{q}_1|} e^{i\varphi\left(\vec{k}-\vec{q}_1\right)} & 1+\delta V \end{pmatrix}$$

$$\begin{pmatrix} (H_{n,1,1})_{1,3} & (H_{n,1,1})_{1,4} \\ (H_{n,1,1})_{2,3} & (H_{n,1,1})_{2,4} \end{pmatrix} = \hbar v_F |\vec{q}_1| \begin{pmatrix} \zeta e^{-i\frac{\delta\theta}{2}} & \zeta e^{-i\left(\frac{2\pi}{3}-\frac{\delta\theta}{2}\right)} \\ \zeta e^{i\left(\frac{2\pi}{3}-\frac{\delta\theta}{2}\right)} & \zeta e^{i\frac{\delta\theta}{2}} \end{pmatrix} \qquad n > 0$$

which illustrate both the kinetic and coupling terms in a form factored by $\hbar v_F \left|\vec{q}_1\right|$. In a similar manner, this $\hbar v_F \left|\vec{q}_1^{(\theta)}\right|$ term can be factored from any full Hamiltonian $H_{n,r,s}^{(\theta)}$ and carries the dimensions of energy for the matrix. Note that since $\left|\vec{k}\right| \leq \left|\vec{q}_1^{(\theta)}\right|$ and $|\delta V| \ll 1$ the explicit matrix elements in the Dirac terms are dimensionless complex numbers of roughly order unity. Similarly, the explicit matrix elements in the coupling terms are also dimensionless complex numbers of order ζ.

Therefore, in a global sense, the scale of the energy eigenvalues of $H_{n,r,s}^{(\theta)}$ is determined by $\hbar v_F \left|\vec{q}_1^{(\theta)}\right|$ and the effective interlayer coupling strength is determined by ζ.

Alternatively, we might factor the matrix instead by γ. In this case, we obtain represen-

tative submatrices of $H_{n,1,1}$ ($n > 0$)

$$\begin{pmatrix} (H_{1,1,1})_{3,3} & (H_{1,1,1})_{3,4} \\ (H_{1,1,1})_{4,3} & (H_{1,1,1})_{4,4} \end{pmatrix} = \gamma \begin{pmatrix} \zeta^{-1} + \delta\tilde{V} & \left(\frac{\hbar v_F}{\gamma}\right) |\vec{k} - \vec{q}_1| e^{-i\varphi\left(\vec{k}-\vec{q}_1\right)} \\ \left(\frac{\hbar v_F}{\gamma}\right) |\vec{k} - \vec{q}_1| e^{i\varphi\left(\vec{k}-\vec{q}_1\right)} & \zeta^{-1} + \delta\tilde{V} \end{pmatrix}$$

$$\begin{pmatrix} (H_{1,1,1})_{1,3} & (H_{1,1,1})_{1,4} \\ (H_{1,1,1})_{2,3} & (H_{1,1,1})_{2,4} \end{pmatrix} = \gamma \begin{pmatrix} e^{-i\frac{\delta\theta}{2}} & e^{-i\left(\frac{2\pi}{3} - \frac{\delta\theta}{2}\right)} \\ e^{i\left(\frac{2\pi}{3} - \frac{\delta\theta}{2}\right)} & e^{i\frac{\delta\theta}{2}} \end{pmatrix}$$

where

$$\delta\tilde{V} \equiv \frac{\delta V}{\zeta} \tag{3.10}$$

and for which γ provides the dimensions of energy to the Hamiltonian. The utility of this form will become evident in Section 4.2 where we show the approximate independence of the spectrum on $\left|\vec{q}_1^{\,(\theta)}\right|$ in the limit of small energies and long-wavelength $\left|\vec{k}\right| \ll \left|\vec{q}_1^{\,(\theta)}\right|$ and for suggesting the emergence of a useful dimensionless wavevector measure $\vec{\kappa} = (\hbar v_F/\gamma)\,\vec{k}$.

3.2.2 Control Parameters

Let us now consider the other parameters in our twisted bilayer system. Our description of $H_n^{(\theta)}$ depends on 6 parameters $\{\gamma, \theta, \delta\theta, a, v_F, V\}$ and the physical constant $\hbar$ along with the two wavevector degrees of freedom. In the resonant case we replace V by δV and the other parameters. As mentioned, experiment determines that $\{a, v_F\} = \left\{1.42\text{Å}, 10^6\text{m/s}\right\}$ and $\hbar = 6.582 \cdot 10^{-13}\text{meV} \cdot \text{s}$. We will direct our focus to commensuration angles $\theta \in \{0, \theta_1\} = \{0, 38.21\pi/180\}$ and moderately small deviation angles $0 < \delta\theta \ll 10^\circ$. The bias energy V is theoretically unbound, but experimentally confined below roughly 250meV. The bias deviation $\delta V \in (-1, 1)$ is a small free parameter.

However, γ depends on the exact system we inspect, for example, the value depends on the commensuration angle θ.[24] Moreover, an insulating layer can be placed between the graphene layers which weakens the coupling of electrons in the graphene layers. One

Table 3.1: Interlayer coupling strength for several nearly-commensurate graphene bilayers with interlayer twist angle $\Theta = \theta + \delta\theta$. The intermediary layer included in one case is hexagonal boron nitride.

Twisted Bilayer Graphene Interlayer Coupling		
Commensuration Angle, θ	Intermediary Layer	Coupling Strength, γ (meV)
0	none	330meV
0	h-BN	20meV
$\theta_1 = 38.21\pi/180$	none	7meV

candidate material for this is hexagonal boron nitride (h-BN), a single layer allotrope of BN which is also characterized by a trigonal Bravais lattice with 2-point basis. The B and N atoms each occupy one sublattice and has been shown to weaken the interlayer coupling strength when placed between graphene layers.[28] Table 3.1 outlines three values of the interlayer coupling which we will examine in detail, primarily in Chapter 5. Therefore, in practice, the parameters which constitute the majority of our control over the system are θ, $\delta\theta$, γ, the star with which we resonate, and δV. Finally, observe that, when treating $\{a, v_F\}$ as constants and $\theta \in \{0, \theta_1\}$, the pair of independent parameters $\{\delta\theta, \gamma\}$ may be exchanged for new independent parameters

$$\hbar v_F \left|\vec{q}_1^{(\theta)}\right| = \begin{cases} \hbar v_F \left[8\pi/\left(3\sqrt{3}a\right)\right] \sin\left(\delta\theta/2\right) & \text{if } \theta = 0 \\ \hbar v_F \left[8\sqrt{7}\pi/\left(3\sqrt{3}a\right)\right] \sin\left(\delta\theta/2\right) & \text{if } \theta = \theta_1 \end{cases}$$
$$\zeta = \gamma/\left(\hbar v_F \left|\vec{q}_1^{(\theta)}\right|\right) \tag{3.11}$$

which are the kinetic energy seen in the last section and the effective coupling strength.

3.2.3 Resonant Region

The complete spectrum of our twisted bilayer system lies in a hexagonal prism with infinite extent along the energy axis and finite hexagonal cross section in 2D wavevector space which is the superlattice Brillouin zone, with corners at the $\pm\vec{q}_j^{(\theta)}$(cf. Section 2.1.3).

However, our primary interest in this spectrum lies within a finite energy window near 0 and sometimes within a smaller domain in wavevector space than the full BZ. Particularly when our goal is to isolate and study the effect of resonance it will prove useful to define a special region of this complete wavevector-energy space.

In Section 3.1.1 we saw that resonance increases the degeneracy of the zero energy state in the limit of no coupling, and in the following section we showed that these bands produce nonperturbative physics. We will hence refer to these bands as *resonant bands*, distinguished from the remaining bands as *non-resonant* ones. Now we construct a particular region to focus our inspection on the resonant bands.

This region in wavevector-energy space depends on the star cast into resonance. Let $\mathbb{L}_{r,s}$ be the rectangular prism for which $\max\{|k_x|, |k_y|\} \leq f_{r,s}\left|\vec{q}_1^{(\theta)}\right|$ and $\left|\varepsilon(\vec{k})\right| \leq f_{r,s}\hbar v_F\left|\vec{q}_1^{(\theta)}\right|$. This closed region is constructed precisely such that $\mathbb{L}_{r,s}$ is devoid of all non-resonant bands of $H^{(\theta)}_{n,r,s}|_{\gamma=0}$. In particular, we explicitly specify this region by

$$\begin{aligned} f_{1,1} &= \frac{1-\delta V}{2} \\ \delta V &\in \left(-\frac{1}{2}, \frac{1}{4}\right) \end{aligned} \tag{3.12}$$

and

$$\begin{aligned} f_{3,2} &= \frac{1}{4}\left(\sqrt{13} - 2 - \left|\sqrt{13} + 2 - 2\sqrt{7}\,(1+\delta V)\right|\right) \\ \delta V &\in \frac{1}{4\sqrt{7}}\left(2-\sqrt{7}, \sqrt{7}-2\right) \end{aligned} \tag{3.13}$$

for systems in resonance with the $[1,1]$ and $[3,2]$ stars. We note that these numbers lie approximately within

$$f_{1,1} \in (0.375, 0.750) \tag{3.14}$$

$$f_{3,2} \in (0.242, 0.401) \tag{3.15}$$

depending on the value of δV over their respective validity intervals. The factors become

$$f_{1,1}|_{\delta V=0} = 1/2 \tag{3.16}$$

$$f_{3,2}|_{\delta V=0} = \left(\sqrt{7}-2\right)/2 \approx 0.323 \tag{3.17}$$

in perfect resonance.

By construction, we expect to see roughly no contribution to the dispersion from non-resonant bands within this prism, provided ζ is sufficiently small. Therefore, the energy scale cannot be set by $\hbar v_F \left|\vec{q}_1^{(\theta)}\right|$ and must instead be determined by γ. Observe that

$$t\gamma \leq f_{r,s}\hbar v_F \left|\vec{q}_1^{(\theta)}\right| \iff \zeta \leq \frac{f_{r,s}}{t} \quad \forall t > 0 \tag{3.18}$$

illustrates that fitting an energy window proportional to γ within the resonant region imposes an upper bound on the effective coupling ζ. We will make use of this observation in Section 5.2.2 and make further general use of these regions in Chapter 5.

3.3 Topology

We conclude this chapter with an introduction of several topological matters. The primary necessity will be to facilitate the discussion of *Lifshitz Transitions*, stark changes in the behavior of physical observables which have been precisely mapped onto abstract topological discontinuities as we will here explore.

3.3.1 Lifshitz Transitions

Given a suitably convergent Hamiltonian, we can observe a valid representation of the dispersion relation of the system by numerical evaluation of the eigenvalues. A feature of particular interest in condensed matter systems is the Fermi surface, the boundary between filled and empty states in reciprocal space. The Fermi surface is a level set of energy as

a function of wavevector, the contour of the dispersion relation at the Fermi energy. By adjusting parameters such as the chemical potential, the Fermi energy can be tuned. It has been shown that if a change in the Fermi energy causes the "topology" of the Fermi surface to change, then the system experiences an abrupt observable phenomenon called a Lifshitz Transition.[17] This theory has since been studied in great depth, such as in Ref. [29]. As discussed previously, these abstract topological phase transitions are important because they predict drastic changes in measurable macroscopic material properties.

More precisely, let Fermi surfaces at energies ε_F and ε'_F be *topologically equivalent* if and only if there exists a homeomorphism which maps the Fermi surface at ε_F to the Fermi surface at ε'_F. Next, we partition the energy codomain of the dispersion into open intervals in which the Fermi surface is topologically equivalent for any pair of energies selected from the interval. Finally, a Lifshitz transition occurs exactly at the boundaries of all such intervals. The Lifshitz transition is an example of what is known as a topological phase transition.

3.3.2 Fermi Surface and Brillouin Zone Topology

Since our system has two wavevector degrees of freedom, a level set of energy in the dispersion will consist of a disjoint union of 0 and 1-dimensional spaces. Explicitly, the Fermi surface for this system may contain 0-dimensional points, sets homeomorphic to the circle ($\mathcal{S}^1$), and wedge sums of $\mathcal{S}^1$. In other words, we expect the Fermi surface to be a union of 0 and 1-dimensional manifolds without boundary, though self-intersection is allowed.

The Fermi surface is embedded in a space of dimension 2, the space of suitable wavevectors (k_x, k_y). However, we have not yet considered the topology of this domain, which is the first Brillouin zone. This space is homeomorphic not to the real plane ($\mathbb{R} \times \mathbb{R}$) but rather to the 2-torus $\mathbb{T}^2$. To show this, first recall that all points which differ by an integral linear combination of the reciprocal lattice vectors in Equations 2.8 are equivalent.

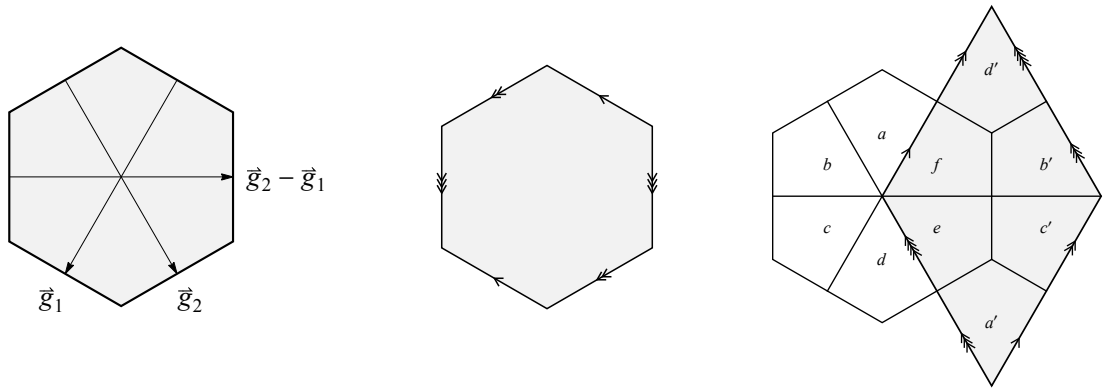

(a) Reciprocal lattice vectors. (b) Gluing diagram. (c) Transformed gluing diagram.

Figure 3.1: Interlayer Brillouin zone. A rough graphical proof of the $\mathbb{T}^2$ topology of this space. Reciprocal lattice vectors lead to edge identification and this gluing diagram is transformed by those vectors to produce a diagram for the 2-torus.

We see in Figure 3.1a that the six edges of the Brillouin zone are connected by vectors $\vec{g}_1$, $\vec{g}_2$, and $\vec{g}_2 - \vec{g}_1$, which leads to identification of those edges in the topological gluing diagram in Figure 3.1b. In Figure 3.1c the diagram is partitioned into six pieces, four of which are translated by reciprocal lattice vectors $\vec{g}_1$, $\vec{g}_2$, and $\vec{g}_2 - \vec{g}_1$ to obtain an equivalent gluing diagram with only 4 apparent edges. Preservation of the proper edge identifications from Figure 3.1b results in the edge diagram within Figure 3.1c which is equivalent to the canonical gluing diagram for the 2-torus.

Finally, recall that an open set in $\mathbb{T}^2$ is locally homeomorphic to that set in the real plane. As a corollary, any patch of the first Brillouin zone which does not contain the apparent "edges" of the hexagon in Figure 3.1a is locally homeomorphic to the same set in the real plane. Also recall that our perturbation scheme converges more readily for wavevectors $\left|\vec{k}\right| \ll |\vec{q}_1|$ which lie towards the center of the Brillouin zone. Therefore, the fact that the embedding space for the Fermi surface is the 2-torus turns out to be, perhaps fortuitously, of reduced consequence in some contexts of our research. Informally, provided that two Fermi surfaces lie entirely within the first Brillouin zone, we can consider the surfaces to be embedded in the real plane when determining topological equivalence. Should one or both of the Fermi surfaces extend beyond the first Brillouin zone, then the topological "nature"

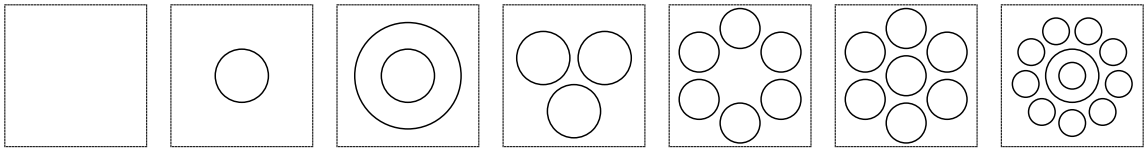

(a) $\mathcal{V}$ (b) $\mathcal{O}$ (c) $\mathcal{T}$ (d) $\mathcal{R}$ (e) $\mathcal{X}$ (f) $\mathcal{N}$ (g) $\mathcal{L}$

Figure 3.2: Canonical topological equivalence classes of several possible Fermi surfaces.

of those surfaces is explicitly dependendent on the embedding space $\mathbb{T}^2$. Strictly, this "nature" is described by the free homotopy class for the 1-manifold (of which there exist $(\mathbb{Z} \times \mathbb{Z})$ countably infinite classes) and determining the topological equivalence between such Fermi surfaces is substantially more difficult.

3.3.3 Topological Words

In the last section we mentioned the range of topological classes which are permitted in the Fermi surface. Figure 3.2 illustrates several examples of allowed states. In order to provide succinct descriptions of Lifshitz transitions, we will introduce the concept of a *topological word* to characterize the evolution of the Fermi surface. We denote the equivalence class of states homeomorphic to the canonical states shown in Figure 3.2 by the calligraphic letters in those figure captions. For example, we define the equivalence class of states homeomorphic to the circle as the $\mathcal{O}$ state shown in Figure 3.2b. Similarly, let the equivalence class of all states which are topologically equivalent to canonical state ξ in Figure 3.2 be denoted by $\xi \in \{\mathcal{V}, \mathcal{O}, \mathcal{T}, \mathcal{R}, \mathcal{X}, \mathcal{N}, \mathcal{L}\}$. These labels were chosen somewhat arbitrarily, yet mnemonically (**v**oided, **o**ne, **t**wo, th**r**ee, si**x**, seve**n**, e**l**even).

The topological word is defined on a region of wavevector-energy space, $\mathbb{D}$, and is given by the concatenation of these topological letter designations corresponding to the sequence of topologically inequivalent level sets of $\varepsilon\left(\vec{k}\right)$ in $\mathbb{D}$, ordered by increasing energy. Therefore, by construction, a t-letter topological word describes a system with $(t-1)$ Lifshitz transitions on $\mathbb{D}$. We will employ these topological words in Chapter 5 to characterize Lifshitz transitions.

CHAPTER 4

EFFECTIVE RESONANT THEORY

In Section 3.1.1 we observed that the degeneracy of the zero-energy state can be increased in the coupling free limit through resonance. Namely, this degeneracy is increased to at least 2 plus the number of sites in $\mathbb{B}$ included in the resonant star, a quantity $w_{r,s}$ there defined (cf. Equation 3.4). However, one should notice that our perturbative expansion theory does not fully exploit this congruence. The matrix $H^{(\theta)}_{n,r,s}$ takes the central Dirac bands as the primitive physics and includes corrections from every site in the first n rings. However, in Section 3.1.2 we saw that, at perfect resonance, the contributions from the resonant star are strictly nonperturbative. We now seek a theory which appropriately places these contributions on equal footing in order to extract the clearest description of this novel physics. We will now identify these "low-energy" eigenmodes in the real system with nonzero coupling. The main result of this chapter appears as well in Ref. [30].

4.1 Schrieffer-Wolff Transformation

To isolate the low energy bands, we must first transform our Hamiltonian from a layer basis into an energy basis. To do this, the eigenvectors of the coupling-free Hamiltonian $H^{(\theta)}_{n,r,s}|_{\gamma=0}$ are arranged according to non-decreasing absolute magnitude of their eigenvalues to form unitary transformation

$$U^{(\theta)}_{n,r,s} = \begin{pmatrix} \vec{\psi}_1 & \vec{\psi}_2 & \cdots & \vec{\psi}_{3n(n+1)+2} \end{pmatrix} \tag{4.1}$$

where $\left(H^{(\theta)}_{n,r,s}|_{\gamma=0}\right)\vec{\psi}_j = \varepsilon_j\vec{\psi}_j$ and $|\varepsilon_j| \leq |\varepsilon_{j+1}|$. A new Hamiltonian matrix

$$\mathcal{H}^{(\theta)}_{n,r,s} = (U^{(\theta)}_{n,r,s})^\dagger H^{(\theta)}_{n,r,s} U^{(\theta)}_{n,r,s} \tag{4.2}$$

reproduces the spectrum of $H^{(\theta)}_{n,r,s}$ since $U^{(\theta)}_{n,r,s}$ is unitary. In general, with coupling reintroduced ($\gamma > 0$), we still expect to have $w_{r,s}$ (typically $2 + m_{r,s}$, cf. Section 3.1.1) many "low-energy" bands at small wavevectors for a system in resonance with the $[r, s]$ star, the two bands from the central Dirac cone and 1 band from each site which lies on a circle of radius $Q_{r,s}$ (cf. Equation 3.1).

By construction of our unitary transformation, our energy basis Hamiltonian separates the low and high energy subspaces of the spectrum. The Schrieffer-Wolff transformation is a Hilbert space operator transformation which produces an approximate effective Hamiltonian by decoupling the low and high energy subspaces and was first used for a specific problem by the namesake authors.[31] The transformation was further developed and placed on a solid mathematical foundation in Ref. [32].

We separate the Hilbert space into high and low energy subspaces by writing

$$\begin{pmatrix} H_L & H^\dagger_{\text{int}} \\ H_{\text{int}} & H_H \end{pmatrix} \equiv \left(U^{(\theta)}_{n,r,s}\right)^\dagger H^{(\theta)}_{n,r,s} U^{(\theta)}_{n,r,s} \tag{4.3}$$

with matrix H_L chosen to be square and dimension $w_{r,s}$. More explicitly, these block

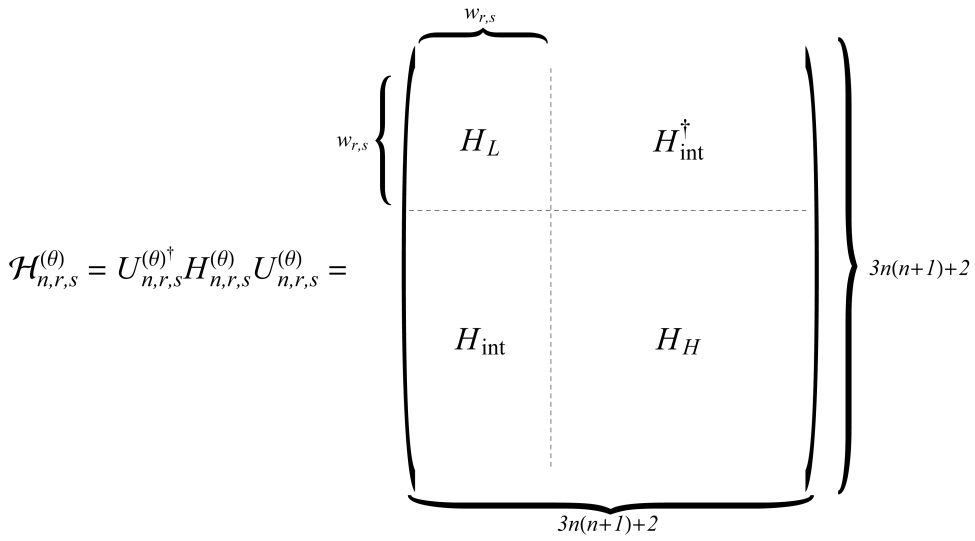

Figure 4.1: Block matrix diagram for energy basis Hamiltonian $\mathcal{H}_{n,r,s}$. Square block submatrices H_L and H_H capture the low and high energy subspaces of the spectrum of $\mathcal{H}^{(\theta)}_{n,r,s}$ and H_{Int} couples these subspaces.

matrices of $\mathcal{H}^{(\theta)}_{n,r,s}$ are given by

$$
\begin{aligned}
H_L &= \begin{pmatrix} \left(\mathcal{H}^{(\theta)}_{n,r,s}\right)_{1,1} & \dots & \left(\mathcal{H}^{(\theta)}_{n,r,s}\right)_{1,w_{r,s}} \\ \vdots & \ddots & \vdots \\ \left(\mathcal{H}^{(\theta)}_{n,r,s}\right)_{w_{r,s},1} & \dots & \left(\mathcal{H}^{(\theta)}_{n,r,s}\right)_{w_{r,s},w_{r,s}} \end{pmatrix} \\
H_H &= \begin{pmatrix} \left(\mathcal{H}^{(\theta)}_{n,r,s}\right)_{w_{r,s}+1,w_{r,s}+1} & \dots & \left(\mathcal{H}^{(\theta)}_{n,r,s}\right)_{w_{r,s}+1,3n(n+1)+2} \\ \vdots & \ddots & \vdots \\ \left(\mathcal{H}^{(\theta)}_{n,r,s}\right)_{3n(n+1)+2,w_{r,s}+1} & \dots & \left(\mathcal{H}^{(\theta)}_{n,r,s}\right)_{3n(n+1)+2,3n(n+1)+2} \end{pmatrix} \\
H_{\text{int}} &= \begin{pmatrix} \left(\mathcal{H}^{(\theta)}_{n,r,s}\right)_{w_{r,s}+1,1} & \dots & \left(\mathcal{H}^{(\theta)}_{n,r,s}\right)_{w_{r,s}+1,w_{r,s}} \\ \vdots & \ddots & \vdots \\ \left(\mathcal{H}^{(\theta)}_{n,r,s}\right)_{3n(n+1)+2,1} & \dots & \left(\mathcal{H}^{(\theta)}_{n,r,s}\right)_{3n(n+1)+2,w_{r,s}} \end{pmatrix}
\end{aligned}
\tag{4.4}
$$

and shown schematically in Figure 4.1.

We then produce a new matrix by Schrieffer-Wolff transformation

$$\begin{aligned} C^{(\theta)}_{n,r,s} &= H_L - H^{\dagger}_{\text{int}} H_H^{-1} H_{\text{int}} \\ &= H_L - H^{\dagger}_{\text{int}} \left(A^{-1} \sum_{\nu=0}^{\infty} (-1)^{\nu} \left(B A^{-1} \right)^{\nu} \right) H_{\text{int}} \end{aligned} \tag{4.5}$$

where $A \equiv H_H|_{\gamma=0}$ and $B \equiv H_H - H_H|_{\gamma=0}$ and $C^{(\theta)}_{n,r,s}$ has the dimension of H_L. Specifically, this matrix $C^{(\theta)}_{n,r,s}$ obtained by the Schrieffer-Wolff transformation of $\mathcal{H}^{(\theta)}_{n,r,s}$ is a Hermitian matrix of dimension $w_{r,s}$ and produces an approximation of the low-energy spectrum which is exact at zero energy. For orders $n \geq 2$, the inverse H_H^{-1} is incomputable and must be approximated by a finite truncation of the Neumann expansion.

4.2 Effective Theory of [1,1] Resonance

We consider now the simplest manifestation of this low energy theory. Our present goal is to gain insight into the nature of the low energy spectrum at long wavelength $\left|\vec{k}\right| \ll \left|\vec{q}_1^{(\theta)}\right|$. Examination of the numerical spectra has revealed that, in the resonant regime, the spectrum of $H^{(\theta)}_n$ depends very little on the explicit $\delta\theta$ terms appearing in the coupling blocks and the dominating effect of this parameter is rather through the $\sin(\delta\theta/2)$ dependence in the $\left|\vec{q}_j^{(\theta)}\right|$ (this can be seen in the next chapter in Figures 5.5 and 5.7, for example). At present, we assume this fact and expand $H^{(\theta)}_{1,1,1}$ to linear order in $\left|\vec{k}\right| \left|\vec{q}_1^{(\theta)}\right|^{-1}$ and replace $T_p^{(\theta)} \rightarrow T_p^{(\theta)}|_{\delta\theta=0}$ to obtain an approximate dimension-8 Hamiltonian $\tilde{H}^{(\theta)}_{1,1,1}$. From this Hamiltonian, we produce a dimension-5 matrix $\tilde{C}^{(\theta)}_{1,1,1}$ by Schrieffer-Wolff transformation, analogous to Equation 4.5.

Finally, we create effective Hamiltonians

$$H^{(0)}_{\text{eff}} = \Upsilon_1^{\dagger} \tilde{C}^{(0)}_{1,1,1} \Upsilon_1 \tag{4.6}$$

and

$$H_{\text{eff}}^{(\theta_1)} = (\Upsilon_3 \Upsilon_2)^\dagger \, \tilde{C}_{1,1,1}^{(\theta_1)} \, (\Upsilon_3 \Upsilon_2) \tag{4.7}$$

where

$$\Upsilon_1 \equiv \begin{pmatrix} 1 & 0 & 0 & 0 & 0 \\ 0 & 1 & 0 & 0 & 0 \\ 0 & 0 & e^{-i\frac{\pi}{12}} & 0 & 0 \\ 0 & 0 & 0 & e^{-i\frac{\pi}{12}} & 0 \\ 0 & 0 & 0 & 0 & e^{-i\frac{\pi}{12}} \end{pmatrix} \tag{4.8}$$

$$\Upsilon_2 \equiv \begin{pmatrix} 1 & 0 & 0 & 0 & 0 \\ 0 & 1 & 0 & 0 & 0 \\ 0 & 0 & 0 & 1 & 0 \\ 0 & 0 & 0 & 0 & 1 \\ 0 & 0 & 1 & 0 & 0 \end{pmatrix} \tag{4.9}$$

$$\Upsilon_3 \equiv \begin{pmatrix} 1 & 0 & 0 & 0 & 0 \\ 0 & 1 & 0 & 0 & 0 \\ 0 & 0 & e^{i\left(\frac{11\pi}{12}+\frac{\theta_1}{2}\right)} & 0 & 0 \\ 0 & 0 & 0 & e^{i\left(\frac{11\pi}{12}+\frac{\theta_1}{2}\right)} & 0 \\ 0 & 0 & 0 & 0 & e^{i\left(\frac{11\pi}{12}+\frac{\theta_1}{2}\right)} \end{pmatrix} \tag{4.10}$$

are unitary gauge transformations. By careful construction, these effective Hamiltonians can be written simultaneously as

$$H_{\text{eff}}^{(\theta)} = \gamma \begin{pmatrix} -\frac{3\zeta\Omega_-^2}{2+\delta V} & (\kappa_x - i\kappa_y) & e^{-i\frac{2\pi}{3}}\Omega_+ & e^{i\frac{2\pi}{3}}\Omega_+ & \Omega_+ \\ (\kappa_x + i\kappa_y) & -\frac{3\zeta\Omega_-^2}{2+\delta V} & \Omega_+ & \Omega_+ & \Omega_+ \\ e^{i\frac{2\pi}{3}}\Omega_+ & \Omega_+ & \vec{\kappa}\cdot\hat{q}_1^{(\theta)} + \delta\tilde{V} & 0 & 0 \\ e^{-i\frac{2\pi}{3}}\Omega_+ & \Omega_+ & 0 & \vec{\kappa}\cdot\hat{q}_2^{(\theta)} + \delta\tilde{V} & 0 \\ \Omega_+ & \Omega_+ & 0 & 0 & \vec{\kappa}\cdot\hat{q}_3^{(\theta)} + \delta\tilde{V} \end{pmatrix} \tag{4.11}$$

where

$$\Omega_{\pm} \equiv \begin{cases} \left(\sqrt{3} \pm 1\right)/2 & \text{if} \quad \theta = 0 \\ \cos(\theta_1) \mp \sin(\theta_1) & \text{if} \quad \theta = \theta_1 \end{cases}$$
$$\vec{\kappa} \equiv \left(\frac{\hbar v_F}{\gamma}\right) \vec{k}$$

and $\delta\tilde{V} = \delta V/\zeta$ as in Equation 3.10.

In this we have realized the fundamental long-wavelength structure of the spectrum for the system in resonance with the $[1,1]$ star. The complexity of $H_{\text{eff}}^{(\theta)}$ compared to the Dirac matrix will soon become evident in the novel physics presented in the numerical spectra. However, this effective Hamiltonian provides great theoretical insight and illustrates the low-energy character of the bands. Namely, the spectrum begins with a Dirac cone (at origin $-\gamma\zeta\left(3\Omega_{-}^{2}\right)\left(2+\delta V\right)^{-1}$) and three planes (oriented along the $\hat{q}_j^{(\theta)}$ with intercept $\delta\tilde{V}$), coupled by complex numbers of modulus Ω_+ which are intrinsic to the commensuration angle.

We observe that $H_{\text{eff}}^{(\theta)}$ has only a minor dependence on ζ in two elements which may be ignored when ζ is sufficiently small. For this reason, we will approximate this theory as

$$H_{\text{weak}}^{(\theta)} = \gamma \begin{pmatrix} 0 & (\kappa_x - i\kappa_y) & e^{-i\frac{2\pi}{3}}\Omega^{(\theta)} & e^{i\frac{2\pi}{3}}\Omega^{(\theta)} & \Omega^{(\theta)} \\ (\kappa_x + i\kappa_y) & 0 & \Omega^{(\theta)} & \Omega^{(\theta)} & \Omega^{(\theta)} \\ e^{i\frac{2\pi}{3}}\Omega^{(\theta)} & \Omega^{(\theta)} & \vec{\kappa}\cdot\hat{q}_1^{(\theta)} + \delta\tilde{V} & 0 & 0 \\ e^{-i\frac{2\pi}{3}}\Omega^{(\theta)} & \Omega^{(\theta)} & 0 & \vec{\kappa}\cdot\hat{q}_2^{(\theta)} + \delta\tilde{V} & 0 \\ \Omega^{(\theta)} & \Omega^{(\theta)} & 0 & 0 & \vec{\kappa}\cdot\hat{q}_3^{(\theta)} + \delta\tilde{V} \end{pmatrix} \tag{4.12}$$

where

$$\Omega^{(0)} \equiv \left(\sqrt{3}+1\right)/2$$
$$\Omega^{(\theta_1)} \equiv \cos(\theta_1) - \sin(\theta_1)$$
$$\vec{\kappa} = \left(\frac{\hbar v_F}{\gamma}\right)\vec{k}$$

which holds as an effective theory of resonance with the $[1,1]$ star for weak effective coupling. Also recall that in Section 3.2.1 we claimed that the γ scaling convention was most appropriate for describing the physics in the limit of small energies and long-wavelength. This intuition is manifest exactly in our weak effective theory $H^{(\theta)}_{\text{weak}}$, which is completely independent of the scale of $\left|\vec{q}_1^{(\theta)}\right|$ and is a Schrieffer-Wolff theory valid in precisely the same limit, within the resonant region $\mathbb{L}_{1,1}$ with small ζ. Furthermore, we witness the emergence of the new dimensionless wavevector scale $\vec{\kappa}$ predicted in that section.

4.2.1 Subtle Commensuration Dependence

Closer inspection of our general effective theory of resonance with the $[1,1]$ star, $H^{(\theta)}_{\text{eff}}$, reveals an important dependence on the commensuration angle θ. Recall that the $\hat{q}_j^{(\theta)}$ depend very simply on the commensuration angle, a global rotation by θ and a scale constant (cf. Equation 2.14). Beyond this distinction, the commensuration angle enters only through the

intrinsic coupling constants

$$\theta = 0 : \begin{cases} \Omega_+ = \Omega^{(0)} = \left(\sqrt{3}+1\right)/2 \approx 1.366 \\ \Omega_- = \left(\sqrt{3}-1\right)/2 \approx 0.366 \\ \Omega_+ - \Omega_- = 1 \end{cases} \tag{4.13}$$

$$\theta = \theta_1 : \begin{cases} \Omega_+ = \Omega^{(\theta_1)} = \cos(\theta_1) - \sin(\theta_1) \approx 0.167 \\ \Omega_- = \cos(\theta_1) + \sin(\theta_1) \approx 1.404 \\ \Omega_+ - \Omega_- = -2\sin(\theta_1) \approx -1.237 \end{cases} \tag{4.14}$$

which are real numbers of roughly order unity. Therefore, our effective theory predicts some qualitative similarity in the spectrum of wildly different physical systems—resonant bilayers with twist angles near 0 and near 38.21° when their other parameters (ζ and δV) are similar. In the next chapter, we verify this prediction in a very important way by showing that the commensuration angle θ has only a geometric impact on the bands but no topological impact within the resonant regime (cf. Section 5.2.2).

4.2.2 Scale Invariance

In the last section, we used our general effective theory to justify a prediction of qualitative similarity between appropriate resonant systems with vastly different total rotation angles, near different commensuration angles. However, there is a similar and even more fundamental observation that can be made from our weak effective theory.

Consider the transformation

$$\left(\vec{k}, \gamma, \delta V\right) \mapsto \lambda\left(\vec{k}, \gamma, \delta V\right) \tag{4.15}$$

for $\lambda > 0$ and observe that both

$$\vec{\kappa} = (\hbar v_F)\, \vec{k}/\gamma$$
$$\delta\tilde{V} = \delta V/\zeta = \hbar v_F \left|\vec{q}_1^{(\theta)}\right| \delta V/\gamma$$

are invariant under this transformation. Therefore, by treating $\delta\tilde{V}$ as an independent parameter, we observe that

$$H^{(\theta)}_{\text{weak}} \mapsto \lambda H^{(\theta)}_{\text{weak}} \tag{4.16}$$

under Transformation 4.15. Thus the weak effective theory of $[1, 1]$ resonance is scale-invariant. Since the weak effective theory is scale-invariant, the dispersion of systems in resonance with the $[1, 1]$ star must be scale invariant in the limit of weak effective coupling ζ. Consider what this implies about the spectrum in resonance with the $[1, 1]$ star within the resonant region. Suppose we begin with a particular set of parameters, including interlayer coupling value γ', bias deviation $\delta V'$, and sample the spectrum at energy ε'. If we increase the coupling arbitrarily to γ'' but simultaneously expand our view of the spectrum in $\vec{k}$ space by precisely γ''/γ' and change the bias deviation to $(\gamma''/\gamma')\, \delta V'$, then the new spectrum will appear asymptotically identical at energy $(\gamma''/\gamma')\, \varepsilon'$ in the limit of small ζ.

In other words, we predict that the bands are not only topologically invariant, but *exactly geometrically invariant* to any change in the other parameters (besides θ) except for a global scale factor in both the wavevector and energy.

This is an important theoretical insight which can not be fully demonstrated graphically by any finite collection of spectra. However, we indeed report having witnessed its effect countless times and will comment further on its manifestation in the next chapter. Moreover, the effective theories reveal that in the limit of sufficiently small ζ the spectrum must be independent of ζ which we also verify numerically in Section 5.2.2.

4.3 Solution to the Effective Theory

A clear objective would be to evaluate the exact spectra of our general effective theory for resonance with the $[1,1]$ star. However, $H_{\text{eff}}^{(\theta)}$ has dimension 5 and therefore eigenvalues given by the roots of a degree 5 polynomial. As mentioned in Section 2.2.2, the Abel-Ruffini theorem proved that there are no *algebraic* solution for the roots of a general degree 5 polynomial. While certain symmetries can exist in quintics to allow for algebraic roots, discovery of closed-form, algebraic eigenvalue functions of $H_{\text{eff}}^{(\theta)}$ have eluded us for a considerable time, despite use of manual and computer algebra techniques. We are inclined to believe that they do not exist.

4.3.1 Existence of Closed-Form

However, it is possible to show that the spectrum of our effective theory exists in closed-form, simply outside the space of algebraic functions. Mathematicians have studied the problem of solving for the roots of the general quintic polynomial for centuries. In 1683, the Tchirnhaus transformation was discovered, an invertible mapping between pairs of same-degree polynomials and their roots. Tchirnhaus transformations can be used to effectively reduce the number of free parameters in a quintic by creating a new quintic with fewer degrees of freedom and roots which may be mapped onto the original roots by the inverse of the transformation.

Let us define a few classes of quintic polynomials

$$\begin{aligned}
a_5W^5 + a_4W^4 + a_3W^3 + a_2W^2 + a_1W + a_0 = 0 \qquad & \text{general form (6)} \\
W^5 + a_4'W^4 + a_3'W^3 + a_2'W^2 + a_1'W + a_0' = 0 \qquad & \text{standard form (5)} \\
X^5 + b_2X^2 + b_1X + b_0 = 0 \qquad & \text{principal form (3)} \\
Y^5 + c_1Y + c_0 = 0 \qquad & \text{Bring form (2)} \\
Z^5 - Z + d_0 = 0 \qquad & \text{Bring-Jerrard form (1)}
\end{aligned}$$

where the parenthetical number beside each name is the number of free coefficients in each polynomial (in capital variables). Obviously it is trivial to transform an equation for the roots of a quintic from general to standard form. Also note that the resultant of two polynomials is proportional to the product of differences in the roots of each. Tchirnhaus showed that a quadratic Tchirnhaus transformation can be used to create a principle quintic from a standard one, by eliminating degrees of freedom in the resultant of the quintic and $X = W^2 + \xi_1 W + \xi_0$.[33] Specifically, one may begin with any standard quintic and construct a quadratic Tchirnhaus transformation which generates a particular principal quintic with coefficients given by algebraic functions of the standard coefficients, and the roots of the standard quintic are given by the inverse transformation of the roots of the principal quintic.

Similarly, a principal quintic may be brought through Bring form [34] and into Bring-Jerrard form [35] by additional Tchirnhaus transformations. Closed-form solutions to the Bring-Jerrard quintic were found in the late 19^{th} century and may be expressed in terms of hypergeometric functions [36] as well as Jacobi elliptic theta functions.[37, 38, 39] Therefore, closed-form, nonperturbative, exact solutions to our general effective theory $H_{\text{eff}}^{(\theta)}$ *exist*.

These difficult Tchirnhaus transformations have been implemented in Mathematica [40] and we followed this work. However, these solutions would be prohibitively large to even be written here. Nevertheless, the existence of these solutions is very important because it shows that we have indeed found an exactly solvable limit of $[1, 1]$ resonant graphene bilayers.

4.3.2 Algebraic Exact Limits

While closed-forms of the general eigenvalues of $H_{\text{eff}}^{(\theta)}$ can not be written succinctly, we have already demonstrated some of the critial theoretical insights this form provides and we will highlight additional ones in Chapter 6. Presently, we will conclude this chapter by

providing the exact solutions to our effective theory in two precise limits.

Recall that

$$\Omega_{\pm} = \begin{cases} \left(\sqrt{3} \pm 1\right)/2 & \text{if} \quad \theta = 0 \\ \cos(\theta_1) \mp \sin(\theta_1) & \text{if} \quad \theta = \theta_1 \end{cases} \tag{4.17}$$

and we compute the exact effective spectrum at zero wavevector to be

$$\left(H^{(\theta)}_{\text{weak}}|_{\vec{k}=\vec{0}}\right)\vec{\psi}_n = \varepsilon_n\vec{\psi}_n$$

$$\Downarrow$$

$$\begin{cases} \varepsilon_{-2} = \varepsilon_{-1} = -\gamma\Omega^{(\theta)}\sqrt{3}\left[\sqrt{1+\left(\frac{\delta\tilde{V}}{2\sqrt{3}\Omega^{(\theta)}}\right)^2} - \left(\frac{\delta\tilde{V}}{2\sqrt{3}\Omega^{(\theta)}}\right)\right] \\ \varepsilon_0 = \gamma\delta\tilde{V} \\ \varepsilon_1 = \varepsilon_2 = \gamma\Omega^{(\theta)}\sqrt{3}\left[\sqrt{1+\left(\frac{\delta\tilde{V}}{2\sqrt{3}\Omega^{(\theta)}}\right)^2} + \left(\frac{\delta\tilde{V}}{2\sqrt{3}\Omega^{(\theta)}}\right)\right] \end{cases} \tag{4.18}$$

in the limit of weak effective coupling. Conversely, the exact spectrum of $H^{(\theta)}_{\text{eff}}$ at zero wavevector is

$$\left(H^{(\theta)}_{\text{eff}}|_{\vec{k}=\vec{0},\delta\tilde{V}=0}\right)\vec{\psi}_n = \varepsilon_n\vec{\psi}_n$$

$$\Downarrow$$

$$\begin{cases} \varepsilon_{-2} = \varepsilon_{-1} = -\gamma\Omega_+\sqrt{3}\left[\sqrt{1+\left(\frac{\sqrt{3}\zeta\Omega_-^2}{4\Omega_+}\right)^2} + \left(\frac{\sqrt{3}\zeta\Omega_-^2}{4\Omega_+}\right)\right] \\ \varepsilon_0 = 0 \\ \varepsilon_1 = \varepsilon_2 = \gamma\Omega_+\sqrt{3}\left[\sqrt{1+\left(\frac{\sqrt{3}\zeta\Omega_-^2}{4\Omega_+}\right)^2} - \left(\frac{\sqrt{3}\zeta\Omega_-^2}{4\Omega_+}\right)\right] \end{cases} \tag{4.19}$$

at perfect resonance with the $[1,1]$ star, where $\delta\tilde{V} = 0 = \delta V$.

CHAPTER 5

NUMERICAL SPECTRA AND LIFSHITZ TRANSITIONS

In this chapter we will at last examine some of the dispersion spectra which emerge from twisted graphene bilayers with resonant bias energies. For now we focus on viewing these spectra as contour plots constituting level sets of $\varepsilon\left(\vec{k}\right)$. These contours represent possible Fermi surfaces and we will illustrate that the nonperturbative physics created by resonance produces novel Lifshitz transitions not present in un-biased bilayers. We will also verify numerically some of the claims made in the previous chapter using our effective theories for $[1,1]$ resonance. The main result of this chapter appears as well in Ref. [30].

5.1 Numerical Landscape

We are now sufficiently prepared to select values of all physical parameters and use Mathematica to generate a Hamiltonian of arbitrary order which depends on two real variables $k_x = \vec{k} \cdot \hat{x}$ and $k_y = \vec{k} \cdot \hat{y}$ taken from the superlattice Brillouin zone. We discretize the domain into a finite mesh of $\vec{k}$ tuples and evaluate $H^{(\theta)}_{n,r,s}$ at each domain point, a purely numerical matrix of dimension $3n\,(n+1)+2$. We collect these spectra and produce various visualizations of the continuous dispersion in the twisted bilayer.

5.1.1 Parameter Space

In Section 3.2.2 we noted that our original theory for twisted bilayer graphene depends on 6 parameters $\{\gamma, \theta, \delta\theta, a, v_F, V\}$. This means that all possible dispersion relations lie in a very large, continuous parameter space of dimension 6. By restricting our search to experimentally measured values of $\{a, v_F\}$, experimentally relevant sets of values for others ($\gamma \in \{330, 20, 7\}\mathrm{meV}$, $\theta \in \{0, 38.21\pi/180\}$), and considering only resonant bias energies, this space may be reduced. When restricted in this way, we have 5 parameters

Table 5.1: Parameter dependence across a spectrum of effective coupling ζ for three bilayer graphene systems—twisted near 0 commensuration with and without h-BN interlayer, and near $\theta_1 = 38.21\pi/180$ (cf. Section 3.2.2). Namely, the values of the deviation angle and bias energies for $[1,1]$ and $[3,2]$ resonant systems. Recall that $V_{r,s}$ is the perfect resonant bias energy for the $[r,s]$ star (cf. Equation 3.1).

	$\theta = 0 \quad \gamma = 330\text{meV}$			$\theta = 0 \quad \gamma = 20\text{meV}$			$\theta = \theta_1 \quad \gamma = 7\text{meV}$		
ζ	$\delta\theta$ $(^\circ)$	$V_{1,1}$ (meV)	$V_{3,2}$ (meV)	$\delta\theta$ $(^\circ)$	$V_{1,1}$ (meV)	$V_{3,2}$ (meV)	$\delta\theta$ $(^\circ)$	$V_{1,1}$ (meV)	$V_{3,2}$ (meV)
0.05	34.24	6600	17461	2.045	400.0	1058	0.2705	140.0	370.4
0.10	16.93	3300	8731	1.022	200.0	529.2	0.1352	70.00	185.2
0.20	8.44	1650	4365	0.511	100.0	264.6	0.0676	35.00	92.60
0.30	5.62	1100	2910	0.341	66.67	176.4	0.0451	23.33	61.73
0.40	4.22	825.0	2183	0.256	50.00	132.3	0.0338	17.50	46.30
0.50	3.37	660.0	1746	0.204	40.00	105.8	0.0270	14.00	37.04
0.75	2.25	440.0	1164	0.136	26.67	70.55	0.0180	9.33	24.69
1.00	1.69	330.0	873.1	0.102	20.00	52.92	0.0135	7.00	18.52
1.25	1.35	264.0	698.5	0.082	16.00	42.33	0.0108	5.60	14.82
1.50	1.12	220.0	582.1	0.068	13.33	35.28	0.0090	4.67	12.35
1.75	0.96	188.6	498.9	0.058	11.43	30.24	0.0077	4.00	10.58
2.00	0.84	165.0	436.55	0.051	10.00	26.46	0.0068	3.50	9.26
3.00	0.56	110.0	291.0	0.034	6.67	17.64	0.0045	2.33	6.17
4.00	0.42	82.50	218.3	0.026	5.00	13.23	0.0034	1.75	4.63
5.00	0.34	66.00	174.6	0.020	4.00	10.58	0.0027	1.40	3.70

$\{\gamma, \theta, \delta\theta, V_{r,s}, \delta V\}$ but only a 3 dimensional unbound parameter space.

A great amount of time was spent exploring this parameter space, and our theoretical insights allow us to prevail in practice by exchanging some fundamental parameters in favor of the composite ones in Equation 3.11, limiting our search to a few resonant stars, and focusing our view primarily to the resonant region (cf. Section 3.2.3). In this way, the ζ parameter may provide the majority of the continuous parameter control in some limits. Table 5.1 shows some of the possible parameter regimes we might explore across a range of the effective coupling parameter, ζ.

5.1.2 Verify Effective Theory

We first verify the validity of our effective theory $H^{(\theta)}_{\text{eff}}$ (cf. Equation 4.11). Figure 5.1 shows a single energy level set of the spectrum of $H^{(0)}_{1,1,1}$ in green and the same level set of $H^{(0)}_{\text{eff}}$ in purple. The coupling strength γ is the same in both images, and the effective coupling ζ is controlled via the deviation angle $\delta\theta$. First, we note that the contours show agreement which improves as the wavevector diminishes, which aligns with expectation since we truncated the effective theory to linear order in $\left|\vec{k}\right| \left|\vec{q}_1^{(\theta)}\right|^{-1}$. Moreover, we observe greater agreement for smaller ζ as predicted. Finally, we observe that even where exact geometric agreement is no longer present, topological agreement between the two theories persists over a larger region of the domain. Also note that the bias is tuned into *imperfect* $[1,1]$ resonance to illustrate the validity of those terms in $H^{(0)}_{\text{eff}}$ as well.

We may draw precisely the same conclusions from Figure 5.2 regarding the validity of effective theory $H^{(\theta_1)}_{\text{eff}}$ for bilayers twisted near angle $38.21\pi/180$ and cast into even imperfect bias resonance with the $[1,1]$ star.

5.1.3 Demonstrate Scale Invariance

In Section 4.2.2 we showed that the weak effective theory is scale invariant. To demonstrate this effect, consider Figure 5.3, which displays the spectrum of the original theory $H^{(0)}_{1,1,1}$, not that of $H^{(0)}_{\text{eff}}$ or $H^{(0)}_{\text{weak}}$. Notice that this figure uses artificially small values of γ in order to clearly demonstrate this important feature of the spectra. The figure displays a selection of energy level sets which are chosen proportionally to γ and that the value of γ differs by a factor of 10 between the two images. Observe that both contour maps are plotted over the same size domain in the dimensionless scale $\vec{\kappa}$, but indeed in absolute terms the image in Figure 5.3b is on a scale 10 times smaller in actual wavevector and comprises a section of the BZ which is 10 times smaller in linear dimensions. Despite the great difference in coupling strength and effective coupling strength, the two contour plots are nigh-imperceptibly different, they are geometrically identical on this scale. This is

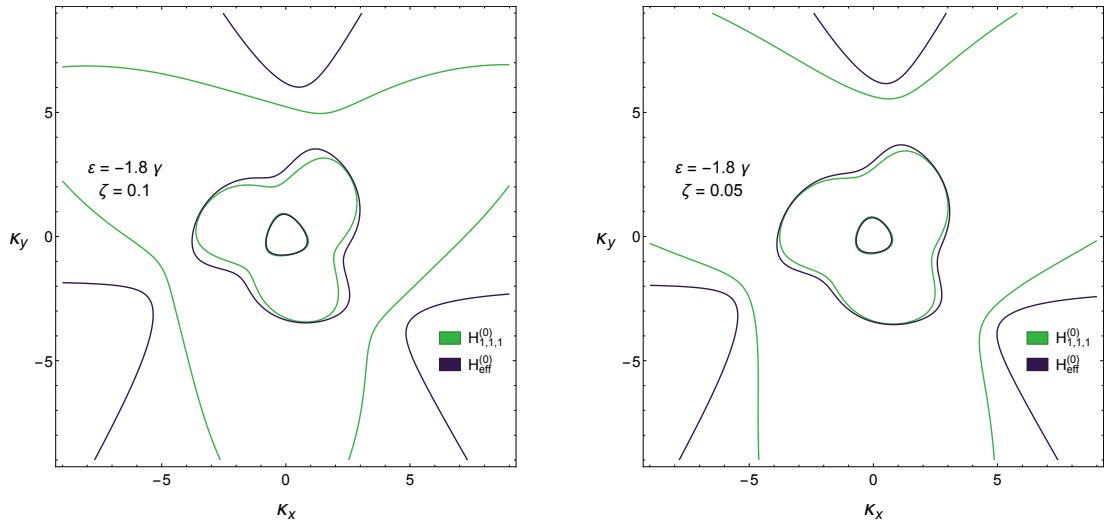

(a) Additionally, $\zeta = 0.1$, $\delta\theta = 1.02\pi/180$, $V = 202\text{meV}$, and the Brillouin zone radius is $|\vec{\kappa}|_{\text{max}} = \zeta^{-1} = 10$

(b) Additionally, $\zeta = 0.05$, $\delta\theta = 2.04\pi/180$, $V = 404\text{meV}$, and the Brillouin zone radius is $|\vec{\kappa}|_{\text{max}} = \zeta^{-1} = 20$

Figure 5.1: Energy $-1.8\gamma = -36\text{meV}$ level set of both $H^{(0)}_{1,1,1}$ and effective theory $H^{(0)}_{\text{eff}}$. The dimensionless wavevector scale is $\vec{\kappa} \equiv \left(\frac{\hbar v_F}{\gamma}\right)\vec{k}$. Both figures use $\gamma = 20\text{meV}$, $\delta V = 0.01$, $\theta = 0$, $a = 1.42\text{Å}$, and $v_F = 10^{16}\text{Å/s}$.

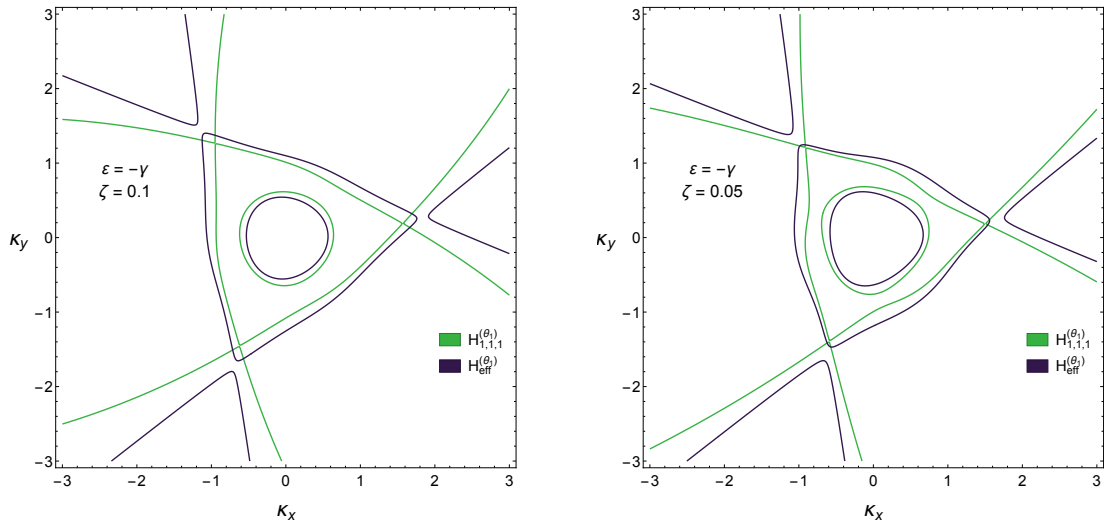

(a) Additionally, $\zeta = 0.1$, $\delta\theta = 0.135\pi/180$, $V = 69.3\text{meV}$, and the Brillouin zone radius is $|\vec{\kappa}|_{\text{max}} = \zeta^{-1} = 10$

(b) Additionally, $\zeta = 0.05$, $\delta\theta = 0.270\pi/180$, $V = 138.6\text{meV}$, and the Brillouin zone radius is $|\vec{\kappa}|_{\text{max}} = \zeta^{-1} = 20$

Figure 5.2: Energy $-\gamma = -7\text{meV}$ level set of both $H^{(\theta_1)}_{1,1,1}$ and effective theory $H^{(\theta_1)}_{\text{eff}}$. The dimensionless wavevector scale is $\vec{\kappa} \equiv \left(\frac{\hbar v_F}{\gamma}\right)\vec{k}$. Both figures use $\gamma = 7\text{meV}$, $\delta V = -0.01$, $\theta = 38.21\pi/180$, $a = 1.42\text{Å}$, and $v_F = 10^{16}\text{Å/s}$.

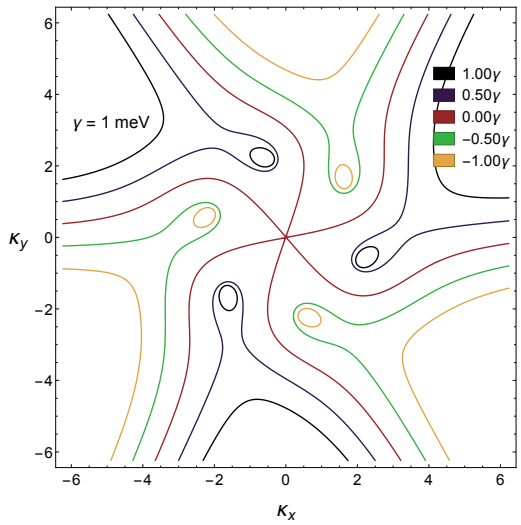

(a) Additionally, $\gamma = 1\text{meV}$, $\zeta = 5.11 \times 10^{-3}$ and the Brillouin zone radius is $|\vec{\kappa}|_{\max} = \zeta^{-1} = 195.6$.

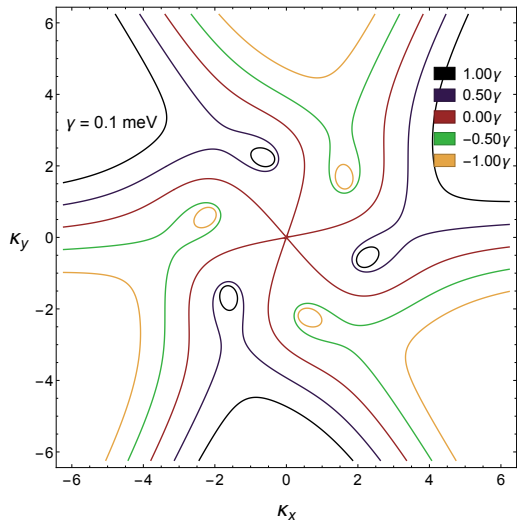

(b) Additonally, $\gamma = 0.1\text{meV}$, $\zeta = 5.11 \times 10^{-4}$ and the Brillouin zone radius is $|\vec{\kappa}|_{\max} = \zeta^{-1} = 1956$.

Figure 5.3: A sample of several energy level sets in the dispersion of $H^{(0)}_{1,1,1}$. The dimensionless wavevector scale is $\vec{\kappa} \equiv \left(\frac{\hbar v_F}{\gamma}\right)\vec{k}$. Both plots have deviation angle $\delta\theta = \pi/180$ and perfect $[1,1]$ resonance $\delta V = 0$, $V = 195.6\text{meV}$, along with $a = 1.42\text{Å}$, $v_F = 10^{16}\text{Å/s}$.

precisely the consequence of the asymptotic scale-invariance for weak effective coupling. Therefore, for sufficiently small ζ, changes in $\vec{k}$, γ, δV, and ε are immaterial beyond a global scaling, as predicted in Section 4.2.2.

5.1.4 Novel Lifshitz Transitions

We mentioned in Chapter 1 that only a single Lifshitz transition appears in the spectrum of non-biased bilayer graphene, namely in AB stacked Bernal bilayers ($\Theta = \pi/3$ in our convention). No Lifshitz transitions are known to appear in AA stacked bilayers ($\Theta = 0$). However, in stark contrast, exploring the rich parameter space we have created for resonant bilayer graphene reveals seemingly arbitrarily many possible Fermi surfaces which are topologically distinct and produce novel Lifshitz transitions. Simply stated, without any restriction on ζ or $V_{r,s}$ we can not make any further intelligible characterization of these transitions in general, the possibilities are simply immense.

Table 5.2: A summary of the topological equivalence class (cf. 3.2) of the energy level sets shown in Figure 5.4.

level sets $\varepsilon\left(\vec{k}\right) = \varepsilon_F$	
ε_F	Topological Equivalence Class
-3.00γ	$\mathcal{T}$
-1.79γ	$\mathcal{T}$
-1.76γ	$\mathcal{R}$
-0.77γ	$\mathcal{R}$
-0.74γ	$\mathcal{V}$
0.31γ	$\mathcal{V}$
0.34γ	$\mathcal{R}$
1.65γ	$\mathcal{R}$
1.68γ	$\mathcal{T}$
1.80γ	$\mathcal{T}$

5.2 Universal Lifshitz Transitions

In this section we present the most important result of this chapter, a regime for which we are capable of making a universal prediction of topological phase transitions.

5.2.1 Universal Word

Let us begin by inspecting the spectrum of $H^{(0)}_{1,1,1}$ shown in Figure 5.4. These figures display a careful selection of energy level sets proportional to γ which is given the value present in h-BN laced twisted bilayer graphene. Observe that the level set at -3.00γ is topologically equivalent to the canonical state $\mathcal{T}$ defined in Figure 3.2. The surface remains homeomorphic across the intervening energies towards the surface displayed at energy -1.79γ in green. This green state is also a member of the $\mathcal{T}$ equivalence class. However, observe that the surface at -1.76γ (red) is not equivalent, a topological phase transition has occurred on the interval $(-1.79, -1.76)\,\gamma$. This new state is equivalent to $\mathcal{R}$ and the surfaces up to and including the state at -0.77γ (purple) remain equivalent to $\mathcal{R}$. Another topological phase transition occurs on $(-0.77, -0.74)\,\gamma$ and the $\mathcal{V}$ state (black) emerges. The $\mathcal{V}$ state persists

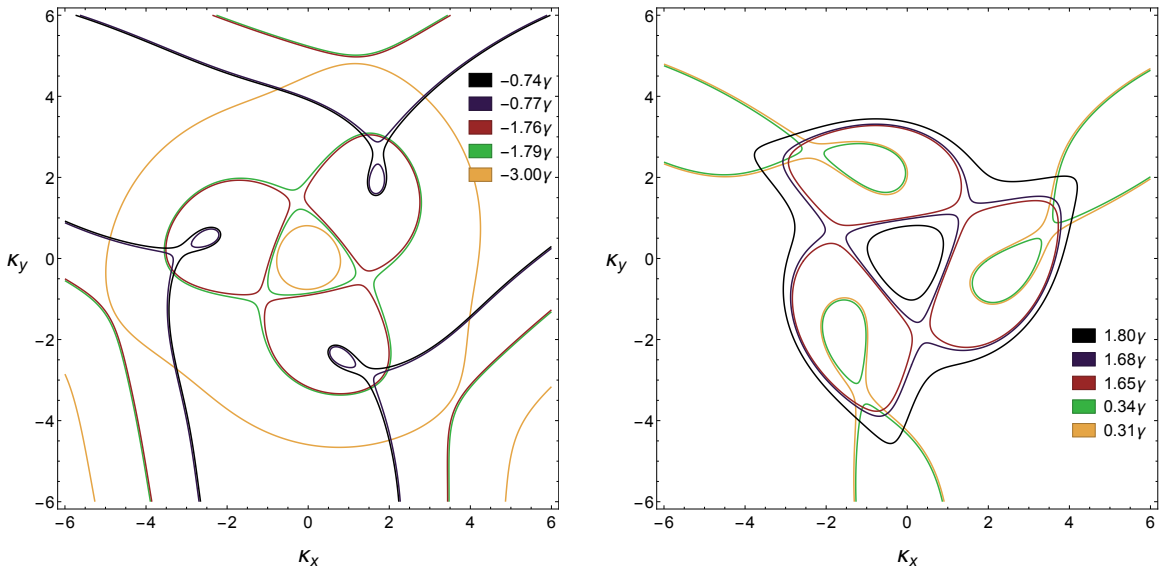

Figure 5.4: A sample of dispersion contours of $H^{(0)}_{1,1,1}$ within $\mathbb{L}_{1,1}$ which exhibit topological word $\mathcal{TRVRT}$. The dimensionless wavevector scale is $\vec{\kappa} \equiv \left(\frac{\hbar v_F}{\gamma}\right)\vec{k}$.
Parameters: $\zeta = 0.08$, $\theta = 0$, $\delta\theta = 1.28\pi/180$, $\gamma = 20\text{meV}$, $\delta V = 0$, $V = 250\text{meV}$, $a = 1.42\text{Å}$, $v_F = 10^{16}\text{Å/s}$. The Brillouin zone radius is $|\vec{\kappa}|_{\text{max}} = \zeta^{-1} = 12.5$.

up to energy 0.31γ (orange) shown in the figure on the right side. Another topological phase transition returns the state to $\mathcal{R}$ at 0.34γ (green). This state remains until at least 1.65γ (red) and then undergoes another transition into the $\mathcal{T}$ state (purple). This sequence is summarized in Table 5.2. Therefore, we can describe this evolution of the Fermi surface in Figure 5.4 precisely by topological word $\mathcal{TRVRT}$.

Inspection of Figures 5.5, 5.6, and 5.7 reveal the same, the exact same topological word $\mathcal{TRVRT}$ describes the evolution of the Fermi surface in every case.

5.2.2 Universal Regime

Let us reflect now on the significance of our last statement. First, recall that in Section 4.2.1 we predicted that the commensuration angle would have only a geometric impact on the structure of the bands in the limits where our effective theory holds. We see this prediction come true by comparing Figures 5.4 and 5.5, or by comparing Figures 5.6 and 5.7. While the bands of the bilayer twisted at a small deflection angle from AA are clearly distinct

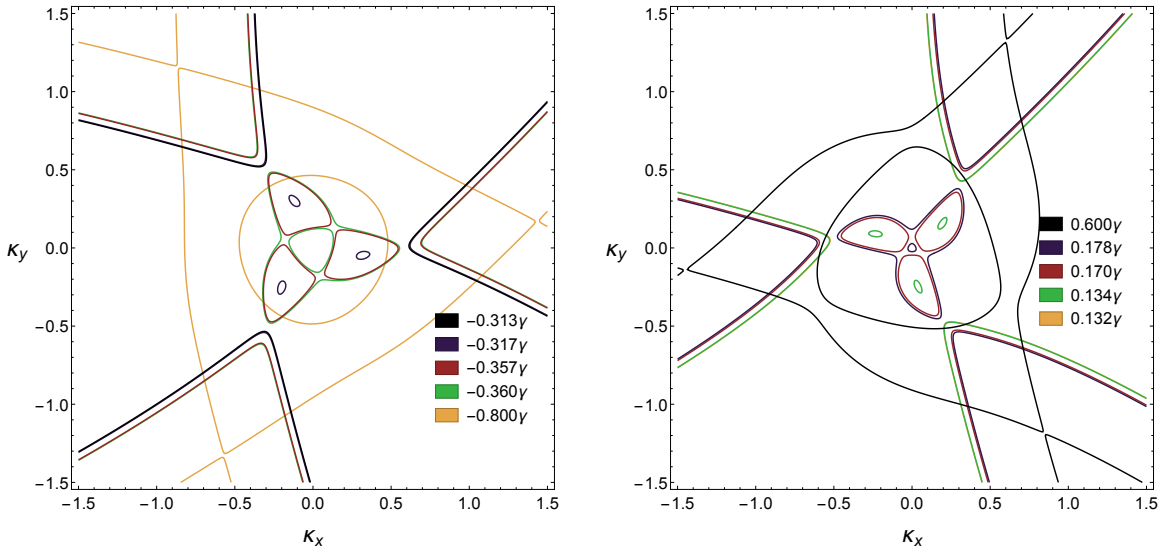

Figure 5.5: A sample of dispersion contours of $H^{(\theta_1)}_{1,1,1}$ within $\mathbb{L}_{1,1}$ which exhibit topological word $\mathcal{TRVRT}$. The dimensionless wavevector scale is $\vec{\kappa} \equiv \left(\frac{\hbar v_F}{\gamma}\right)\vec{k}$.
Parameters: $\zeta = 0.08$, $\theta = 38.21\pi/180$, $\delta\theta = 0.169\pi/180$, $\gamma = 7\text{meV}$, $\delta V = 0$, $V = 87.5\text{meV}$, $a = 1.42\text{Å}$, $v_F = 10^{16}\text{Å/s}$. The Brillouin zone radius is $|\vec{\kappa}|_{\text{max}} = \zeta^{-1} = 12.5$.

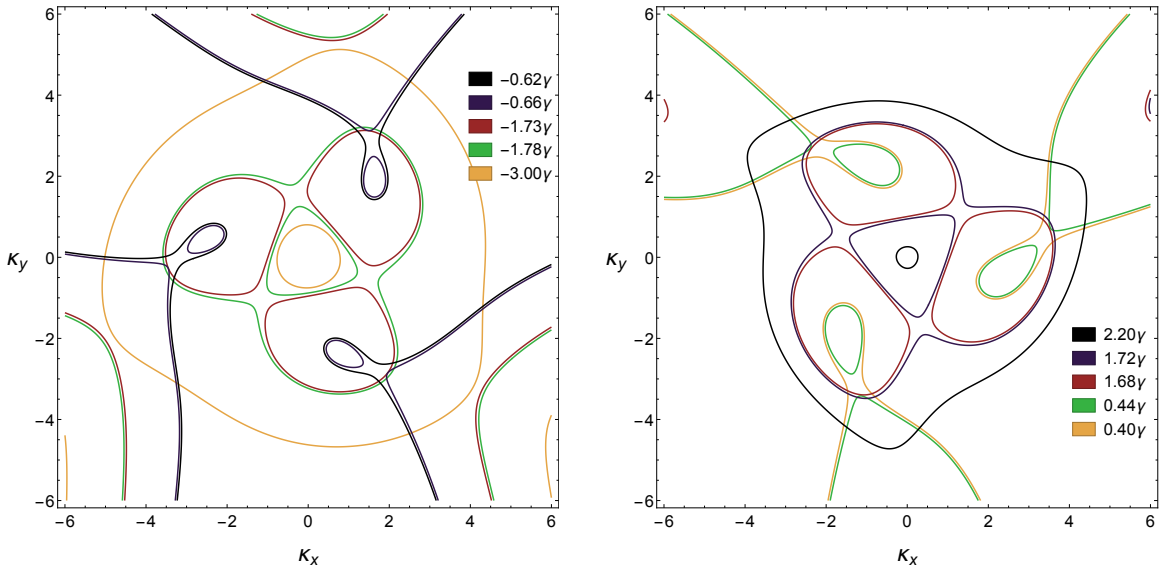

Figure 5.6: A sample of dispersion contours of $H^{(0)}_{1,1,1}$ within $\mathbb{L}_{1,1}$ which exhibit topological word $\mathcal{TRVRT}$. The dimensionless wavevector scale is $\vec{\kappa} \equiv \left(\frac{\hbar v_F}{\gamma}\right)\vec{k}$.
Parameters: $\zeta = 0.04$, $\theta = 0$, $\delta\theta = 2.56\pi/180$, $\gamma = 20\text{meV}$, $\delta V = 0$, $V = 500\text{meV}$, $a = 1.42\text{Å}$, $v_F = 10^{16}\text{Å/s}$. The Brillouin zone radius is $|\vec{\kappa}|_{\text{max}} = \zeta^{-1} = 25$.

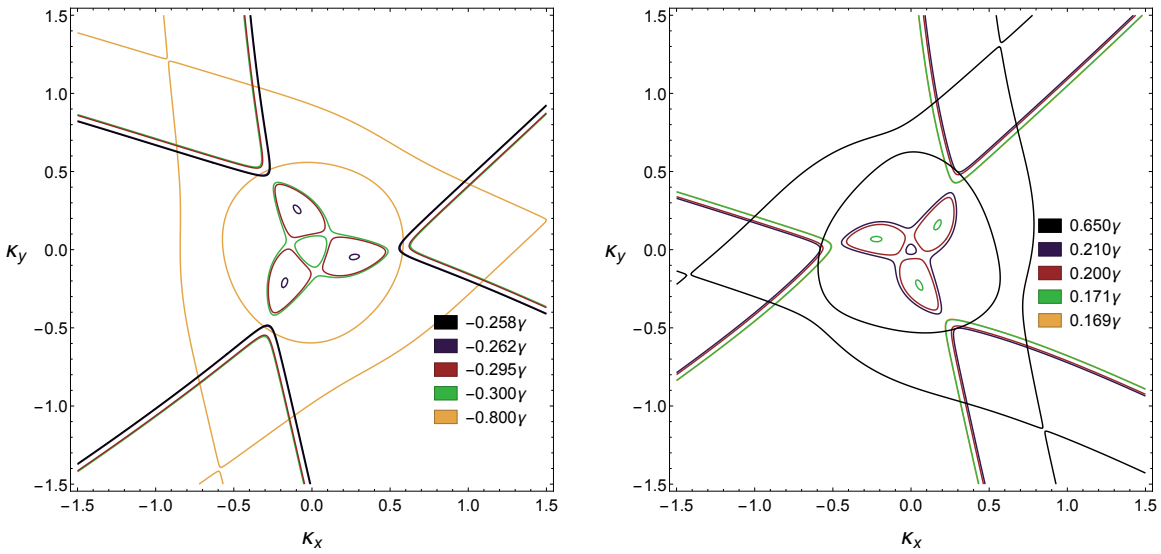

Figure 5.7: A sample of dispersion contours of $H^{(\theta_1)}_{1,1,1}$ within $\mathbb{L}_{1,1}$ which exhibit topological word $\mathcal{TRVRT}$. The dimensionless wavevector scale is $\vec{\kappa} \equiv \left(\frac{\hbar v_F}{\gamma}\right)\vec{k}$.
Parameters: $\zeta = 0.04$, $\theta = 38.21\pi/180$, $\delta\theta = 0.338\pi/180$, $\gamma = 7\text{meV}$, $\delta V = 0$, $V = 175\text{meV}$, $a = 1.42\text{Å}$, $v_F = 10^{16}\text{Å/s}$. The Brillouin zone radius is $|\vec{\kappa}|_{\text{max}} = \zeta^{-1} = 25$.

from those of a bilayer twisted at another small deflection angle from $\theta_1 = 38.21\pi/180$, the topology is the same, and we see that the same topological word $\mathcal{TRVRT}$ describes the evolution of the Fermi surface in both cases. This congruence is an empirical discovery of our numerical examination of many spectra, motivated in part by our effective theory (cf. Section 4.2.1).

Alternatively, consider the difference between Figures 5.4 and 5.6. The commensuration is $\theta = 0$ in both and coupling $\gamma = 20\text{meV}$ is held constant. However, the effective coupling ζ is reduced by a factor 2 via the deflection angle $\delta\theta$. Here we observe *significantly* less change in the contours compared to changing the commensuration. This is reflective of the scale invariance and the independence of the spectra on ζ when it is sufficiently small, as predicted in Section 4.2.2. In the case of some bands, the independence is visually perfect, but some slight geometric changes are visible at this scale. Conversely, we saw in Figure 5.3 for much smaller ζ, this independence became exact. Nonetheless, for sufficiently small ζ, the topology of the bands certainly does not change.

Similarly, comparison of Figures 5.5 and 5.7 reveals almost exact geometric independence on ζ in the bands in the case of $\theta = \theta_1$. Topological word $\mathcal{TRVRT}$ in this limit is independent of the effective coupling strength.

Recall the definition of the resonant region in Section 3.2.3. Particularly for the $[1,1]$ star in perfect resonace, $\delta V = 0$, we had simply $f_{1,1} = 1/2$. Manipulating the wavevector space restriction defined there

$$\max\left\{\left|\kappa_x\right|,\left|\kappa_y\right|\right\} = \max\left\{\left|\left(\frac{\hbar v_F}{\gamma}\right)k_x\right|,\left|\left(\frac{\hbar v_F}{\gamma}\right)k_y\right|\right\} \tag{5.1}$$

$$= \left(\frac{\hbar v_F}{\gamma}\right)\max\left\{\left|k_x\right|,\left|k_y\right|\right\} \tag{5.2}$$

$$\leq \left(\frac{\hbar v_F}{\gamma}\right) f_{r,s}\left|\vec{q}_1^{(\theta)}\right| \tag{5.3}$$

$$= f_{r,s}\zeta^{-1} \tag{5.4}$$

we obtain the restriction on the dimensionless $\vec{\kappa}$. Thus, in the case of perfect $[1,1]$ resonance and $\zeta = 0.08$ we have $\max\left\{\left|\kappa_x\right|,\left|\kappa_y\right|\right\} = 6.25$. Moreover, we showed in Equation 3.18 the restriction of the energy codomain by the resonant region. With $t = 3$ and $f_{1,1} = 1/2$ in perfect resonance, we must have $\zeta \leq 1/6 \approx 0.167$. Therefore, we see that every Figure 5.4, 5.5, 5.6, and 5.7 lies within the resonant region $\mathbb{L}_{1,1}$ in terms of $\vec{\kappa}$, ε, and ζ.

This is the *universal regime* of twisted bilayer graphene in resonance with the $[1,1]$ star, the regime of sufficiently small effective coupling, wavevector, and energy on which we postulate that the topological word is $\mathcal{TRVRT}$. For a given commensuratation and sufficiently small ζ, this follows from the independence of effective theory $H^{(\theta)}_{\text{weak}}$ on the effective coupling. Strictly speaking, this topological word is defined over a subregion of $\mathbb{L}_{1,1}$ (cf. Section 3.3.3).

5.2.3 Imperfect Resonance and Experimental Viability

The figures used in the previous section to demonstrate the universality of $\mathcal{TRVRT}$ have used Hamiltonians cast into perfect resonance with the $[1,1]$ star. By sampling a large finite set of $\delta\tilde{V}$ values, we conjecture this word to be robust to effective deviations at least as large as $\delta\tilde{V} \in [-1.5, 1.5]$. Consider Figure 5.4 where such effective deviation corresponds to deviations as large as $\delta V \in [-0.12, 0.12]$ and bias energies on the interval $V \in [220, 280]\,\mathrm{meV}$ (cf. Equations 3.10 and 3.1). This is an experimentally viable bias energy in graphene bilayers in terms of magnitude and requisite precision. Furthermore, the deviation angle of 1.28° is within experimental control and the coupling energy $\gamma = 20\mathrm{meV}$ is feasible with inclusion of hexagonal boron nitride (cf. Table 3.1). Lastly, there is a thermal broadening in real systems on the order of the temperature times the Boltzmann constant. At the boiling point of Helium, $T_{He} = 4.2\mathrm{K}$, this broadening is on the scale of $k_B T_{He} = 0.36\mathrm{meV}$. Relative to $\gamma = 20\mathrm{meV}$ this scale is $k_B T_{He} = 0.018\gamma$ which is at least an order of magnitude smaller than required to resolve the inequivalent Fermi surfaces in Figure 5.4 and observe the 4 Lifshitz transitions predicted by $\mathcal{TRVRT}$.

5.3 Beyond Universal [1,1] Resonance

A considerable effort was given to the exploration of the massive parameter space described in Section 5.1.1, but we are unable to provide such a concise and universal characterization of the general topological behavior. We can reach beyond our universal description in several ways: by increasing the effective coupling beyond around $\zeta \approx 0.17$ (cf. Section 5.2.2), considering resonance with a different star, or by expanding our characterization to a larger region of wavevector space or the energy codomain. Indeed, doing any of these things produces new transitions and even new topological states such as those defined in Figure 3.2 and many others.

We give a concise demonstration of these effects in Figure 5.8. This figure gives several

energy level sets in the dispersion of a Hamiltonian cast into resonance with the $[3,2]$ star at an effective coupling of $\zeta = 0.315$. This large ζ, particularly in conjunction with intention to view the spectrum over the entire BZ, requires use of a larger order Hamiltonian to achieve convergence. These contours were produced by dimension 218 Hamiltonian $H^{(0)}_{8,3,2}$. The top pair of images show a small window of the BZ and highlight two novel Lifshitz transitions, $\mathcal{TX}$ and $\mathcal{LN}$ respectively (cf. Figure 3.2). With the toroidal topology of the BZ in mind (cf. Section 3.3.2), the bottom pair of images hint at the extent of topological possibilities present in resonant twisted graphene bilayers.

A reader may wonder why we do not present an examination of the $\zeta \to 0$ limit for resonance with this $[3,2]$ star, especially since the $[3,2]$ star contains $m_{3,2} = 6$ sites in resonance and a resonant subspace dimension of 8. However, there is a fundamental difference between the $[3,2]$ and $[1,1]$ resonant subspaces, beyond the fact that $w_{1,1} = 5$ and $w_{3,2} = 8$. This difference is the nature of the mutual coupling within each resonant subspace. In Section 3.1.2 we made an observation about mutual coupling between sites in the hopping space, which is really a consequence of the manner in which coupling is included in this theory (cf. Section 2.2.1). All neighboring sites in $\mathbb{B}$ are coupled via γ which results in pairs of sites in general coupled by γ times a polynomial in ζ with powers given by $l-1$ for all paths of hopping length l along the edges of $\mathbb{B}$ which connect the pair of sites.

This means that in the $[1,1]$ resonant subspace, the $[1,1]$ sites are coupled to the $[0,0]$ site at lowest order γ and coupled to one another at lowest order $\gamma\zeta$. In the $\zeta \to 0$ limit the latter can be ignored and a universal regime is obtained, nontrivial physics roughly independent of ζ. Conversely, examination of Figure 2.8 reveals that the $[3,2]$ sites are coupled to $[0,0]$ at lowest order $\gamma\zeta^2$ while coupling to another $[3,2]$ site at lowest order $\gamma\zeta$ (the shortest path connecting them, via a $[4,1]$ site, has hopping length 2). It is for this reason that we cannot achieve a nontrivial universal description of $[3,2]$ resonance in any limit of ζ, no coupling to the central Dirac bands remains as $\zeta \to 0$.

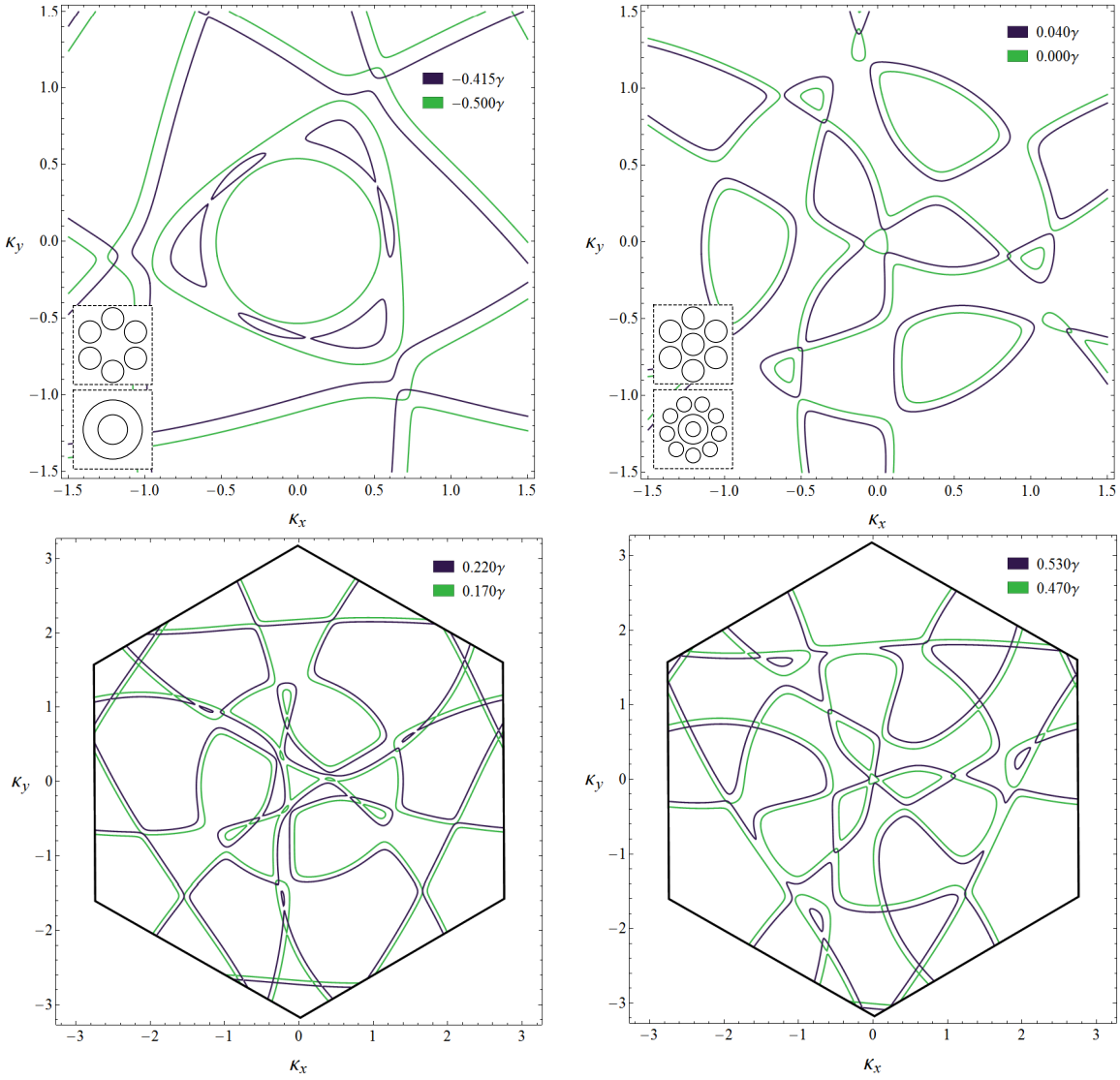

Figure 5.8: A sample of several dispersion contours of $H^{(0)}_{8,3,2}$ in perfect $[3,2]$ resonance with larger effective coupling, which exhibit some novel topological phase transitions, including $\mathcal{TX}$ and $\mathcal{LN}$ in the top row (cf. Fig. 3.2). Parameters: $\zeta = 0.315, \theta = 0, \delta\theta = 0.325\pi/180$, $\gamma = 20\text{meV}, V = 168\text{meV}$, $\delta V = 0$, $a = 1.42\text{Å}$, $v_F = 10^{16}\text{Å/s}$. The dimensionless wavevector scale is $\vec{\kappa} \equiv \left(\frac{\hbar v}{\gamma}\right)\vec{k}$ and the Brillouin zone radius is $|\vec{\kappa}|_{\text{max}} = \zeta^{-1} = 3.17$

CHAPTER 6

IMMUTABLE MAGIC RESONANCE

In Chapter 1 we mentioned that numerical examination of the existing theory demonstrates that small angle twisted bilayer graphene has a zero velocity electron state at a discrete set of so-called "magic angles."[20] However, this mysterious phenomenon remains unexplained. In this chapter, we will at last explain a similar consequence of generally twisted bilayer graphene in the presence of an external electric field by using the exactly solvable limit of our resonant theory.

6.1 Immutable State in [1,1] Resonance

We will now show that a similar state emerges at zero wavevector in our $[1, 1]$ resonant system by using our exactly solvable effective theories. We will use isolation and symmetries to show that this state has not only zero velocity but also zero curvature.

6.1.1 Isolated Nullity

We begin by examining the exact effective spectrum of perfect $[1, 1]$ resonance at zero wavevector, given by Equation 4.19. Observe that the spectrum is directly proportional to

$$\begin{cases} \varepsilon_- = -\left(\sqrt{1+y^2}+y\right) = -y-\sqrt{1+y^2} \\ \varepsilon_0 = 0 \\ \varepsilon_+ = \left(\sqrt{1+y^2}-y\right) = -y+\sqrt{1+y^2} \end{cases} \tag{6.1}$$

with $y \equiv \left(\frac{\sqrt{3}\zeta\Omega_-^2}{4\Omega_+}\right)$. Consider that

$$0 = -y \pm \sqrt{1+y^2} \quad \exists y, |y| < \infty \tag{6.2}$$

$$\iff \sqrt{1+y^2} = \mp y \tag{6.3}$$

$$\implies \left(\sqrt{1+y^2}\right)^2 = (\mp y)^2 \tag{6.4}$$

$$\iff 1 + y^2 = y^2 \tag{6.5}$$

$$\iff 1 = 0 \quad \text{(contradiction)} \tag{6.6}$$

shows that $\varepsilon_- \neq \varepsilon_0 \neq \varepsilon_+$ for any finite y. Moreover, $\varepsilon_- \neq \varepsilon_+$ for any $y \in \mathbb{R}$ so the spectrum in Equation 4.19 has no additional degeneracy beyond the two explicitly stated degenerate pairs. Therefore, the zero energy band at zero wavevector is isolated from the degenerate pairs. Let us assign this band the index z and refer to it as the *zero-band*. The isolation of the zero band is very important because it allows us to impose symmetries of the entire spectrum on this one band.

6.1.2 Zero Velocity

We first recall that the lattice $\mathbb{B}$ is $\mathcal{C}_3$ symmetric, so the dispersion relation must also be invariant to rotation by $2p\pi/3 \quad \forall p \in \mathbb{Z}$. Moreover, recall that the velocity of an electron in band n is $\vec{v}_n\left(\vec{k}\right) = \hbar^{-1}\nabla_{\vec{k}}\varepsilon_n\left(\vec{k}\right)$. However, since we showed that the zero-band is isolated at $\vec{k} = \vec{0}$ it must be itself $\mathcal{C}_3$ symmetric and therefore we must have

$$R_{2p\pi/3}\left[\nabla_{\vec{k}}\varepsilon_z\left(\vec{k}\right)\right] = \nabla_{\vec{k}}\varepsilon_z\left(\vec{k}\right) \quad \forall p \in \mathbb{Z} \tag{6.7}$$

where $R_\theta = \left(\begin{smallmatrix}\cos\theta & -\sin\theta \\ \sin\theta & \cos\theta\end{smallmatrix}\right)$ is the 2D rotation matrix and z is the index of the zero-band. The only solution to Equation 6.7 is $\vec{0} = \nabla_{\vec{k}}\varepsilon_z\left(\vec{k}\right)$, so $\vec{v}_z\left(\vec{k}\right) = \vec{0}$ and the velocity of the zero-band at $\vec{k} = \vec{0}$ must be zero.

6.1.3 Chiral Symmetry

We used the isolation of the zero-band to impose the $\mathcal{C}_3$ symmetry on this band and imply that the gradient is zero. Here we define a chiral symmetry which will allow us to show that this band also has no curvature. Let us define two transformations on a matrix $D\left(\vec{k}\right)$

$$\mathcal{P} : \vec{k} \mapsto -\vec{k} \tag{6.8}$$

$$\mathcal{S} : D \mapsto S^{\dagger} D S \tag{6.9}$$

where $\vec{k}$ is the wavevector and

$$S = \begin{pmatrix} -1 & 0 & 0 & 0 & 0 \\ 0 & -1 & 0 & 0 & 0 \\ 0 & 0 & 1 & 0 & 0 \\ 0 & 0 & 0 & 1 & 0 \\ 0 & 0 & 0 & 0 & 1 \end{pmatrix} \tag{6.10}$$

is a unitary matrix. Observe that

$$S^{\dagger}\left[H^{(\theta)}_{\text{weak}}\left(-\vec{k}\right)\right] S = -\left[H^{(\theta)}_{\text{weak}}\left(\vec{k}\right)\right] \iff \delta\tilde{V} = 0 \tag{6.11}$$

demonstrates the action of the composite transformation $\mathcal{SP}$ on the weak effective theory given by Equation 4.12. For clarity, we let

$$J_{\vec{k}} \equiv H^{(\theta)}_{\text{weak}}\left(\vec{k}\right)|_{\delta\tilde{V}=0} \tag{6.12}$$

and

$$J_{\vec{k}}\vec{\psi}_{n,\vec{k}} = \varepsilon_n\left(\vec{k}\right)\vec{\psi}_{n,\vec{k}} \tag{6.13}$$

defines the eigevectors of all bands of this Hamiltonian. Consider

$$-\varepsilon_n\left(\vec{k}\right)\left[S\vec{\psi}_{n,\vec{k}}\right] = -S\left[\varepsilon_n\left(\vec{k}\right)\vec{\psi}_{n,\vec{k}}\right] \tag{6.14}$$

$$= -S\left[J_{\vec{k}}\vec{\psi}_{n,\vec{k}}\right] \qquad \text{(by Equation 6.13)} \tag{6.15}$$

$$= -S\left[\left(-S^{\dagger}J_{-\vec{k}}S\right)\vec{\psi}_{n,\vec{k}}\right] \qquad \text{(by Equations 6.12, 6.11)} \tag{6.16}$$

$$= (-1)^2\left(SS^{\dagger}\right)J_{-\vec{k}}\left(S\vec{\psi}_{n,\vec{k}}\right) \tag{6.17}$$

$$= J_{-\vec{k}}\left[S\vec{\psi}_{n,\vec{k}}\right] \qquad \text{(since } S \text{ is unitary)} \tag{6.18}$$

$$= \varepsilon_{n'}\left(-\vec{k}\right)\left[S\vec{\psi}_{n,\vec{k}}\right] \qquad \text{(justification below)} \tag{6.19}$$

where the last equivalence follows from the fact that $-\varepsilon_n\left(\vec{k}\right)$ is a scalar which implies that $-\varepsilon_n\left(\vec{k}\right)\left[S\vec{\psi}_{n,\vec{k}}\right] = J_{-\vec{k}}\left[S\vec{\psi}_{n,\vec{k}}\right]$ must be an eigenvalue equation for $J_{-\vec{k}}$ and therefore $S\vec{\psi}_{n,\vec{k}}$ must be an eigenvector of $J_{-\vec{k}}$. Therefore

$$S^{\dagger}J_{-\vec{k}}S = -J_{\vec{k}} \implies \varepsilon_{n'}\left(-\vec{k}\right) = -\varepsilon_n\left(\vec{k}\right) \tag{6.20}$$

which means that a Hamiltonian observing the symmetry $\mathcal{SP}$, which we will denote a *chiral symmetry*, must contain a collection of bands which possess points inverted in sign at domain points which are inverted in sign. Importantly, Equation 6.11 shows that the weak effective Hamiltonian is chiral symmetric at perfect resonance.

In general, the spectrum may obey this $\mathcal{SP}$ symmetry with multiple bands. However, since the zero band is isolated at zero energy and zero wavevector, the $\mathcal{SP}$ symmetry demands

$$\varepsilon_z\left(-\vec{k}\right) = -\varepsilon_z\left(\vec{k}\right) \tag{6.21}$$

which means that the zero-band is an odd function along any direction from $\vec{k} = \vec{0}$ and the curvature is zero in every direction.

6.1.4 Immutable State

We have used isolation and symmetry to show that the zero-band of $[1, 1]$ resonant systems has zero gradient and curvature. While the velocity is proportional to the gradient and therefore zero, the effective mass tensor for the state is inversely proportional to the band Jacobian, a collection of second partial derivatives of the band in wavevector space. We saw that these curvatures are all zero by chiral symmetry, so the state effective mass is infinite.

Therefore, we refer to this zero-band state at $\vec{k} = \vec{0}$ as *immutable* precisely because it has both zero velocity and infinite mass. Therefore, not only is the state stationary, but it is profoundly robust to perturbations, as a particle with infinite mass may accept arbitrarily large, finite impulses without accelerating.

6.2 Additional Immutable States

We showed that the zero-band in $[1, 1]$ resonance is immutable, but now we would like to know if this phenomenon emerges in resonance with other stars. In addition to the $\mathcal{C}_3$ symmetry present in all twisted bilayer spectra, the necessary and sufficient conditions were the isolation of the zero-band and the chiral symmetry of the effective Hamiltonian for weak effective coupling. We will now examine the source of these properties in general resonance.

6.2.1 Extended Effective Theories

In Section 4.1 we introduced the Schrieffer-Wolff transformation and illustrated that it can be used to isolate the low energy subspace of twisted bilayer Hamiltonians. In particular, we showed that we may use this theory to obtain effective Hamiltonians for any resonant subspace, which has dimension $w_{r,s}$ in general (cf. Equation 3.4). In Section 4.2 we explicitly derived such an effective theory for systems in resonance with the $[1, 1]$ star, where

$w_{1,1} = 5$, and carefully presented this effective theory as simply as possible using limiting approximations and unitary gauge transformations. We may generalize the form of these results without manually performing these transformations for every star with which we may resonate.

To this end, let us define the unit vector $\hat{e}_{j,m}$ to be the zero vector in dimension $(2+m)$ with the j^{th} entry replaced by 1. For example, $\hat{e}_{2,1} = \begin{pmatrix} 0 & 1 & 0 \end{pmatrix}^T$ and $\hat{e}_{4,2} = \begin{pmatrix} 0 & 0 & 0 & 1 \end{pmatrix}^T$. Let us also define vectors

$$\vec{u}_{1,m} = \sum_{j=3}^{m+2} \exp\left[(j-2)\,\frac{2i\pi}{m}\right] \hat{e}_{j,m} \tag{6.22}$$

$$= \begin{pmatrix} 0 & 0 & e^{2i\pi/m} & e^{2(2)i\pi/m} & \dots & e^{2(m-1)i\pi/m} & 1 \end{pmatrix}^T$$

$$\vec{u}_{2,m} = \sum_{j=3}^{m+2} \hat{e}_{j,m} = \begin{pmatrix} 0 & 0 & 1 & 1 & \dots & 1 & 1 \end{pmatrix}^T \tag{6.23}$$

which have as well dimension $(2+m)$. We then construct *principal* matrix P_m as a Hermitian matrix of dimension $(2+m)$

$$P_m = \Omega \left[\begin{pmatrix} \vec{u}_{1,m} & \vec{u}_{2,m} & \vec{0} & \vec{0} & \dots & \vec{0} \end{pmatrix} + \begin{pmatrix} \vec{u}_{1,m} & \vec{u}_{2,m} & \vec{0} & \vec{0} & \dots & \vec{0} \end{pmatrix}^\dagger \right] \tag{6.24}$$

where $\Omega \in \mathbb{R}^+$ and $\vec{0}$ is the zero vector in dimension $(2+m)$. Consideration of the explicit form of P_3

$$P_3 = \begin{pmatrix} 0 & 0 & \Omega e^{-2i\pi/3} & \Omega e^{2i\pi/3} & \Omega \\ 0 & 0 & \Omega & \Omega & \Omega \\ \Omega e^{2i\pi/3} & \Omega & 0 & 0 & 0 \\ \Omega e^{-2i\pi/3} & \Omega & 0 & 0 & 0 \\ \Omega & \Omega & 0 & 0 & 0 \end{pmatrix} \tag{6.25}$$

reveals the connection to the effective theory of resonance with the $[1,1]$ star, namely

$$P_3 = H^{(\theta)}_{\text{weak}}|_{\vec{k}=\vec{0},\delta\tilde{V}=0} \iff \Omega = \gamma\Omega^{(\theta)} \tag{6.26}$$

where $H^{(\theta)}_{\text{weak}}$ is given by Equation 4.12. However, critically, this connection holds for some $\Omega > 0$ in general for any effective theory with resonant subspace dimension 5 (e.g. resonance with the $[3,1]$ star). In general resonance, the resonant subspace dimension is $w_{r,s}$ and the weak effective Hamiltonian has the form $P_{w_{r,s}-2}$.

6.2.2 Dimension of the Kernel

Our goal is to find all resonant stars which induce an isolated zero-band, which is to say that our goal is to find principal matrices P_m for which there is only one zero eigenvalue. We begin by finding that

$$\begin{aligned} P_m\hat{e}_{j,m} &= \Omega\vec{u}_{j,m} \qquad \forall j \in \{1,2\}, \forall m \in \mathbb{N} \\ P_m\vec{u}_{j,m} &= m\Omega\hat{e}_{j,m} \qquad \forall j \in \{1,2\}, \forall m \in \mathbb{N}\setminus\{1\} \end{aligned} \tag{6.27}$$

describe the action of the principal matrices. From these we observe that the following is true for for all $j \in \{1,2\}$ and $m \in \mathbb{N}\setminus\{1\}$

$$\begin{aligned} P_m\left[\vec{u}_{j,m} \pm \sqrt{m}\hat{e}_{j,m}\right] &= P_m\vec{u}_{j,m} \pm \sqrt{m}P_m\hat{e}_{j,m} \\ &= m\Omega\hat{e}_{j,m} \pm \sqrt{m}\Omega\vec{u}_{j,m} \qquad \text{(Eq. 6.27)} \\ &= \left(\pm\sqrt{m}\Omega\right)\left[\vec{u}_{j,m} \pm \sqrt{m}\hat{e}_{j,m}\right] \end{aligned} \tag{6.28}$$

and that $\vec{u}_{j,m} \pm \sqrt{m}\hat{e}_{j,m} \quad \forall j \in \{1,2\}$ represents 4 distinct eigenvectors of P_m if $m \geq 2$. Therefore, for all $m \geq 2$, P_m contains 4 non-zero eigenvalues: $\pm\sqrt{m}\Omega$ with multiplicity 2 each. It is trivial to check that the spectrum of P_0 is indeed 0 with multiplicity 2 in accordance with Equation 6.28 and that the spectrum of P_1 is in fact $\{-\Omega, 0, \Omega\}$.

Equipped with a lower bound on the number of nonzero eigenvalues of P_m, discovered by explicit construction of some of the eigenvectors, we turn to the remainder of the eigenspace. To this end, observe that $\vec{u}_{1,m}$ and $\vec{u}_{2,m}$ are linearly independent for all $m \geq 2$ since, in such a case, their last elements are equal and nonzero (1) while their penultimate elements are not equal (cf. Equations 6.22, 6.23). When $m \geq 2$, square matrix $\begin{pmatrix} \vec{u}_{1,m} & \vec{u}_{2,m} & \vec{0} & \vec{0} & \dots & \vec{0} \end{pmatrix}$ has dimension $2 + m \geq 4$ and precisely satisfies the conditions of Theorem A.1.1, proved in Appendix A.1. Since $\Omega > 0$, that theorem implies that the dimension of the column space of P_m is exactly 4 for $m \geq 2$ (cf. Equation 6.24).

The Rank-Nullity Theorem for square matrices demands that

$$\dim\left[\text{Null}\left(P_m\right)\right] = \dim\left(P_m\right) - \dim\left[\text{Col}\left(P_m\right)\right] \tag{6.29}$$

so, for all $m \geq 2$, we have $\dim\left[\text{Null}\left(P_m\right)\right] = (2+m) - 4 = m - 2$. Finally, then

$$\dim\left[\text{Null}\left(P_m\right)\right] = \begin{cases} |m-2| & \forall m \in \mathbb{N} \setminus \{1\} \\ 1 & m = 1 \end{cases} \tag{6.30}$$

follows from combining the result with straightforward computation of the spectrum of P_0 and P_1. Therefore

$$\dim\left[\text{Null}\left(P_m\right)\right] = 1 \iff m \in \{1, 3\} \tag{6.31}$$

and only P_1 and P_3 possess exactly 1 zero eigenvalue.

6.2.3 Connection to Effective Hamiltonians

Recall that these principal matrices were introduced to provide the general form of the weak effective Hamiltonian at zero wavevector for systems in resonance with arbitrary stars in $\mathbb{B}$. However, the dimension of these resonant subspaces are not arbitrary natural numbers,

these dimensions are $w_{r,s}$ as described in Section 3.1.1. Recall that $w_{r,s} - 2$ is constrained to be always the number of solutions to $\left|\vec{Q}\right| = Q_{r,s}$ for $\vec{Q} \in \mathbb{B}$ (cf. Equation 3.3). Simply, this quantity is the number of sites in the hopping lattice which lie on a circle of radius $Q_{r,s}$. At present, we need only to assert that this number must be a multiple of 3 since the lattice $\mathbb{B}$ is $\mathcal{C}_3$ symmetric.

In other words, the dimension of the resonant subspace for any bilayer system must be $2 + 3p \quad \exists p \in \mathbb{N}$. Since P_m has dimension $2 + m$, only principal matrices $P_{3p} \quad \exists p \in \mathbb{N}$ may correspond to effective theories of resonant graphene bilayers. Therefore principal matrix P_1 corresponds to no such effective theory and Equation 6.31 implies that P_3 alone contains exactly 1 zero eigenvalue while corresponding to an effective physical theory of resonance.

6.3 3-Stars

We have shown that all resonant subspaces of dimension 5 are described by chiral symmetric theories similar to $H^{(\theta)}_{\text{weak}}$ at weak effective coupling and must possess the immutable state. Furthermore, we showed that systems with any other resonant subspace dimension do not possess an isolated band at zero energy and wavevector and therefore do not possess this immutable state. In order to induce a resonant subspace of dimension 5 we must use a bias energy which casts into resonance exactly 3 sites in the hopping lattice. Furthermore, we know that these sites will have odd hopping number, but in general we cannot presently predict for which bias energies this occurs. We will formalize and answer this question now.

6.3.1 Degenerate Stars

In order to find these stars, it seems reasonable to begin by considering the number of sites in the r^{th} ring, which is readily seen to grow simply as $3r + \delta^0_r$. However, we know that these rings are subdivided into stars by the magnitude of the wavevectors. Finding a general

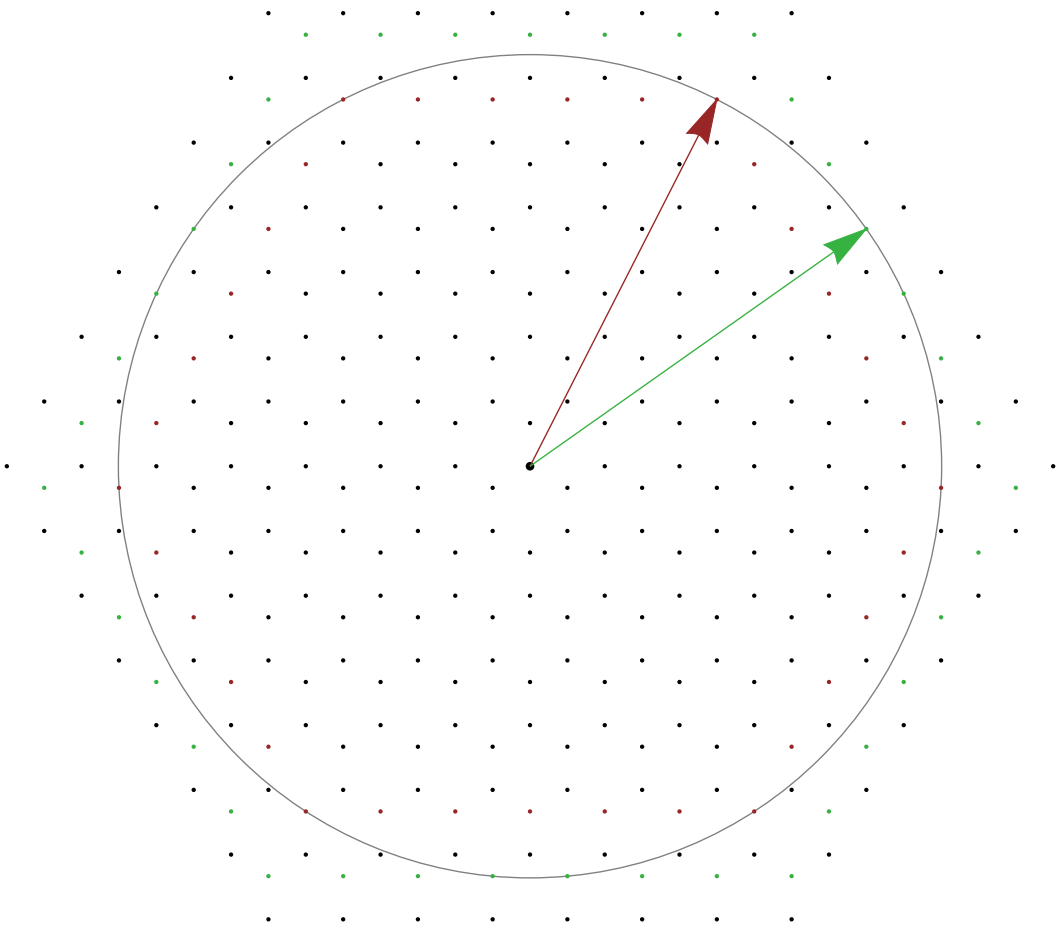

Figure 6.1: Illustrating the "overlap" in the $[11, 6]$ and $[13, 1]$ stars. The red dots are the sites of the $[11, 6]$ star and the green dots constitute the $[13, 1]$ star. Both set lie on a origin-centered circle of radius $\sqrt{91}\,|\vec{q}_1|$.

prescription for $m_{r,s}$, the number of sites in the $[r, s]$ star proves to be a difficult problem. However, we will show that it is actually not the proper question to ask, and moreover, we may obtain our desired result without it.

First, to illustrate that this is not the right question to ask, let us now disprove a result that might seem intuitive. Recall that $Q_{r,s}$ is defined as the magnitude of sites in the $[r, s]$ star. One might expect these $Q_{r,s}$ to uniquely specify $[r, s]$, but they do not. We illustrate the smallest counterexample to this assumption in Figure 6.1.

Figure 6.1 shows the first 14 rings of $\mathbb{B}$. The 11^{th} ring is highlighted in red and the 13^{th} ring in green. The red vector shown is $\vec{F}_1 = 6\vec{q}_1 - 5\vec{q}_2 = \vec{q}_1 - 5\vec{g}_1$ and the green vector is

$\vec{F}_2 = 4\vec{q}_1 - 6\vec{q}_2 + 3\vec{q}_3 = \vec{q}_1 - 6\vec{g}_1 + 3\vec{q}_3$ (cf. Equation 2.8). These vectors clearly belong to different stars as their hopping numbers differ. Their hopping numbers are $\langle \vec{F}_1, \vec{0} \rangle_L = 11$ and $\langle \vec{F}_2, \vec{0} \rangle_L = 13$, but we see that they lie on the same circle centered at the origin. Indeed $\vec{F}_1$ lies in the $[11, 6]$ star while $\vec{F}_2$ lies in the $[13, 1]$ star but

$$Q_{11,6} = Q_{13,1} = \sqrt{91}\,|\vec{q}_1| \tag{6.32}$$

which illustrates the fact that $Q_{r,s}$ does not uniquely specify $[r, s]$. Note that the circle in Figure 6.1 includes 6 red sites and 6 green sites. Thus, any resonance with the $[11, 6]$ star is also resonance with the $[13, 1]$ star and casts 12 sites into resonance to produce a resonant subspace of dimension $14 = 2 + 12$. Additional examples of this type of overlap between stars exist, including pairs with even hopping number. The smallest such example is

$$Q_{14,4} = Q_{16,2} = 7\sqrt{3}\,|\vec{q}_1| \tag{6.33}$$

a circle on which lie the 6 sites of the $[14, 4]$ star and the 12 sites of the $[16, 2]$ star. Of course, we can not resonate with the sites on this circle as their hopping number is even. Explicit example vectors $-7\vec{g}_1$ (hopping number 14) and $-8\vec{g}_1 + 3\vec{g}_2$ (hopping number 16) share this magnitude $7\sqrt{3}\,|\vec{q}_1|$.

6.3.2 Fundamental Lattice

We see now that finding a general prescription for $m_{r,s}$, the number of sites in the $[r, s]$ star, is not aligned with our present objective. Rather, we wish to find the radius of all circles, centered at the origin, which intersect exactly 3 sites in $\mathbb{B}$ which have odd hopping number. This difficult mathematical question requires a more rigorous foundation in order to answer.

We begin by partitioning the hopping lattice $\mathbb{B}$ into two disjoint sets

$$\vec{Q} \in \mathbb{B}_0 \iff \vec{Q} = n\vec{g}_1 + m\vec{g}_2 \quad \exists n, m \in \mathbb{Z} \tag{6.34}$$

$$\vec{Q} \in \mathbb{B}_1 \iff \vec{Q} = n\vec{g}_1 + m\vec{g}_2 + \vec{q}_1 \quad \exists n, m \in \mathbb{Z} \tag{6.35}$$

on which

$$\mathbb{B} = \mathbb{B}_0 \cup \mathbb{B}_1 \quad \wedge \quad \mathbb{B}_0 \cap \mathbb{B}_1 = \emptyset \tag{6.36}$$

are clearly satisfied. Observe that every site in $\mathbb{B}_0$ has even hopping number and every site in $\mathbb{B}_1$ has odd hopping number. Furthermore, both $\mathbb{B}_j$ are Bravais lattices spanned by lattice vectors $\vec{g}_1, \vec{g}_2$ (cf. Equation 2.8).

Let us define an m-*star* as a collection of m-many sites in $\mathbb{B}_1$ which lie on a circle centered at the origin which intersects exactly m sites in $\mathbb{B}$. In light of our discussion in Section 6.3.1, it is far from immediately clear that no origin-centered circle will intersect lattice sites in both $\mathbb{B}_0$ and $\mathbb{B}_1$ but we will soon prove that this is true. Assuming this fact for now, we see that our primary aim becomes to find the radius of all 3-stars.

To prove claims like the last one and more, we will extract the fundamental mathematics of $\mathbb{B}$, not subject to the physical parameters of our system. Let us define the following vectors

$$\vec{\phi}_1 \equiv \hat{q}_1/\sqrt{3} = \left(0, \tfrac{1}{\sqrt{3}}\right) \qquad \vec{\phi}_2 \equiv \hat{q}_2/\sqrt{3} = \left(-\tfrac{1}{2}, -\tfrac{1}{2\sqrt{3}}\right) \qquad \vec{\phi}_3 \equiv \hat{q}_3/\sqrt{3} = \left(\tfrac{1}{2}, -\tfrac{1}{2\sqrt{3}}\right)$$

$$\vec{\Phi}_1 \equiv \vec{\phi}_2 - \vec{\phi}_1 = \left(-\tfrac{1}{2}, -\tfrac{\sqrt{3}}{2}\right) \qquad \vec{\Phi}_2 \equiv \vec{\phi}_3 - \vec{\phi}_1 = \left(\tfrac{1}{2}, -\tfrac{\sqrt{3}}{2}\right) \tag{6.37}$$

which span a hexagonal (two point trigonal Bravais) lattice with lattice constants

$1 = \left|\vec{\Phi}_1\right| = \left|\vec{\Phi}_2\right|$ by construction. We define analogous, dimensionless lattices

$$\vec{\eta} \in \mathbb{E}_j \iff \vec{\eta} = n\vec{\Phi}_1 + m\vec{\Phi}_2 + j\vec{\phi}_1 \quad \exists n, m \in \mathbb{Z}, \forall j \in \{0, 1\} \tag{6.38}$$

$$\mathbb{E} = \mathbb{E}_0 \cup \mathbb{E}_1 \quad \wedge \quad \mathbb{E}_0 \cap \mathbb{E}_1 = \emptyset \tag{6.39}$$

spanned by the new lattice vectors.

6.3.3 Lattice Proofs

We begin by showing that, indeed, there is no origin-centered circle which intersects sites in both $\mathbb{E}_0$ and $\mathbb{E}_1$ by proving Lemma A.3.1 in Appendix A.3. We also establish a mapping of $\mathbb{E}$ into $\mathbb{N}$ by Lemma A.3.2 and a mapping of $\mathbb{E}$ into $\mathbb{E}_0$ by Lemma A.3.4 (see Appendix A.3 for proof of both).

In addition to these lemmas, we must consider the result proven in Ref. [41], regarding the number of sites which intersect circles in a trigonal Bravais lattice. That author uses the number theory of unique factorization domains and partitions the prime numbers as

Definition 6.3.1. *For all prime numbers p*

$$\begin{aligned} p \textit{ is ramified} &\iff p \equiv 0 \pmod 3 \\ p \textit{ is split} &\iff p \equiv 1 \pmod 3 \\ p \textit{ is inert} &\iff p \equiv 2 \pmod 3 \end{aligned}$$

into congruence classes modulo 3. The Fundamental Theorem of Arithmetic asserts that we may uniquely factor any $x \in \mathbb{N}$ into primes. We may partition those factors by modulo congruence and write

$$x = 3^\beta \prod_i n_i^{\nu_i} \prod_j m_j^{\mu_j} \tag{6.40}$$

for unique $\beta, \nu_k, \mu_k \in \mathbb{N}$, split primes $n_k \equiv 1 \pmod 3$ and inert primes $m_k \equiv 2 \pmod 3$. The author of Ref. [41] goes on to show that the number of lattice sites in $\mathbb{E}_0$ on a circle of radius x is

$$\mathfrak{N}\left(x^2\right) = 6 \cdot \prod_{n_i} \left(\nu_i + 1\right) \tag{6.41}$$

where the n_i, ν_i are given by Equation 6.40.[41]

Thus, we have a prescription for the radii of circles which intersect, for example, exactly 6 sites in $\mathbb{E}_0$. We use our lemmas to show that there is a one-to-one correspondence between sets of 3 sites in $\mathbb{E}_1$ which share a unique magnitude and certain sets of 6 sites in $\mathbb{E}_0$ sharing a unique magnitude in order to finally prove our main theorem.

Theorem. *There are exactly 3 distinct solutions $\vec{\lambda} \in \mathbb{E}_1$ and no solutions in $\mathbb{E}_0$ to $\left|\vec{\lambda}\right| = L$ if and only if $L = 3^{-1/2}\Pi m_j^{\mu_j} \quad \exists \mu_j \in \mathbb{N}$ and primes $m_j \equiv 2 \pmod 3$.*

This is proven as Theorem A.3.5 in Appendix A.3, and in this, we have realized an exhaustive prescription of all positive radii of origin-centered circles on which lie exactly 3 sites from $\mathbb{E}_1$ and no sites from $\mathbb{E}_0$.

Therefore, by the construction made in Equations 6.37 we know that

$$|\vec{q}_1| \prod_j m_j^{\mu_j} \quad \exists \mu_j \in \mathbb{N} \text{ and primes } m_j \equiv 2 \pmod 3$$

exhaustively prescribes the radii of all 3-stars.

6.4 Magic Energy

In the last section, we proved an exhaustive prescription for the radius of all 3-stars in $\mathbb{B}$. Moreover, the hopping lattice near commensuration θ_1 is merely scaled and rotated (cf. Equation 2.14), so, in conjunction with Equation 3.1 we now define

$$\overset{*}{V} = \hbar v_F \left|\vec{q}_1^{(\theta)}\right| \prod_j m_j^{\mu_j} \quad \exists \mu_j \in \mathbb{N} \text{ and primes } m_j \equiv 2 \pmod 3 \tag{6.42}$$

as *magic bias energies*. Note that there are infinitely many such magic bias energies, at minimum due to the infinite cardinality of $\mathbb{N}$. Any graphene bilayer with a magic bias energy has a dimension 5 resonant subspace and exhibits a zero velocity, infinite mass electron state at zero wavevector.

Presumably, the magic angles were so denoted as no justification was given for their existence, no analytic prescription obtained, and the cardinality of their set unknown.[20] Conversely, our result is not impaired by any of these factors, but we give the name magic energies to align with that phenomenon nonetheless.

The first several magic energies are

$$\overset{*}{V} \in \hbar v_F \left|\vec{q}_1^{(\theta)}\right| (1, 2, 4, 5, 8, 10, 11, 16, 17, 20, 22, 23, 25, \ldots) \tag{6.43}$$

and we note as well that these magic bias energies correspond to resonance with the

$$[1,1], [3,1], [5,2], [7,1], [11,1], [13,3], [15,1], [21,3], [23,1], [27,1], [29,4], [31,1], [33,4], \ldots$$

stars, in our two-index convention. We will describe these stars as *magic stars* and we present a larger list of the first 76 magic energies in Table 6.1. While we mathematically proved the validity of our prescription of these magic energies, we also performed a partial numerical confirmation. We generated a truncation of $\mathbb{B}$ and numerically confirmed that Equation 6.3.3 exhaustively prescribes the 3-stars within the first 5000 rings. The largest 3-star examined had radius

$$3742 \left|\vec{q}_1\right| = 2^1 \cdot 1871^1 \left|\vec{q}_1\right| = 2\left[3\left(623\right) + 2\right] \left|\vec{q}_1\right| \tag{6.44}$$

where 1871 is an inert prime.

Finally, consider solving the magic energy condition given by Equation 6.42 for the

Table 6.1: The smallest 76 magic coefficients given by products of only natural powers of inert primes $m_j \equiv 2 \pmod 3$, as in Equation 6.42. We include all such numbers up to and including $226 = 2^1 \cdot 113^1$, but infinitely many such numbers exist.

$\frac{\overset{*}{V}}{\hbar v_F \lvert \vec{q}_1 \rvert} = \prod_j m_j^{\mu_j}$	m_1	μ_1	m_2	μ_2
1	2	0		
2	2	1		
4	2	2		
5	5	1		
8	2	3		
10	2	1	5	1
11	11	1		
16	2	4		
17	17	1		
20	2	2	5	1
22	2	1	11	1
23	23	1		
25	5	2		
29	29	1		
32	2	5		
34	2	1	17	1
40	2	3	5	1
41	41	1		
44	2	2	11	1
46	2	1	23	1
47	47	1		
50	2	1	5	2
53	53	1		
55	5	1	11	1
58	2	1	29	1
59	59	1		
64	2	6		
68	2	2	17	1
71	71	1		
80	2	4	5	1
82	2	1	41	1
83	83	1		
85	5	1	17	1
88	2	3	11	1
89	89	1		
92	2	2	23	1
94	2	1	47	1
100	2	2	5	2

$\frac{\overset{*}{V}}{\hbar v_F \lvert \vec{q}_1 \rvert}$	m_1	μ_1	m_2	μ_2	m_3	μ_3
101	101	1				
106	2	1	53	1		
107	107	1				
110	2	1	5	1	11	1
113	113	1				
115	5	1	23	1		
116	2	2	29	1		
118	2	1	59	1		
121	11	2				
125	5	3				
128	2	7				
131	131	1				
136	2	3	17	1		
137	137	1				
142	2	1	71	1		
145	5	1	29	1		
149	149	1				
160	2	5	5	1		
164	2	2	41	1		
166	2	1	83	1		
167	167	1				
170	2	1	5	1	17	1
173	173	1				
176	2	4	11	1		
178	2	1	89	1		
179	179	1				
184	2	3	23	1		
187	11	1	17	1		
188	2	2	47	1		
191	191	1				
197	197	1				
200	2	3	5	2		
202	2	1	101	1		
205	5	1	41	1		
212	2	2	53	1		
214	2	1	107	1		
220	2	2	5	1	11	1
226	2	1	113	1		

deviation angle (using Equations 2.4, 2.8, 2.14), which gives

$$\overset{*}{\delta\theta} = \begin{cases} 2\arcsin\left[3\sqrt{3}a\left(8\pi\hbar v_F\right)^{-1} V \prod_j m_j^{-\mu_j}\right] & \text{if} \quad \theta = 0 \\ 2\arcsin\left[3\sqrt{3}a\left(8\pi\sqrt{7}\hbar v_F\right)^{-1} V \prod_j m_j^{-\mu_j}\right] & \text{if} \quad \theta = \theta_1 \end{cases} \tag{6.45}$$

where V is the interlayer bias energy, $3\sqrt{3}a\left(8\pi\hbar v_F\right)^{-1} = 4.46 \cdot 10^{-5}\mathrm{meV}^{-1}$, the $\mu_j \in \mathbb{N}$, and the $m_j \equiv 2 \pmod 3$ are prime. Given any finite $V > 0$, the $\arcsin$ argument takes on infinitely many values in $(0, 1]$ since there are infinitely many powers of inert primes $\prod_j m_j^{\mu_j}$ larger than any finite constant. Therefore Equation 6.45 defines an infinite number of real deviation angles $\overset{*}{\delta\theta}$.

These are not the same "magic angles" present in unbiased bilayer graphene, but we have shown that they lead to a similar phenomenon.[20] A twisted graphene bilayer in the presence of a perpendicular electric field inducing an electric potential energy difference V between the layers and rotation angle $\Theta = \theta + \overset{*}{\delta\theta}$ will possess an immutable state at zero wavevector.

6.5 Numerical Immutable State in Magic Resonance

We conclude this chapter by examining one numerical manifestation of the immutable state in magic resonance. We have shown that this immutable state emerges in the spectrum of all magic resonant systems. Recall that the chiral $\mathcal{SP}$ symmetry demands that this isolated zero-band have zero curvature at zero wavevector and the $\mathcal{C}_3$ symmetry demands the band have zero gradient there. The non-constant solution to these constraints is a so-called monkey saddle, precisely such a point in a surface which is neither a local minimum nor maximum, but has $\mathcal{C}_3$ symmetry in contrast with the $\mathcal{C}_2$ symmetry of the standard "saddle point" studied in introductory calculus.

Furthermore, it is straightforward numerically to approximate by finite differences the

derivatives for the gradient and curvature of the zero-band in the spectrum of a magic system. This has been done for several systems with various magic bias energies given by Equation 6.42 and indeed both derivatives converge to 0, even in spite of the presence of positive $\zeta > 0$. Conversely, however, systems with imperfect bias energies $(1 + \delta V)\overset{*}{V}$ (which we do not refer to as magic energies) have a zero-band with gradient which converges to 0 numerically but a curvature which does not. Indeed this result is consistent with our symmetry prediction, where we saw that nonzero bias deviations break $\mathcal{SP}$ symmetry (cf. Equation 6.11).

As shown in Section 6.4, the $[1, 1]$ star is the first magic star. Figure 6.2 displays sections of the dispersion of the real system in resonance with the $[1, 1]$ star. Specifically, we display the converged spectrum of $H^{(0)}_{7,1,1}$ ($\delta V = 0$) over sectioned domains also displayed in the figure. The sectioned domain in the left spectrum is precisely $2/3$ of the first Brillouin Zone, chosen in a way which clearly respects the $\mathcal{C}_3$ symmetry of the BZ. The domain used in the right figure is reduced in size. In the lower portions of the figure we present a low-energy subset (the $5 = w_{1,1}$ bands in the resonant subspace) of the numeric spectrum of $H^{(0)}_{7,1,1}$ taken over the sectioned domains shown above. The 5 bands are taken numerically as those with the smallest value of $\left|\varepsilon_n\left(\vec{0}\right)\right|$. Observe that, by construction of the sectioned domains, we are able to peer within the 3D dispersion and identify the qualitative nature of the real bands at $\vec{k} = \vec{0}$. Indeed, the real spectrum aligns precisely with our prediction—a pair of bands above and below zero energy and a single band (red) which is flat at the origin.

Regarding the precision of this prediction, consider Table 6.2 which illustrates the zero-wavevector numeric spectrum given by $H^{(0)}_{7,1,1}$ with the same set of parameters which appear in Figure 6.2. Also shown in the table for comparison is the numeric spectrum of $H^{(0)}_{1,1,1}$ and the low-energy analytic theory of Equation 4.19 at the same parameters. Indeed, we see nearly perfect agreement between the order 1 spectrum and the effective theory. Moreover, Hamiltonian convergence is achieved readily at this value of ζ and we see excellent

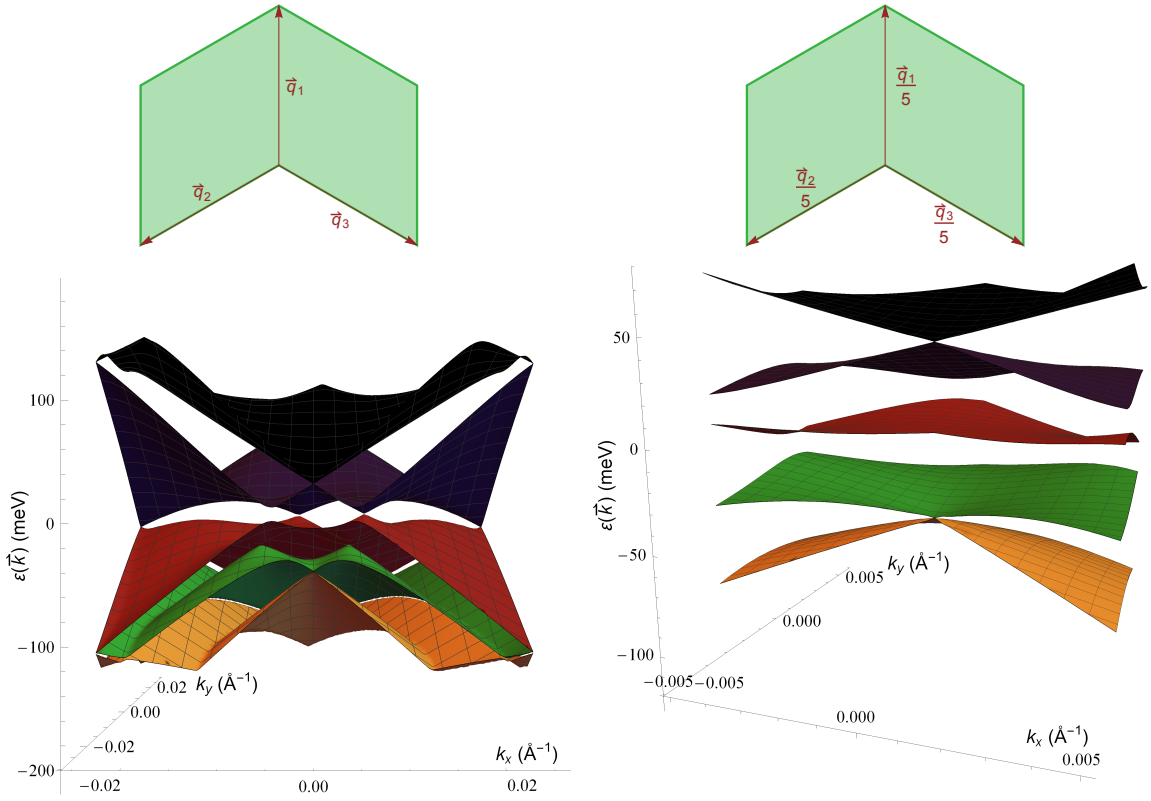

Figure 6.2: Low energy spectrum of $H^{(0)}_{7,1,1}$ over the sectioned BZ domain shown above. Only $5 = w_{1,1}$ of the $170 = 3 \times 7\,(7+1) + 2$ bands produced by $H^{(0)}_{7,1,1}$ are shown, those which have the smallest energy at $\vec{k} = \vec{0}$. The red band shown is the "zero-band" and demonstrates zero gradient and zero curvature at $\vec{k} = \vec{0}$. Parameters: $\zeta = 0.1$, $\theta = 0$, $\delta\theta = 1.02\pi/180$, $\gamma = 20\text{meV}$, $\delta V = 0$, $V = 200\text{meV}$, $a = 1.42\text{Å}$, $v_F = 10^{16}\text{Å/s}$.

Table 6.2: Spectrum of $[1,1]$ resonant subspace given by two expansion Hamiltonians and the effective theory derived in Chapter 4. Parameters: $\zeta = 0.1$, $\theta = 0$, $\delta\theta = 1.02\pi/180$, $\gamma = 20\text{meV}$, $\delta V = 0$, $V = 200\text{meV}$, $a = 1.42\text{Å}$, $v_F = 10^{16}\text{Å/s}$.

Five-band Zero-Wavelength Low Energy Spectrum (meV)		
$H^{(0)}_{1,1,1}\|_{\vec{k}=\vec{0}}$	$H^{(0)}_{7,1,1}\|_{\vec{k}=\vec{0}}$	Theoretical Prediction of Equation 4.19
-47.70	-48.26	$-47.52 \approx \left(3\sqrt{3} - 6 - \sqrt{19263 + 9564\sqrt{3}}\right)/4$
-47.70	-48.26	$-47.52 \approx \left(3\sqrt{3} - 6 - \sqrt{19263 + 9564\sqrt{3}}\right)/4$
0.00	-1.48	0
47.34	46.42	$47.12 \approx \left(3\sqrt{3} - 6 + \sqrt{19263 + 9564\sqrt{3}}\right)/4$
47.34	46.42	$47.12 \approx \left(3\sqrt{3} - 6 + \sqrt{19263 + 9564\sqrt{3}}\right)/4$

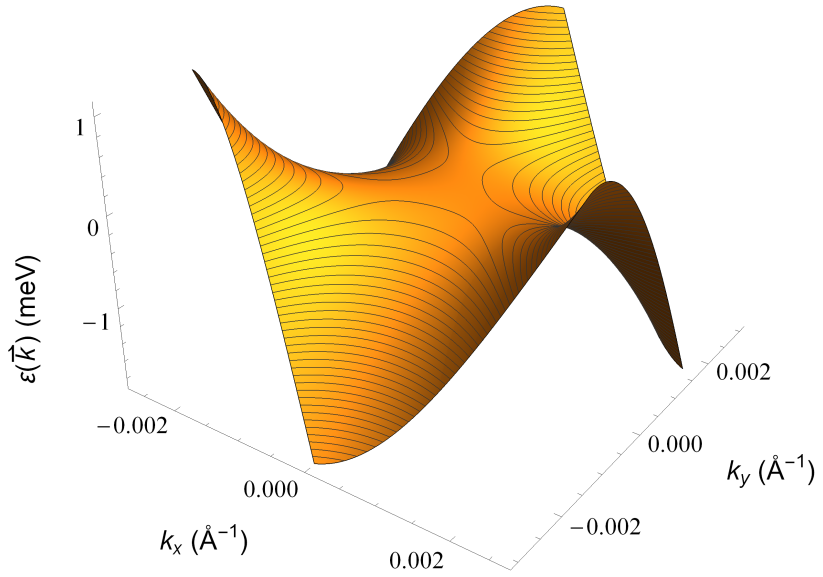

Figure 6.3: The zero-band of $H^{(0)}_{1,1,1}$ viewed as surface embedded in 3D (wavevector-energy) space over a domain hexagon with corners $\pm\vec{q}^{\,(0)}_j/10$ in the center of the superlattice Brillouin zone. The meshlines are level sets of energy and we witness the monkey saddle at $\vec{k} = \vec{0}$ predicted by the $\mathcal{C}_3$ and $\mathcal{SP}$ symmetries of the weak effective theory. The zero gradient and zero curvature of the surface at the origin is evident. Parameters: $\zeta = 0.1$, $\theta = 0$, $\delta\theta = 1.02\pi/180$, $\gamma = 20\text{meV}$, $\delta V = 0$, $V = 200\text{meV}$, $a = 1.42\text{Å}$, $v_F = 10^{16}\text{Å/s}$.

agreement between our prediction and the higher order spectrum as well.

Lastly, we extract the zero-band from Figure 6.2 and display it again in Figures 6.3 and 6.4 with the same parameters. In the former, we plot over a small hexagonal domain in the center of the Brillouin zone, with corners at $\pm\vec{q}^{\,(0)}_j/10$. This figure gives the clearest representation of the monkey saddle, the point of zero gradient and zero curvature at $\vec{k} = \vec{0}$ which also respects $\mathcal{C}_3$ symmetry. In the limit of satisfactorily small ζ, the immutable state appears in all magic systems in this way. Furthermore, we plot the same zero-band over the entire BZ in Figure 6.4. Specifically, the band is shown first as a 3D plot from another viewing angle with mesh lines given again by energy level sets. Below, the same band is displayed as a 2D contour plot in the energy. Both depictions further illustrate the zero gradient and zero curvature point at zero wavevector we proved previously and confirmed by numerical computation.

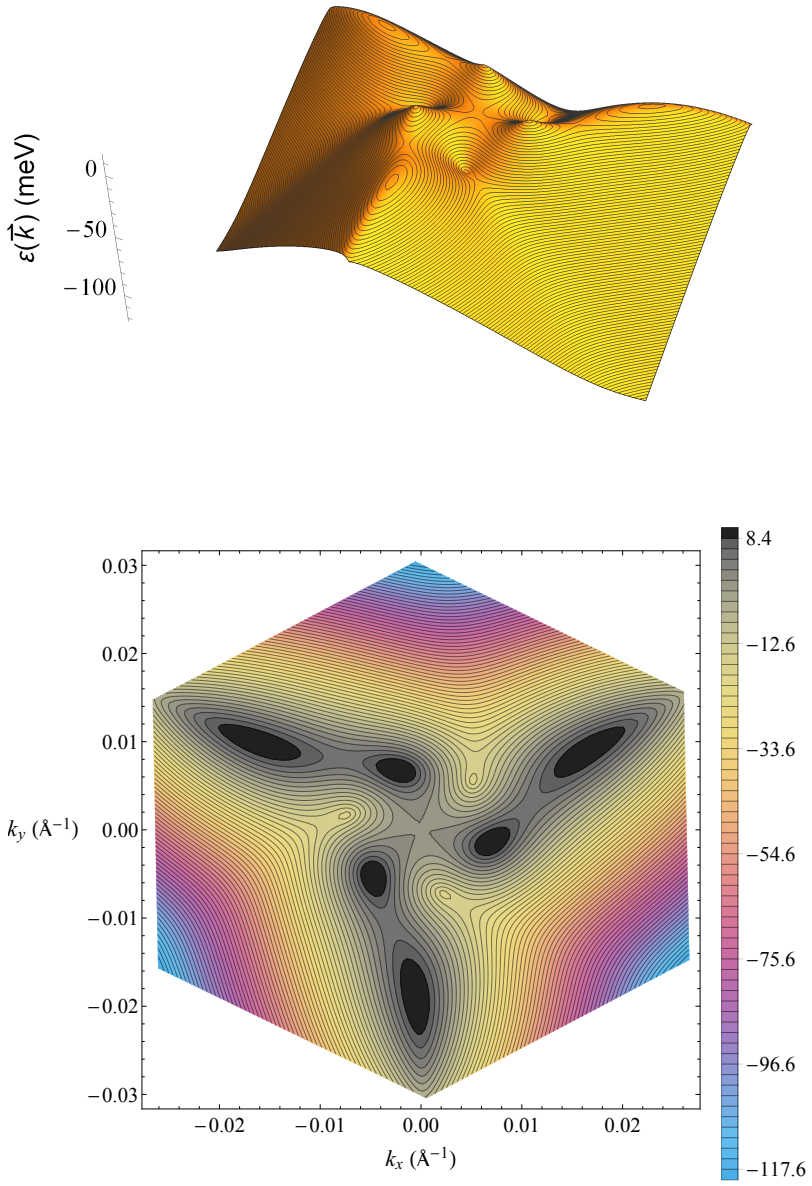

Figure 6.4: The zero-band of $H^{(0)}_{7,1,1}$ viewed as surface embedded in 3D (wavevector-energy) space and as a contour map. The domain is the full superlattice Brillouin zone, the mesh-lines of the upper figure are level sets of energy, and the energy values in the contour legend in the lower figure are in meV. Parameters: $\zeta = 0.1$, $\theta = 0$, $\delta\theta = 1.02\pi/180$, $\gamma = 20\text{meV}$, $\delta V = 0$, $V = 200\text{meV}$, $a = 1.42\text{Å}$, $v_F = 10^{16}\text{Å/s}$.

CHAPTER 7
CONCLUSION

We conclude this dissertation with a brief recapitulation of the consequence of the work presented here. We began in Chapter 2 by specifying the mathematical framework of twisted graphene bilayers. We formalized the hopping lattice, $\mathbb{B}$, which enumerates and collects all transmission of Dirac momenta along all interlayer tunneling and intralayer scattering sequences. We followed Bistritzer and MacDonald [20] and provided an algorithm to create finite matrix Hamiltonians for the dispersion of electrons in the superlattice Brillouin zone. We generalized this approach to include arbitrary interlayer twist angles and an interlayer bias energy using a theory of general commensuration.[24]

7.1 Resonance

In Chapter 3 we introduced resonance, the theoretical foundation for all of the results in this body. We created a natural number of bias energies, proportional to the external electric field strength, which resonate with the inherent kinetic energy difference between twisted graphene layers. We considered the numerical convergence of our Hamiltonian expansion and showed that resonance introduces strictly nonperturbative physics. Additionally, we considered physical limitations for the parameters in our model which allow us to greatly reduce the dimension of the parameter space. Lastly, we introduced a system of topological words to describe the evolution of the Fermi surface and formalized the topological phase transition which forms the basis of experimentally relevant singularies in behavior known as Lifshitz transitions.

7.2 Effective Theory

While the effects of resonance are embedded within our general expansion Hamiltonians, in Chapter 4 we used Schrieffer-Wolff transformations to extract the fundamental nature of resonant systems. By combining the Schrieffer-Wolff transformation and careful gauge transformations, effective theories for resonance with the first star were obtained. Among the insights unveiled by the effective theories is that, in a suitable regime, the physics depend little on the commensuration angle. This allows us to conceptually connect myriad disparate bilayer graphene systems with wildly different interlayer twist angles. Moreover, the effective theory illustrated the inherent complexity of graphene bilayers in resonance compared to unbiased bilayers, while simultaneously revealing an important simplicity in scale invariance in the limit of weak effective coupling. Finally, we demonstrated the existence of analytic closed-form solutions to our effective theories outside algebraic functions. In this, we found an exactly solvable limit of nonperturbative physics in twisted bilayer graphene.

7.3 Universal Lifshitz Transitions

Chapter 5 demonstrated some results of our theories in the dispersion spectra of resonant graphene bilayers. We numerically verified predictions of our effective theories in suitable systems, exploiting scale invariance and commensuration dependence to discover a universal regime in $[1, 1]$ resonance. We conjecture with good numerical support that this regime possesses the universal topological word $\mathcal{TRVRT}$ and produces 4 Lifshitz transitions not seen in any other known graphene bilayer systems. We showed that this result appears robust to a wide range of parameter perturbations and demonstrated a viable regime for experimental verification. In general, we found that an apparent boundless number of new topological phase transitions can be induced in bilayer graphene via bias resonance.

7.4 Magic Resonance

In Chapter 6, we used mathematical proof to justify an exhaustive prescription for an infinite number of magic bias energies at which the system resonates with exactly 3 sites in the lattice. We showed that, in every case, a dimension 5 resonant subspace is induced which necessarily possesses exactly 1 zero energy band at zero wavevector. Since our effective theory revealed the isolation of this band, we were able to use symmetries of the graphene lattice and of the effective Hamiltonian to show that this band must have zero gradient and zero curvature at the origin. This led to the existence of an immutable state, a stationary state with infinite inertia. In addition to highlighting this structure in the numerical band, we mentioned the connection between this result and the small magic twist angles predicted in unbiased bilayers.[20] In fact, we recast our magic energy condition in terms of the interlayer angle to find an analytic expression for an infinite set of real angles, associated with any bias energy $V > 0$, for which the immutable state must exist at zero Dirac wavevector.

The original magic angles in unbiased twisted graphene bilayers were found numerically by our predecessor without an exact prescription and without knowledge of their total number. Conversely, we find an exact prescription of infinitely many bias energies for any interlayer angle, or, an exact prescription of infinitely many angles for any positive bias energy. In either case, we find a zero velocity, zero curvature, immutable state at zero Dirac wavevector.

Appendices

APPENDIX A

MATHEMATICS APPENDIX

The primary goal of this chapter is to give formal mathematical proof of statements made in the body of this dissertation. It is important to note that, in order to facilitate clarity, many variables defined globally in this dissertation will be used in this appendix without further explicit definition. To recall those definitions, see the Symbol Index.

A.1 Linear Algebra

Theorem A.1.1. *Given square, complex matrix Y whose dimension is at least 4 and whose elements satisfy $Y_{i,j} = 0 \iff (i \in \{1,2\} \vee j \geq 3)$, dim $\left[Col\left(Y + Y^\dagger\right)\right] = 4$ if and only if the first two columns of Y are linearly independent.*

Proof. Let $n \geq 4$ be a natural number.

Let[1] $Y \in \mathbb{C}^n \times \mathbb{C}^n$ such that $Y_{i,j} = 0 \iff (i \in \{1,2\} \vee j \geq 3)$.

Let $\vec{\eta} \in \mathbb{C}^n$ be arbitrary.

Consider

$$\begin{aligned}\left(Y + Y^\dagger\right)\vec{\eta} &= Y\vec{\eta} + Y^\dagger\vec{\eta} \quad \text{(linearity)} \\ &= \begin{pmatrix} \sum_{k=1}^{n} Y_{1,k}\eta_k \\ \sum_{k=1}^{n} Y_{2,k}\eta_k \\ \sum_{k=1}^{n} Y_{3,k}\eta_k \\ \vdots \\ \sum_{k=1}^{n} Y_{n,k}\eta_k \end{pmatrix} + \begin{pmatrix} \sum_{k=1}^{n} Y^*_{k,1}\eta_k \\ \sum_{k=1}^{n} Y^*_{k,2}\eta_k \\ \sum_{k=1}^{n} Y^*_{k,3}\eta_k \\ \vdots \\ \sum_{k=1}^{n} Y_{k,n}\eta_k \end{pmatrix}\end{aligned}$$

[1] complex numbers $\mathbb{C}$

$$\left(Y+Y^{\dagger}\right)\vec{\eta}=\begin{pmatrix}0\\0\\\sum_{k=1}^{n}Y_{3,k}\eta_k\\\vdots\\\sum_{k=1}^{n}Y_{n,k}\eta_k\end{pmatrix}+\begin{pmatrix}\sum_{k=3}^{n}Y^*_{k,1}\eta_k\\\sum_{k=3}^{n}Y^*_{k,2}\eta_k\\\sum_{k=3}^{n}Y^*_{k,3}\eta_k\\\vdots\\\sum_{k=3}^{n}Y_{k,n}\eta_k\end{pmatrix}\quad\text{(since } Y_{1,k}=Y_{2,k}=0=Y^*_{1,k}=Y^*_{2,k})$$

$$=\begin{pmatrix}0\\0\\\sum_{k=1}^{2}Y_{3,k}\eta_k\\\vdots\\\sum_{k=1}^{2}Y_{n,k}\eta_k\end{pmatrix}+\begin{pmatrix}\sum_{k=3}^{n}Y^*_{k,1}\eta_k\\\sum_{k=3}^{n}Y^*_{k,2}\eta_k\\0\\\vdots\\0\end{pmatrix}\quad\text{(since } Y_{i,k}=0\iff k\geq 3)$$

$$=\eta_1\begin{pmatrix}0\\0\\Y_{3,1}\\\vdots\\Y_{n,1}\end{pmatrix}+\eta_2\begin{pmatrix}0\\0\\Y_{3,2}\\\vdots\\Y_{n,2}\end{pmatrix}+\sum_{k=3}^{n}Y^*_{k,1}\eta_k\begin{pmatrix}1\\0\\0\\\vdots\\0\end{pmatrix}+\sum_{k=3}^{n}Y^*_{k,2}\eta_k\begin{pmatrix}0\\1\\0\\\vdots\\0\end{pmatrix}$$

$$\in\text{Span}\left\{\begin{pmatrix}0\\0\\Y_{3,1}\\\vdots\\Y_{n,1}\end{pmatrix},\begin{pmatrix}0\\0\\Y_{3,2}\\\vdots\\Y_{n,2}\end{pmatrix},\begin{pmatrix}1\\0\\0\\\vdots\\0\end{pmatrix},\begin{pmatrix}0\\1\\0\\\vdots\\0\end{pmatrix}\right\}=\text{Col}\left(Y+Y^{\dagger}\right)$$

The final equality follows from the definition of the column space. It is evident that these 4 vectors are all linearly independent except possibly the first pair. Moreover, we observe that the first two of these vectors are precisely the first and second column of Y since $Y_{1,1}=Y_{2,1}=Y_{1,2}=Y_{2,2}=0$. Therefore, $\dim\left[\text{Col}\left(Y+Y^{\dagger}\right)\right]=4$ if and only if the first two columns of Y are linearly independent. $\square$

A.2 Metric Spaces

Definition A.2.1 (Lattice metric)**.** *Given* $\vec{u} = u_1\vec{g}_1 + u_2\vec{g}_2 + u_3\vec{q}_1, \vec{v} = v_1\vec{g}_1 + v_2\vec{g}_2 + v_3\vec{q}_1$

$\exists u_1, u_2, v_1, v_2 \in \mathbb{Z}, u_3, v_3 \in \{0, 1\}$

Let $\langle \vec{u}, \vec{v} \rangle_L = |v_1 - u_1| + |v_2 - u_2| + |\,(v_1 + v_2 - v_3) - (u_1 + u_2 - u_3)\,|$

define the lattice metric between $\vec{u}$ *and* $\vec{v}$*.*

Theorem A.2.2. $\langle \cdot, \cdot \rangle_L$ *is a metric in* $\mathbb{B}$*.*

Proof. Let $\vec{u}, \vec{v}, \vec{w} \in \mathbb{B}$. Then $\exists u_1, u_2, v_1, v_2, w_1, w_2 \in \mathbb{Z}, u_3, v_3, w_3 \in \{0, 1\}$ such that $\vec{u} = u_1\vec{g}_1 + u_2\vec{g}_2 + u_3\vec{q}_1, \vec{v} = v_1\vec{g}_1 + v_2\vec{g}_2 + v_3\vec{q}_1, \vec{w} = w_1\vec{g}_1 + w_2\vec{g}_2 + w_3\vec{q}_1$

Consider

$$\begin{aligned}
\langle \vec{u}, \vec{v} \rangle_L &= |v_1 - u_1| + |v_2 - u_2| + |\,(v_1 + v_2 - v_3) - (u_1 + u_2 - u_3)\,| && \text{(definition A.2.1)} \\
&= |n_1| + |n_2| + |n_3| \quad \exists n_1, n_2, n_3 \in \mathbb{Z} && \text{(closure of } \mathbb{Z} \text{ under } +) \\
&\geq 0
\end{aligned}$$

Further

$$\begin{aligned}
0 &= \langle \vec{u}, \vec{v} \rangle_L \\
&= |v_1 - u_1| + |v_2 - u_2| + |\,(v_1 + v_2 - v_3) - (u_1 + u_2 - u_3)\,| && \text{(definition A.2.1)} \\
&\iff 0 = |v_1 - u_1| = |v_2 - u_2| = |\,(v_1 + v_2 - v_3) - (u_1 + u_2 - u_3)\,| \\
&\iff 0 = v_1 - u_1 = v_2 - u_2 = (v_1 + v_2 - v_3) - (u_1 + u_2 - u_3) \\
&\iff u_1 = v_1 \ \wedge \ u_2 = v_2 \ \wedge \ (u_1 + u_2 - u_3) = (v_1 + v_2 - v_3) \\
&\iff u_1 = v_1 \ \wedge \ u_2 = v_2 \ \wedge \ u_3 = v_3 \\
&\iff \vec{u} = \vec{v}
\end{aligned}$$

Moreover

$$\begin{aligned}
\langle \vec{u}, \vec{v} \rangle_L &= |v_1 - u_1| + |v_2 - u_2| + |\,(v_1 + v_2 - v_3) - (u_1 + u_2 - u_3)\,| \qquad \text{(definition A.2.1)} \\
&= |\,-(u_1 - v_1)\,| + |\,-(u_2 - v_2)\,| + |\,-[(u_1 + u_2 - u_3) - (v_1 + v_2 - v_3)]\,| \\
&= |u_1 - v_1| + |u_2 - v_2| + |\,(u_1 + u_2 - u_3) - (v_1 + v_2 - v_3)\,| \\
&= \langle \vec{v}, \vec{u} \rangle_L \qquad \text{(definition A.2.1)}
\end{aligned}$$

Finally, consider

$$\begin{aligned}
\langle \vec{u}, \vec{v} \rangle_L + \langle \vec{v}, \vec{w} \rangle_L &= |v_1 - u_1| + |v_2 - u_2| + |\,(v_1 + v_2 - v_3) - (u_1 + u_2 - u_3)\,| \quad \text{(df. A.2.1)} \\
&\qquad + |w_1 - v_1| + |w_2 - v_2| + |\,(w_1 + w_2 - w_3) - (v_1 + v_2 - v_3)\,| \\
&= (|w_1 - v_1| + |v_1 - u_1|) + (|w_2 - v_2| + |v_2 - u_2|) \\
&\qquad + (|\,(w_1 + w_2 - w_3) - (v_1 + v_2 - v_3)\,| + |\,(v_1 + v_2 - v_3) - (u_1 + u_2 - u_3)\,|) \\
&\geq |\,(w_1 - v_1) + (v_1 - u_1)\,| + |\,(w_2 - v_2) + (v_2 - u_2)\,| \quad \text{(triangle inequality on } \mathbb{C}) \\
&\qquad + |[(w_1 + w_2 - w_3) - (v_1 + v_2 - v_3)] + [(v_1 + v_2 - v_3) - (u_1 + u_2 - u_3)]| \\
&= |w_1 - u_1| + |w_2 - u_2| + |\,(w_1 + w_2 - w_3) - (u_1 + u_2 - u_3)\,| \\
&= \langle \vec{u}, \vec{w} \rangle_L \quad \text{(definition A.2.1)}
\end{aligned}$$

Therefore, $\langle \cdot, \cdot \rangle_L$ is a metric in $\mathbb{B}$. □

Corollary A.2.3. *$\langle \cdot, \cdot \rangle_L$ is a translation invariant metric in $\mathbb{B}$.*

Proof. Let $\vec{u}, \vec{v}, \vec{w} \in \mathbb{B}$. Then $\exists u_1, u_2, v_1, v_2, w_1, w_2 \in \mathbb{Z}, u_3, v3, w_3 \in \{0, 1\}$ such that $\vec{u} = u_1\vec{g}_1 + u_2\vec{g}_2 + u_3\vec{q}_1, \vec{v} = v_1\vec{g}_1 + v_2\vec{g}_2 + v_3\vec{q}_1, \vec{w} = w_1\vec{g}_1 + w_2\vec{g}_2 + w_3\vec{q}_1$

Consider

$$\begin{aligned}
\langle \vec{u}+\vec{w}, \vec{v}+\vec{w} \rangle_L &= \langle (u_1+w_1)\,\vec{g}_1 + (u_2+w_2)\,\vec{g}_2 + (u_3+w_3)\,\vec{q}_1, \\
&\qquad\qquad (v_1+w_1)\,\vec{g}_1 + (v_2+w_2)\,\vec{g}_2 + (v_3+w_3)\,\vec{q}_1 \rangle_L \\
&= |\,(v_1+w_1)-(u_1+w_1)\,| + |\,(v_2+w_2)-(u_2+w_2)\,| \quad \text{(definition A.2.1)} \\
&\quad + |\,[(v_1+w_1)+(v_2+w_2)-(v_3+w_3)]-[(u_1+w_1)+(u_2+w_2)-(u_3+w_3)]\,| \\
&= |v_1-u_1| + |v_2-u_2| + |\,(v_1+v_2-v_3)-(u_1+u_2-u_3)\,| \\
&= \langle \vec{u}, \vec{v} \rangle_L \quad \text{(definition A.2.1)}
\end{aligned}$$

So $\langle \cdot, \cdot \rangle_L$ is a translation invariant metric in $\mathbb{B}$. □

A.3 Number Theory

Recall the basis vectors of $\mathbb{E}$ defined in section 6.3.2 by Equation 6.37

$$\vec{\phi}_1 \equiv \left(0, \tfrac{1}{\sqrt{3}}\right) \qquad \vec{\phi}_2 \equiv \left(-\tfrac{1}{2}, -\tfrac{1}{2\sqrt{3}}\right) \qquad \vec{\phi}_3 \equiv \left(\tfrac{1}{2}, -\tfrac{1}{2\sqrt{3}}\right)$$

$$\vec{\Phi}_1 \equiv \vec{\phi}_2 - \vec{\phi}_1 = \left(-\tfrac{1}{2}, -\tfrac{\sqrt{3}}{2}\right) \qquad \vec{\Phi}_2 \equiv \vec{\phi}_3 - \vec{\phi}_1 = \left(\tfrac{1}{2}, -\tfrac{\sqrt{3}}{2}\right) \tag{A.1}$$

so we have

$$\begin{aligned}
\vec{\phi}_1 = 3^{-1}\left(3\vec{\phi}_1\right) &= 3^{-1}\left[\left(\vec{\phi}_1+\vec{\phi}_2+\vec{\phi}_3\right) - \left(\vec{\phi}_2-\vec{\phi}_1\right) - \left(\vec{\phi}_3-\vec{\phi}_1\right)\right] \\
&= 3^{-1}\left(\vec{0} - \vec{\Phi}_1 - \vec{\Phi}_2\right) \\
&= -\left(\vec{\Phi}_1+\vec{\Phi}_2\right)/3
\end{aligned} \tag{A.2}$$

and for all $n_j, m_j \in \mathbb{Z}, j \in \{0,1\}$ we have the following.

$$
\begin{aligned}
3\left|n_j\vec{\Phi}_1 + m_j\vec{\Phi}_2 + j\vec{\phi}_1\right|^2 &= 3\left(n_j\vec{\Phi}_1 + m_j\vec{\Phi}_2 + j\vec{\phi}_1\right)\cdot\left(n_j\vec{\Phi}_1 + m_j\vec{\Phi}_2 + j\vec{\phi}_1\right) \\
&= 3\left(n_j^2\left|\vec{\Phi}_1\right|^2 + m_j^2\left|\vec{\Phi}_2\right|^2 + j^2\left|\vec{\phi}_1\right|^2 + 2n_jm_j\vec{\Phi}_1\cdot\vec{\Phi}_2 + 2jn_j\vec{\Phi}_1\cdot\vec{\phi}_1 + 2jm_j\vec{\Phi}_2\cdot\vec{\phi}_1\right) \\
&= 3\left\{n_j^2\left|\vec{\Phi}_1\right|^2 + m_j^2\left|\vec{\Phi}_2\right|^2 + j^2\left|\vec{\phi}_1\right|^2 + 2n_jm_j\vec{\Phi}_1\cdot\vec{\Phi}_2 + 2j\left[n_j\vec{\Phi}_1\cdot\vec{\phi}_1 + m_j\vec{\Phi}_2\cdot\vec{\phi}_1\right]\right\} \\
&= 3\left\{n_j^2\,(1) + m_j^2\,(1) + j^2\,(1/3) + 2n_jm_j\,(1/2) + 2j\left[n_j\,(-1/2) + m_j\,(-1/2)\right]\right\} \\
&= 3\left[n_j^2 + m_j^2 + 3^{-1}j + n_jm_j - j\,(n_j + m_j)\right] \qquad \text{(since } j \in \{0,1\}\text{)} \\
&= 3\left[n_j^2 + m_j^2 + n_jm_j - j\,(n_j + m_j)\right] + j \qquad \text{(A.3)} \\
&\equiv j \pmod 3 \qquad \text{(A.4)}
\end{aligned}
$$

Lemma A.3.1. *There exists no $\vec{\eta}_0 \in \mathbb{E}_0$ and $\vec{\eta}_1 \in \mathbb{E}_1$ such that $|\vec{\eta}_0| = |\vec{\eta}_1|$.*

Proof. Let $\vec{\eta}_0 \in \mathbb{E}_0$ and $\vec{\eta}_1 \in \mathbb{E}_1$. Then $\vec{\eta}_j = n_j\vec{\Phi}_1 + m_j\vec{\Phi}_2 + j\vec{\phi}_1 \quad \exists n_j, m_j \in \mathbb{Z}, \forall j \in \{0,1\}$.
Then $3\left|\vec{\eta}_0\right|^2 \neq 3\left|\vec{\eta}_1\right|^2$ by Equation A.4. Thus, $|\vec{\eta}_0| \neq |\vec{\eta}_1|$. □

Lemma A.3.2. *For every $\vec{\eta} \in \mathbb{E}$, $3\left|\vec{\eta}\right|^2 \in \mathbb{N}$.*

Proof. Let $\vec{\eta} \in \mathbb{E}$. Then $\vec{\eta} = n\vec{\Phi}_1 + m\vec{\Phi}_2 + j\vec{\phi}_1 \quad \exists n, m \in \mathbb{Z}, \exists j \in \{0,1\}$.
Then $3\left|\vec{\eta}\right|^2 = 3\left[n^2 + m^2 + nm - j\,(n+m)\right] + j \in \mathbb{Z}$ by equation A.3.
Since $\vec{\eta} \in \mathbb{E} \subset \mathbb{R}^2$, $|\vec{\eta}| \geq 0$ implies that $3\left|\vec{\eta}\right|^2 \in \mathbb{N}$. □

Lemma A.3.3. *For every $\vec{\eta}_1 \in \mathbb{E}_1$, $3\left|\vec{\eta}_1\right|^2 \equiv 1 \pmod 3$. For every $\vec{\eta}_0 \in \mathbb{E}_0$, $3\left|\vec{\eta}_0\right|^2 \equiv 0 \pmod 3$ and $\vec{\eta}_0 \cdot \hat{x} = 0 \implies \sqrt{3}\,|\vec{\eta}_0| \in \mathbb{N} \wedge \sqrt{3}\,|\vec{\eta}_0| \equiv 0 \pmod 3$.*

Proof. Let $\vec{\eta}_0 \in \mathbb{E}_0$ and $\vec{\eta}_1 \in \mathbb{E}_1$. Then $\vec{\eta}_j = n_j\vec{\Phi}_1 + m_j\vec{\Phi}_2 + j\vec{\phi}_1 \quad \exists n_j, m_j \in \mathbb{Z}, \forall j \in \{0,1\}$.
$3\left|\vec{\eta}_1\right|^2 \equiv 1 \pmod 3$ and $3\left|\vec{\eta}_0\right|^2 \equiv 0 \pmod 3$ follow from Equation A.4. Separately, since

$$
\begin{aligned}
0 = \vec{\eta}_0 \cdot \hat{x} &= \left(n_0\vec{\Phi}_1 + m_0\vec{\Phi}_2\right)\cdot\hat{x} = n_0\left(\vec{\Phi}_1\cdot\hat{x}\right) + m_0\left(\vec{\Phi}_2\cdot\hat{x}\right) \\
&= n_0\,(-1/2) + m_0\,(1/2) = -1/2\,(n_0 - m_0) \iff n_0 = m_0
\end{aligned}
$$

$0 = \vec{\eta}_0 \cdot \hat{x} \implies 3\left|\vec{\eta}_0\right|^2 = 3\left(n_0^2 + n_0^2 + n_0 n_0\right)$ by Equation A.3. Thus $\left|\vec{\eta}_0\right|^2 = 3n_0^2$, so $\left|\vec{\eta}_0\right| = \sqrt{3}\left|n_0\right|$ and $\sqrt{3}\left|\vec{\eta}_0\right| = 3\left|n_0\right|$. Thus $\sqrt{3}\left|\vec{\eta}_0\right| \in \mathbb{N}$ and $\sqrt{3}\left|\vec{\eta}_0\right| \equiv 0 \pmod 3$. □

Lemma A.3.4. *For every $\vec{\eta} \in \mathbb{E}$ and $p \in \mathbb{Z}$, $3p\vec{\eta} \in \mathbb{E}_0$.*

Proof. Let $p \in \mathbb{Z}$ and $\vec{\eta} \in \mathbb{E}$. Then $\vec{\eta} = n\vec{\Phi}_1 + m\vec{\Phi}_2 + j\vec{\phi}_1 \quad \exists n, m \in \mathbb{Z}, \exists j \in \{0, 1\}$.

$$\begin{aligned} 3p\vec{\eta} = 3p\left(n\vec{\Phi}_1 + m\vec{\Phi}_2 + t\vec{\phi}_1\right) &= p\left[3n\vec{\Phi}_1 + 3m\vec{\Phi}_2 + t\left(3\vec{\phi}_1\right)\right] \\ &= p\left[3n\vec{\Phi}_1 + 3m\vec{\Phi}_2 - t\left(\vec{\Phi}_1 + \vec{\Phi}_2\right)\right] \quad \text{(Eq. A.2)} \\ &= \left[p\left(3n - t\right)\right]\vec{\Phi}_1 + \left[p\left(3m - t\right)\right]\vec{\Phi}_2 \end{aligned}$$

Thus $3p\vec{\eta} \in \mathbb{E}_0$. □

Theorem A.3.5. *There are exactly 3 distinct solutions $\vec{\lambda} \in \mathbb{E}_1$ and no solutions in $\mathbb{E}_0$ to $\left|\vec{\lambda}\right| = L$ if and only if $L = 3^{-1/2}\Pi m_j^{\mu_j} \quad \exists \mu_j \in \mathbb{N}$ and primes $m_j \equiv 2 \pmod 3$.*

Proof. Let $L > 0$ and assume there are exactly 3 vectors $\vec{\lambda}_j \in \mathbb{E}_1$ such that $\left|\vec{\lambda}_j\right| = L$. Lemma A.3.1 ensures no vector from $\mathbb{E}_0$ shares this length. Define three vectors $\vec{\Lambda}_j \equiv 3\vec{\lambda}_j$. Lemma A.3.4 ensures that $\vec{\Lambda}_j \in \mathbb{E}_0$ and furthermore that $-\vec{\Lambda}_j \in \mathbb{E}_0$. Thus, we have at least 6 distinct solutions to $\left|\vec{\Lambda}\right| = 3L$ in $\mathbb{E}_0$.

We may write an arbitrary solution in $\mathbb{E}_0$ to $\left|\vec{\Lambda}'\right| = 3L$ as $\vec{\Lambda}' = l\vec{\Phi}_1 + (l+d)\vec{\Phi}_2$ for some $l, d \in \mathbb{Z}$. Then

$$\begin{aligned} 3\left|\vec{\lambda}_j\right|^2 = (3L)^2/3 = \left|\vec{\Lambda}'\right|^2/3 &= \left(l^2\left|\vec{\Phi}_1\right|^2 + (l+d)^2\left|\vec{\Phi}_2\right|^2 + 2l(l+d)\vec{\Phi}_1 \cdot \vec{\Phi}_2\right)/3 \\ &= \left(l^2 + (l+d)^2 + 2l(l+d)/2\right)/3 \\ &= l^2 + ld + d^2/3 \end{aligned}$$

which must be a natural number by Lemma A.3.2. Therefore $d = 3r$ for some integer r and $3\left|\vec{\lambda}_j\right|^2 = l^2 + 3lr + 3r^2$. Furthermore, Lemma A.3.3 demands that $3\left|\vec{\lambda}_j\right|^2 \equiv 1 \pmod 3$,

so we must conclude that $l \neq 0 \pmod 3$. Thus $l = 3s - t$ for some integer s and some $t \in \{-1, 1\}$. Since

$$\begin{aligned}\vec{\Lambda}'/3 = \left[l\vec{\Phi}_1 + (l+d)\,\vec{\Phi}_2\right]/3 &= \left[(3s-t)\left(\vec{\Phi}_1 + \vec{\Phi}_2\right) + 3r\vec{\Phi}_2\right]/3 \\ &= \left[3s\left(\vec{\Phi}_1 + \vec{\Phi}_2\right) + 3t\vec{\phi}_1 + 3r\vec{\Phi}_2\right]/3 \quad \text{(Eq. A.2)} \\ &= s\vec{\Phi}_1 + (s+r)\,\vec{\Phi}_2 + t\vec{\phi}_1\end{aligned}$$

we conclude that either $\vec{\Lambda}'/3 \in \mathbb{E}_1$ (if $t = 1$), or $-\vec{\Lambda}'/3 \in \mathbb{E}_1$ (if $t = -1$). Therefore, indeed all vectors $\vec{\Lambda} \in \mathbb{E}_0$ with length $3L$ correspond to $\pm 3\vec{\lambda}$ for some $\vec{\lambda} \in \mathbb{E}_1$. Since we assumed exactly 3 vectors $\vec{\lambda}_j \in \mathbb{E}_1$ exist such that $\left|\vec{\lambda}_j\right| = L$, there must be exactly 6 solutions to $\left|\vec{\Lambda}_j\right| = 3L$ in $\mathbb{E}_0$.

An exact expression for the radii of all such sets of 6 vectors of one length in $\mathbb{E}_0$ is derived in Ref. [41]. It requires prime factorization of those radii and partitioning of their prime factors into equivalence classes modulo 3. We write natural number (by Lemma A.3.2)

$$3\left(3\left|\vec{\lambda}_j\right|^2\right) = (3L)^2 = \left|\vec{\Lambda}_j\right|^2 = 3^\beta \prod_i n_i^{\nu_i} \prod_p m_p^{\upsilon_p} \tag{A.5}$$

for unique $\beta, \nu_k, \upsilon_k \in \mathbb{N}$ and primes $n_k \equiv 1 \pmod 3$ and $m_k \equiv 2 \pmod 3$ for all k. Lemma A.3.3 demands that $3\left|\vec{\lambda}_j\right|^2 \equiv 1 \pmod 3$, so $\beta = 1$. Furthermore, it is shown in Ref. [41] that all $\upsilon_j \equiv 2\mu_j$ are even numbers.

According to Eq. (7) of Ref. [41] the number of lattice sites in $\mathbb{E}_0$ on a circle of radius $\left|\vec{\Lambda}_j\right|$ is

$$\mathfrak{N}\left[\left|\vec{\Lambda}_j\right|^2\right] = 6 \cdot \prod_{n_i} (\nu_i + 1) \tag{A.6}$$

where the n_i, ν_i are given by Equation A.5. Immediately we see that $\mathfrak{N}\left[\left|\vec{\Lambda}_j\right|^2\right] = 6$

requires all the ν_i to be zero. Thus, indeed,

$$L = 3^{-1}\sqrt{(3L)^2} = 3^{-1}\sqrt{3^1 \prod_i n_i^0 \prod_j m_j^{2\mu_j}} = 3^{-1/2} \prod_j m_j^{\mu_j} \tag{A.7}$$

with $\mu_j \in \mathbb{N}$ and primes $m_j \equiv 2 \pmod 3$, as claimed.

The reverse implication remains to be shown, that every set of exactly 6 solutions to $\left|\vec{\Lambda}_j\right| = 3L$ with L given by Equation A.7 implies exactly 3 solutions to $\left|\vec{\lambda}_j\right| = L$ in $\mathbb{E}_1$. Ref. [41] shows that all circles containing exactly 6 solutions in $\mathbb{E}_0$ must include a solution $\vec{\Lambda}_y \in \mathbb{E}_0$ such that $\vec{\Lambda}_y \cdot \hat{x} = 0$. By the proof of Lemma A.3.3 that is $\vec{\Lambda}_y = u\left(\vec{\Phi}_1 + \vec{\Phi}_2\right)$ for some integer u. Using Equation A.2 we have $\vec{\Lambda}_y/3 = -u\vec{\phi}_1$. This vector has $\left|\vec{\Lambda}_y\right|^2 = 3u^2$ by explicit calculation of Equations A.1. Additionally, $\left|\vec{\Lambda}_y\right|^2 = (3L)^2 = 3^1 \prod_j m_j^{2\mu_j}$ for natural μ_j and primes $m_j \equiv 2 \pmod 3$ since $\vec{\Lambda}_y$ is one of exactly 6 solutions to $\left|\vec{\Lambda}_j\right| = 3L$. Therefore $u = \prod_j m_j^{\mu_j} \not\equiv 0 \pmod 3$, since prime factorization is unique. Thus, $u = 3z - t$ $\exists z \in \mathbb{Z}, t \in \{-1, 1\}$ and $\vec{\Lambda}_y/3 = -(3z - t)\,\vec{\phi}_1 = z\left(-3\vec{\phi}_1\right) + t\vec{\phi}_1 = z\vec{\Phi}_1 + z\vec{\Phi}_2 + t\vec{\phi}_1$. Thus, if $t = 1$, $\vec{\Lambda}_y/3 \in \mathbb{E}_1$ and if $t = -1$, $-\vec{\Lambda}_y/3 \in \mathbb{E}_1$. Both vectors have length L and the $\mathcal{C}_3$ symmetry of $\mathbb{E}_1$ implies that there are at least two more vectors of the same length. By Lemma A.3.4 there cannot be more than three such vectors, since $\vec{\Lambda}_y$ is one of exactly 6 solutions to $\left|\vec{\Lambda}_j\right| = 3L$. Therefore, either $\vec{\Lambda}_y/3$ or $-\vec{\Lambda}_y/3$ is indeed one of exactly 3 solutions to $\left|\vec{\lambda}_j\right| = L$ in $\mathbb{E}_1$. □

REFERENCES

[1] C. Lee, X. Wei, J. W. Kysar, and J. Hone, "Measurement of the elastic properties and intrinsic strength of monolayer graphene," *Science*, vol. 321, p. 385, 2008.

[2] R. R. Nair, P. Blake, A. N. Grigorenko, K. S. Novoselov, T. J. Booth, T. Stauber, N. M. R. Peres, and A. K. Geim, "Fine structure constant defines visual transparency of graphene," *Science*, vol. 320, p. 1308, 2008.

[3] S. V. Morozov, K. S. Novoselov, M. I. Katsnelson, F. Schedin, D. C. Elias, J. A. Jaszczak, and A. K. Geim, "Giant intrinsic carrier mobilities in graphene and its bilayer," *Phys. Rev. Lett.*, vol. 100, p. 016 602, 2008.

[4] M. O. Goerbig, "Electronic properties of graphene in a strong magnetic field," *Rev. Mod. Phys.*, vol. 83, p. 1193, 2011.

[5] A. V. Eletskii, I. M. Iskandarova, A. A. Knizhnik, and D. N. Krasikov, "Graphene: Fabrication methods and thermophysical properties," *Uspekhi Fizicheskikh Nauk*, vol. 54, p. 227, 2011.

[6] P. Debye and P. Seherrer, "Interference of randomly oriented particles in x-rays," *Physikalische Zeitschrift*, vol. 17, 1916.

[7] J. D. Bernal, "The structure of graphite," *Proceedings of the Royal Society of London. Series A, Containing Papers of a Mathematical and Physical Character*, vol. 106, p. 749, 1924.

[8] P. R. Wallace, "The band theory of graphite," *Phys. Rev.*, vol. 71, p. 622, 1947.

[9] D. P. DiVincenzo and E. J. Mele, "Self-consistent effective-mass theory for intralayer screening in graphite intercalation compounds," *Phys. Rev. B*, vol. 29, p. 1685, 1984.

[10] G. Ruess and F. Vogt, "Höchstlamellarer kohlenstoff aus graphitoxyhydroxyd," *Monatshefte für Chemie und verwandte Teile anderer Wissenschaften*, vol. 78, p. 222, 1948.

[11] J. C. Meyer, A. K. Geim, M. I. Katsnelson, K. S. Novoselov, T. J. Booth, and S. Roth, "The structure of suspended graphene sheets," *Nature Communications*, vol. 446, p. 60, 2007.

[12] C. Oshima and A. Nagashima, "Ultra-thin epitaxial films of graphite and hexagonal boron nitride on solid surfaces," *J. Phys.: Condens. Matter*, vol. 9, p. 60, 1997.

[13] C. Berger, Z. Song, T. Li, X. Li, A. Y. Ogbazghi, R. Feng, Z. Dai, A. N. Marchenkov, E. H. Conrad, P. N. First, and W. A. de Heer, "Ultrathin epitaxial graphite: 2d electron gas properties and a route toward graphene-based nanoelectronics," *J. Phys. Chem. B*, vol. 108, p. 19 912, 2004.

[14] K. S. Novoselov, A. K. Geim, S. V. Morozov, D. Jiang, Y. Zhang, S. V. Dubonos, I. V. Grigorieva, and A. A. Firsov, "Electric field effect in atomically thin carbon films," *Science*, vol. 306, p. 666, 2004.

[15] Y. Zhang, Y. W. Tan, H. L. Stormer, and P. Kim, "Experimental observation of the quantum hall effect and berry's phase in graphene," *Nature Communications*, vol. 438, p. 201, 2005.

[16] E. J. Mele, "Commensuration and interlayer coherence in twisted bilayer graphene," *Phys. Rev. B*, vol. 81, p. 161 405, 2010.

[17] I. M. Lifshitz and M. I. Kaganov, "Some problems of the electron theory of metals ii.," *Sov. Phys. Usp.*, vol. 5, 1963.

[18] Y. Lemonik, I. L. Aleiner, C. Toke, and V. I. Fal'ko, "Spontaneous symmetry breaking and lifshitz transition in bilayer graphene," *Phys. Rev. B*, vol. 82, p. 201 408, 2010.

[19] J. M. B. Lopes dos Santos, N. M. R. Peres, and A. H. Castro Neto, "Graphene bilayer with a twist: Electronic structure," *Phys. Rev. Lett.*, vol. 99, p. 256 802, 2007.

[20] R. Bistritzer and A. H. MacDonald, "Moiré bands in twisted double-layer graphene," *Proceedings of the National Academy of Sciences*, vol. 108, p. 12 233, 2011.

[21] A. H. Castro Neto, F. Guinea, N. M. R. Peres, K. S. Novoselov, and A. K. Geim, "The electronic properties of graphene," *Rev. Mod. Phys.*, vol. 81, p. 109, 2009.

[22] M. Kindermann and P. N. First, "Local sublattice-symmetry breaking in rotationally faulted multilayer graphene," *Phys. Rev. B*, vol. 83, p. 045 425, 2011.

[23] S. Shallcross, S. Sharma, E. Kandelaki, and O. A. Pankratov, "Electronic structure of turbostratic graphene," *Phys. Rev. B*, vol. 81, p. 165 105, 2010.

[24] H. K. Pal, S. Carter, and M. Kindermann, "Theory of twisted bilayer graphene near commensuration," arXiv:1409.1971.

[25] R. G. Ayoub, "Paolo ruffini's contributions to the quintic," *Archive for History of Exact Sciences*, vol. 22, p. 253, 1980.

[26] H. N. Abel, "Démonstration de l'impossibilité de la résolution algébrique des équations générales qui passent le quatrième degré," *Œuvres Complètes de Niels Henrik Abel*, vol. 1, p. 66, 1826.

[27] S. Shallcross, S. Sharma, and O. A. Pankratov, "Quantum interference at the twist boundary in graphene," *Phys. Rev. Lett.*, vol. 101, p. 056 803, 2008.

[28] J. Jung, A. M. DaSilva, A. H. MacDonald, and S. Adam, "Origin of band gaps in graphene on hexagonal boron nitride," *Nature Communications*, vol. 6, 2015.

[29] Y. Blanter, M. Kaganov, A. Pantsulaya, and A. Varlamov, "The theory of electronic topological transitions," *Physics Reports*, vol. 245, p. 159, 1994.

[30] S. Carter and M. Kindermann, "Novel exact physics in twisted bilayer graphene through bias resonance," In preparation.

[31] J. R. Schrieffer and P. A. Wolff, "Relation between the anderson and kondo hamiltonians," *Phys. Rev.*, vol. 149, p. 491, 1966.

[32] S. Bravyi, D. P. DiVincenzo, and D. Loss, "Schriefferwolff transformation for quantum many-body systems," *Annals of Physics*, vol. 326, p. 2793, 2011.

[33] E. W. von Tchirnhaus, "On a method for removing all intermediate terms from a given equation," *Acta Eruditorum*, p. 204, 1683.

[34] E. S. Bring, *Meletemata quaedam mathematematica circa transformationem aequationum algebraicarum*. Lund, 1786.

[35] G. B. Jerrard, *An essay on the resolution of equations*. London: Taylor and Francis, 1859.

[36] F. Klein, *Lectures on the icosahedron and the solution of equations of the fifth degree*. Ithaca, New York: Cornell University Library: Trübner and Co., 1888.

[37] C. Hermite, "Sur la résolution de l'équation du cinquième degré," *Comptes Rendus de l'Académie des Sciences*, vol. XLVI, p. 508, 1858.

[38] L. Kronecker, "Sur la résolution de l'équation du cinquième degré, extrait d'une lettre adressée à m. hermite," *Comptes Rendus de l'Académie des Sciences*, vol. XLVI, p. 1150, 1858.

[39] F. Brioschi, "Sul metodo di kronecker per la risoluzione delle equazioni di quinto grado," *Atti dell'I. R. Istituto Lombardo di scienze, lettere ed arti*, vol. I, p. 275, 1858.

[40] M. Trott and V. Adamchik, "Solving the quintic with mathematica," *Wolfram Library Archive*, 2001.

[41] O. Marmon, "Hexagonal lattice points on circles," arXiv:math/0508201.

SYMBOL INDEX

VITA

Steven Clay Carter was born of Clay and Angie Carter in Fort Wainwright, Alaska, on May 8, 1990. He graduated valedictorian from Enterprise High School in 2008 and went on to study physics and mathematics at Birmingham-Southern College with the full financial support of the Presidential and Turnipseed-Ikenberry academic scholarships. In 2011, he conducted nuclear physics research at Duke University and met Stephanie Mahalchick. Steve graduated summa cum laude in 2012 and began his doctoral physics studies at Georgia Tech under the Presidential Fellowship. Steve and Stephanie will be married in 2018.

An inquiring reader may reach the author at stevecarterGT@gmail.com